Geo 3900

Master's Thesis in Geology

Fluid-Flow Expressions at Vestnesa Ridge of the NW-Svalbard Margin

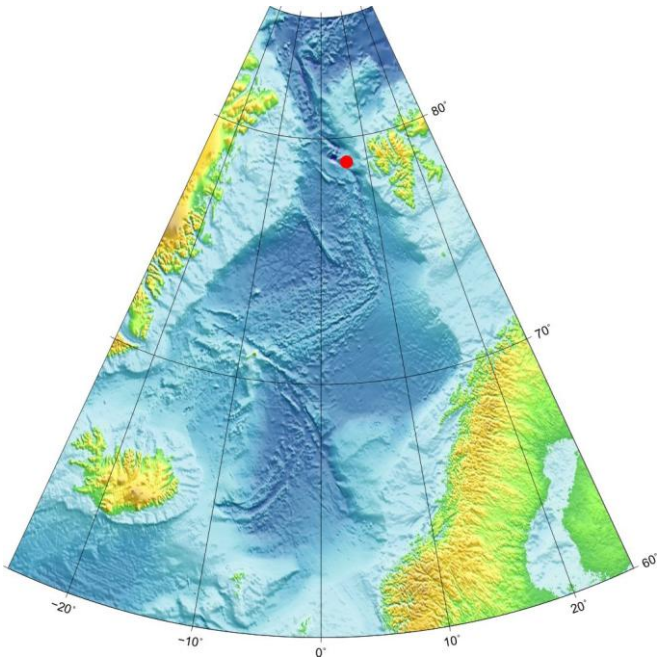

Jon Hermann Pilskog Frantzen

November, 2008

FACULTY OF SCIENCE

Department of geology

University of Tromsø

Geo 3900

Master's Thesis in Geology

Fluid-Flow Expressions at Vestnesa Ridge of the NW-Svalbard Margin

Jon Hermann Pilskog Frantzen

November, 2008

ABSTRACT

The Vestnesa Ridge is a 100 km long and ≈3 km wide sediment drift NW of the Svalbard Margin deposited on young oceanic crust. The crest of the Vestnesa Ridge is pierced by 133 pockmarks, where the orientation and elongation is controlled mainly by processes such as positioning of faulting, creeping of sediments or similar down-slope processes.

High resolution single seismic reflection data together with chirp data across these pockmarks allowed connecting the potential fluid flow pathways in the sub seabed such as acoustic chimneys and faults to the pockmarks at the seabed. The acoustic datasets encompass very high resolution swath bathymetry data gridded to 15m together with very resolution chirp data.

A cross cutting BSR (bottom- simulating reflection) exists in the study area defining the base of the GHSZ (Gas hydrate stability zone), that becomes shallower towards the spreading zone due to increases in heat flow. The GHSZ overlays an approx. 150 m thick layer with enhanced amplitude reflections suggesting considerable amounts of free gas beneath the GHSZ. Due to reduced permeability in hydrated sediments, gas apparently migrates below the GHSZ along the flanks of Vestnesa Ridge upwards towards the crest. Here the pressure builds up as it get trapped below the GHSZ. Acoustic chimneys connects to the seabed pockmarks and pierce through the GHSZ providing a pressure valve for the free gas zone directly beneath the BSR and possibly for the deep acoustic turbidity zone, where gas may accumulate. Suggested source regions of fluid flow encompass both a depth window for thermogenic gas and a shallow temperature window for biogenic gas.

ACKNOWLEDGEMENTS

I would like to thank Prof. Dr. Jürgen Mienert and Assoc. Prof. Stefan Bünz for their excellent supervision. I must specially thank Post Doc. Jörg Petersen for his help with GMT, Fledermaus software and fruitful discussions, and Steinar Hustoft for good discussions and for being available on late evenings. It was a privilege to work with all of you.

I`m also very grateful to Trine Dahl and Post. Doc Corine Davids for all the help with Neptune software, and Steinar Iversen for technical information.

Thanks are to the captain and crew of R/V Jan Mayen for help in acquiring the data. I gratefully acknowledge the friendship and support extended to me by the faculty, staff, and students of the department during my years at the University of Tromsø.

I am very grateful!

Jon Hermann Pilskog Frantzen

CONTENTS

1 INTRODUCTION

1.1 PURPOSE

The aim of this master thesis is to determine and better understand the origin of seafloor and sub-seafloor fluid flow expressions in the Vestnesa Ridge of the NW-Svalbard margin. Seabed fluid flow expression such as pockmarks have been mapped and quantified in detail with focus on size, dip, backscatter and orientation. High resolution single seismic data together with chirp data across these pockmarks allowed connecting the potential fluid-flow pathways in the sub seabed such as acoustic chimneys and faults to the pockmarks at the seabed. The used acoustic datasets encompass swath bathymetry data gridded to 50 and 15 m, together with high frequency single channel seismic (180 Hz) and chirp data (1.5-9 KHz).

The principal aim of using high-resolution data is to image the morphology of the seabed in more detail in relation to shallow sub-bottom sedimentary layers and structures that may be related to gas hydrate and/or fluid flow. Finally, the origin of fluids in the Vestnesa Ridge are discussed and speculated about.

1.2 FLUID FLOW

1.2.1 THEORY OF FLUID FLOW

Darcy's law shows how fluids flow from one area with high pressure to another area with lower pressure. Darcy's law is a definition of permeability for single-phase, one-dimensional flow. The greater the pressure gradient is $((P_b-P_a)/L$ where ΔP is the difference in the hydrodynamic potential, pressure difference between the two ends of the cylinder), the greater the discharge rate will be as long as the lithology and permeability doesn't change. The permeability of a rock is a measure of how easily a fluid may flow through the pore channels in a rock. It depends on the size, shape, and connections between pore channels in the porous medium. The absolute permeability is reached in the porous medium if a single fluid is flowing (Bjørlykke, 2001).

Q = total discharge

ΔP = length in cm

A= cross-sectional area to flow in cm^2

K = permeability

L =applied pressure

μ = fluid viscosity

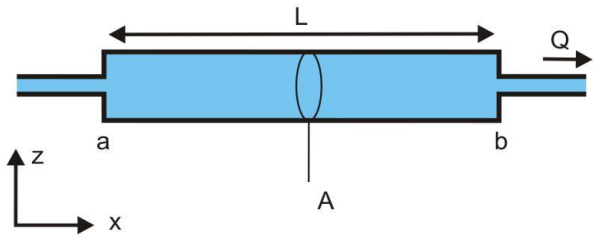

$$Q = \frac{-\kappa A}{\mu}\frac{(P_b - P_a)}{L}$$

Figure 1: Definition of permeability as illustrated by the flow through a cylindric volum. (modified from Bjørlykke, 2001).

The two main principal driving forces for fluid seepage to the seabed are excess pore fluid pressure and buoyancy (Judd and Hovland, 2007).

Overpressure may be caused when pore fluids are unable to drain from fine grained sediments during burial. Such events are commonly caused if the speed of burial exceeds the rate of compaction and the drainage of pore fluids is impeded by low permeability (Judd and Hovland, 2007).

When fluids rise, they will experience a decrease in pressure. This will allow gas to come out of solution and bubbles may form. The free gas in bubbles will expand and reduce the bulk density of the material even further, once initiated, gas migration may lead to a self-perpetuating situation where gas bubbles will grow, and therefore increase the buoyancy and may migrate upward (Judd and Hovland, 2007). This process, in turn may cause fracturing of sediments (e.g. Hustoft et al., 2007).

Fluid may also be trapped in sand bodies, which are surrounded by impermeable layers, which during continuing compaction may cause an increase in overpressure. Also, if gas is accumulated or produced faster than it can be expelled, overpressure will increase as well. During burial this may lead to under-consolidation of sediments since the high pore pressure will minimise the contact between mineral grains, preventing consolidation. This will also decrease the shear strength of sediments, and such processes may lead to slope failures , i.e. geohazards (Kvalstad et al., 2005).

Judd (2003) has shown that seabed fluid flow involving seepage of free methane gas and/or water with a high methane concentration in solution is found in every sea and ocean.

Fluid flow occurs both in passive and active continental margin settings (Judd and Hovland, 2007) (Figure 2). On passive continental margins fluid flow is most common in areas with rapid sedimentation and undercompaction that prevents fluids to be expelled during sedimentation (Judd and Hovland 2007). On active continental margins, fluid flow relates mainly to compressional geological processes (Judd and Hovland, 2007).

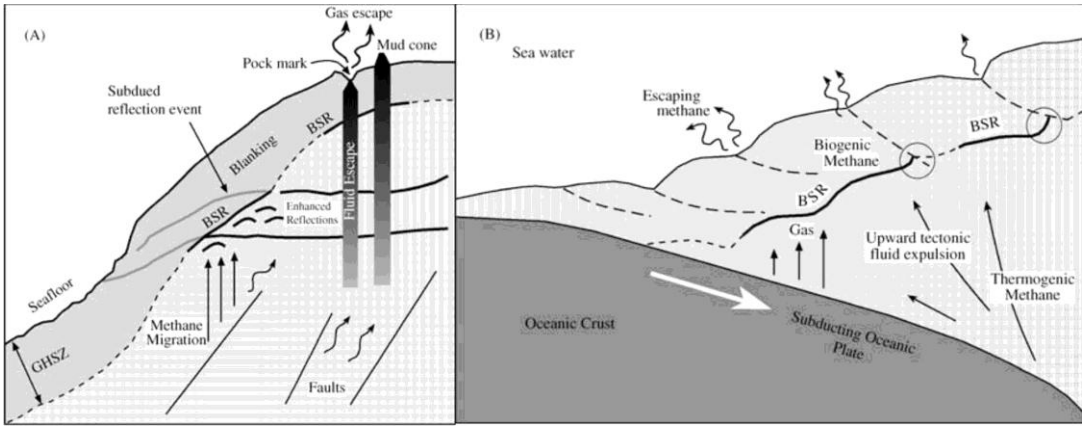

Figure 2: Schematic sketch showing gas-hydrate related features along (a) a passive, and (b) an active continental margin. The (bottom simulating reflector) BSR marks the base of the hydrate stability zone where free gas accumulates beneath gas-hydrated sediments. At passive continental margins, major features observed include subdued reflection events within the GHSZ, blanking, enhanced reflection below the BSR, acoustic turbidity, and fluid escape features such as wipe outs, pockmarks and mud volcanoes. Active margins display forced fluid expulsion features and disturbed BSRs caused by the heat from escaping fluids. Note the disturbed BSR close to the fault locations (circle). Both figures have a vertical exaggeration of approximately 50 (Chand and Minshull, 2003).

1.2.2 INDICATIONS OF FLUID FLOW

Seabed fluid flow can be recognized on seismic and on mutibeam bathymetry data where the seabed and sub-seabed exhibits pockmarks, mud volcanoes, acoustic chimneys, pingos and authigenic carbonate build ups that are related to hydrocarbon migration (Hovland and Judd, 1988).

Pockmarks are indicators of focused fluid flow in marine and lacustrine environments (Hovland and Judd, 1988). They develop in sediments that are suitable for their formation, usually fine-grained sediments. Since there exist no clear discrimination between fluids or its origin that generates pockmarks, they are mainly reported from a wide variety of environments and described morphologically. Hovland et al., (2002) subdivided pockmarks into 6 morphological classes:

• Unit pockmark

They are defined as a small depression (typically 1 to 10m across and up to 0.5m deep), and probably represents a one-time expulsion event. Unit pockmarks are common inside and around normal pockmarks (Figure 3).

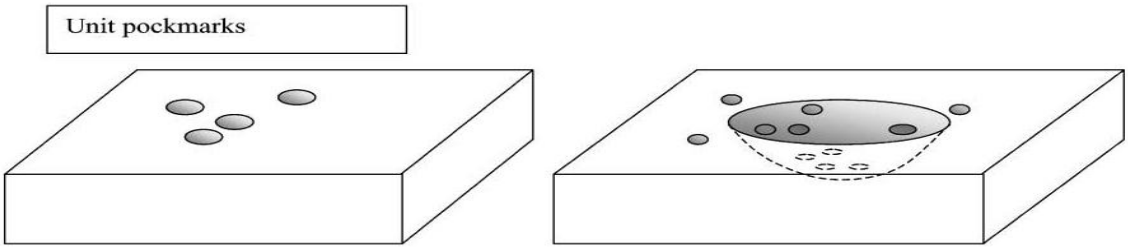

Figure 3: Unit pockmarks, with and without ``parental`` normal pockmark (from Hovland et al., 2002)

• Normal pockmarks

They show circular depressions, typically measuring from 10 m up to 700 m in diameter, with depths from 1 m to 45 m. Their cross-section varies from a basin-formed (low-angle) shape to an asymmetrical and steep-walled feature, and some are even funnel-shaped in the centre (Figure 4).

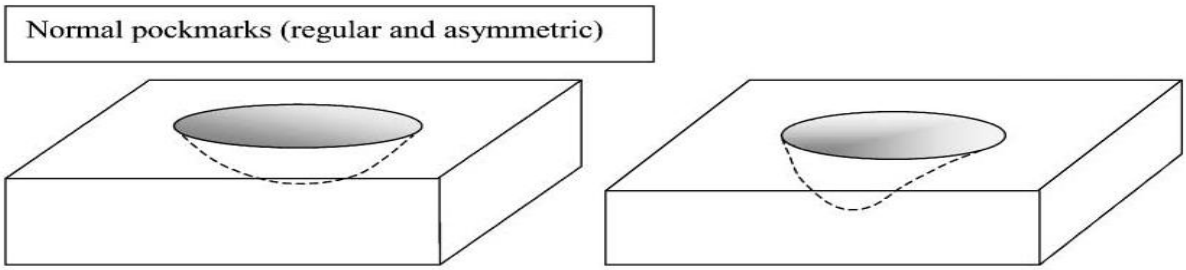

Figure 4: Normal pockmarks (from Hovland et al., 2002)

- Elongated pockmarks

They exhibit depressions where one axis is much longer than the other. This class of pockmark occurs on slopes and areas of the seafloor influenced by strong bottom currents or creeping of sediments downslope. (Figure 5)

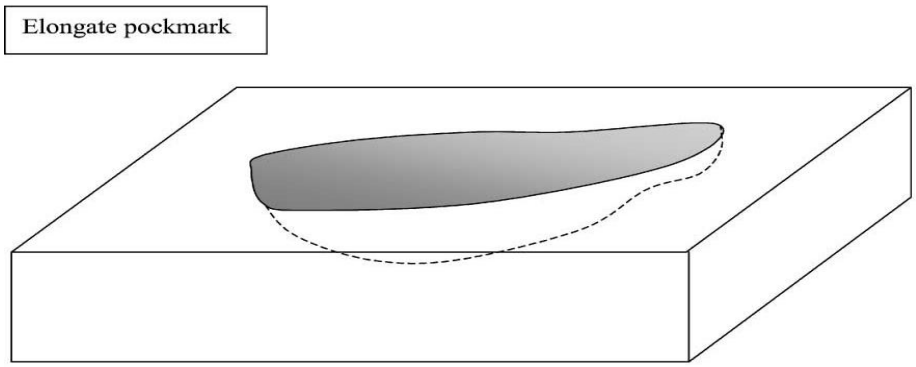

Figure 5: Elongated pockmarks, may also be a composite pockmark (from Hovland et al.,2002)

- Eyed pockmarks

They contain an acoustically high reflective object or region in its central part. Visual inspection often shows that the high acoustic backscatter is due to coarse material remaining after erosive processes (winnowing), biological activity (skeleton remains, dead and living shells, etc.) or authigenic carbonate crusts. (Figure 6)

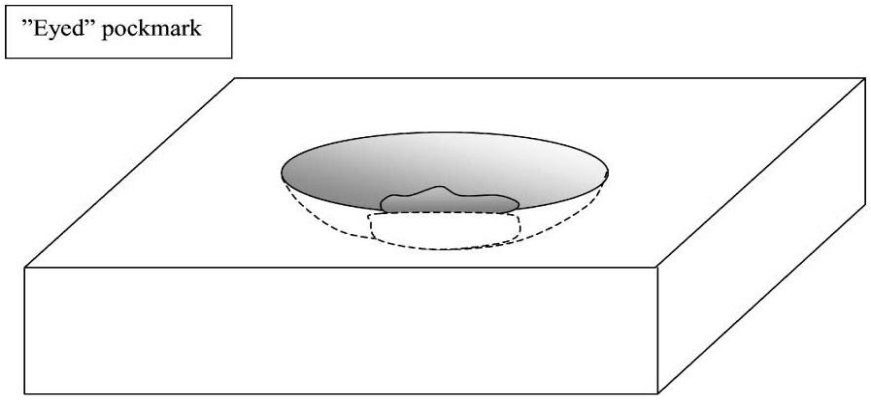

Figure 6: Eyed pockmarks (from Hovland et al., 2002)

• Strings of pockmarks

They consist of unit pockmarks or small normal pockmarks arranged in curvilinear chains or strings, which may be kilometers in length. They are suspected to be a result of fluid focusing along near-vertical faults, flexure or weakness zones in the upper sedimentary layer. (Figure 7)

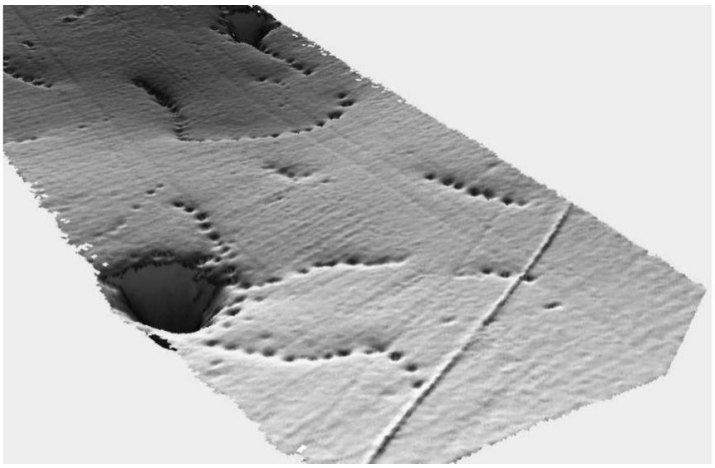

Figure 7: Stringed pockmarks (from Hovland et al., 2002)

• Complex pockmarks

They occur as clusters of normal pockmarks or amalgamations of large pock marks.

Mud volcanism is another widespread phenomenon occurring in many regions of compressional tectonic settings indicating mud and fluid expulsion (Milkov et al., 2004; Kopf, 2002). Mud volcanoes predominantly develop at convergent plate margins, where a high volume of the sediments is subjected to great lateral and vertical stresses. The actual number of features, as well as the amount of material involved in mud volcanism appears to be much greater in offshore than onshore regions (Dimitrov, 2002)

Mud volcanoes can be formed both on land and in oceans at the sea floor. They are formed by the emission of a mixture of solid, liquid and gaseous materials that move up from depth of underlying sediments that are to be emitted at the seafloor. On seismic data, mud volcanoes may be recognized as vertical extensive features, usually with a seismically transparent or chaotic internal character, which disrupt or pierce the normal sedimentary layering (Hovland and Judd, 1988).

The size of mud volcano is mainly a function of the size of the conduit and the driving force of the mud volcanism (Yusifov, 2004). Mud volcanoes may show mud cones, mud pies, domes and/or craters. Mud volcanoes with a negative surface expression are called a mud pool, when extruded material is so fluidized and gassy that it collapses into the crater and fills the depression (Yusifov, 2004).

The different size and shape of mud volcanoes depend to a large degree on the pore fluid pressure, viscosity and porosity. The pore pressure controls how violent an eruption is, while the size can be controlled by the frequency of eruptions. The lower the viscosity of material, the larger and flatter the mud volcano body will become. Low porosity mud will create mud domes or ridges. More consistent mud flows with intermediate fluid content can give rise to mud volcanoes with large diameters and high elevation above the sea floor while high fluid content mud creates mud pies with greater areal extent (Yusifov, 2004).

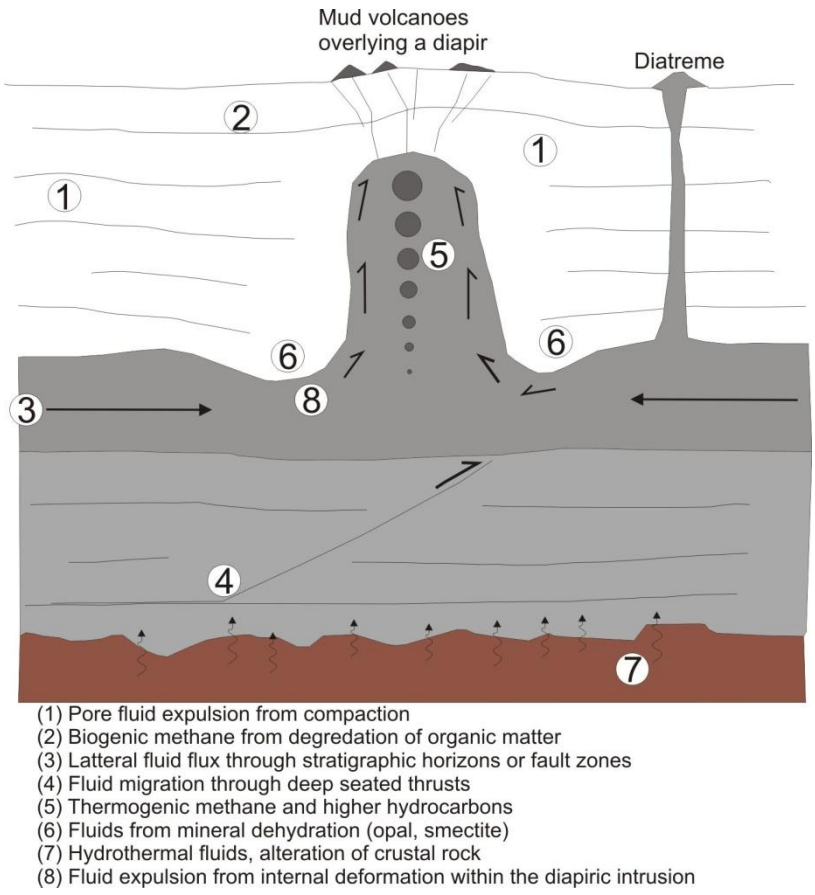

Figure 8: Schematic diagram of a mud diaper with amud volcano extrusion and diatreme including possible fluid sources. (Kopf and Deyhle, 2002).

The above mentioned seabed fluid flow expression often connect to seismic chimneys (Figure 8), which may be detectable as vertical acoustic transparent zones. They are related to variations in subsurface pressure systems by which fluids migrate to shallower levels. When these chimneys reach the seabed, mud volcanoes or pockmarks may form, depending on the intensity of fluid flux and pressure (Ligtenberg, 2003).

Gas chimneys may be detected on seismic data as vertical zones which have been disturbed by previous or ongoing gas migration. The reason for the acoustic disturbance in the chimneys is believed to be caused by small parcels of gas in the pore space of sediments and slightly displaced sediments (Judd and Hovland, 2007). Rapid and strong gas flows may cause upward directed structural disturbances of sediment layers and a blow feature out at the sediment surface. Gas in chimneys may also cause low velocity zones that in turn result in a

push down of reflectors since gas decreases the travel time of the wave through the medium. Acoustic chimneys may show both push down and pull-up effects. Pull up may occur in the presence of a high velocity zone in layers of, for example, authigenic carbonate or gas hydrate (Figure 9).

Fluids are also able to break through the capillary pressure of overlying sediments while oil and water generally uses permeable formations, faults and fractures to migrate (Ligtenberg, 2003).

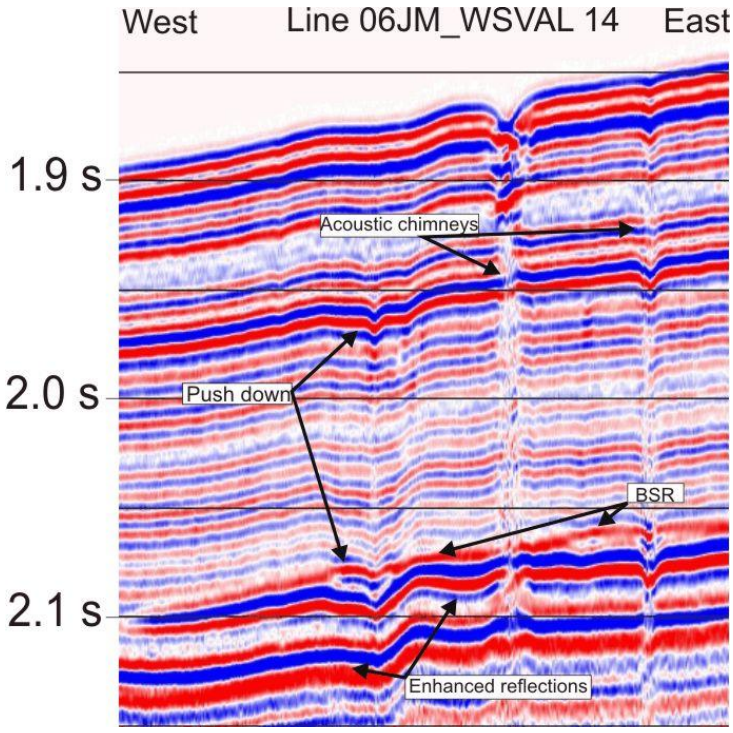

Figure 9: Section of seismic line 06JM_WSVAL 14 (frame c on figure 42a) shows an example of acoustic chimneys, push-down effect, BSR and enhanced reflections below BSR.

More recently, submarine pingos have been reported from marine environments, where gas hydrates and/or authigenic carbonates accumulate in the sub seabed and continue to grow upwards. They are believed to exist only in areas of relatively high fluid flow flux (Hovland and Svensen, 2006).

1.2.3 METHANE SOURCES

Organic matter containing hydrogen and carbon is formed during photosynthesis and enters the marine food chain (Figure 10). This material can be decomposed in the water column or in the seabed by microbial activity or by thermocatalytic breakdown further down in the sediments (e.g. Boetius et al., 2000). Unless the gas is trapped in shallow gas reservoirs or in gas hydrates, the hydrocarbons will migrate towards the seabed. Here, some of the free gas may be consumed by anaerobic oxidation of methane (AOM) and/or may be trapped by the process of authigenic carbonate precipitation.

Special and enriched benthic communities are often associated with fluid seeps (Vogt et al., 1999). The crest, for example, of Hydrate Ridge in the northeastern Pacific Ocean is populated by large communities of clams of the genus Calyptogena, and by thick bacterial mats of the sulphide-oxidizing Beggiatoa, both of which indicate areas of active gas seeping (Linke et al., 1994)

The remaining methane that reaches the water column may get oxidized (Figure 10) but methane bubbles may reach the atmosphere. Moreover, methane and its components may become available for recycling during photosynthesis (Figure 10) (Judd et al., 2002)

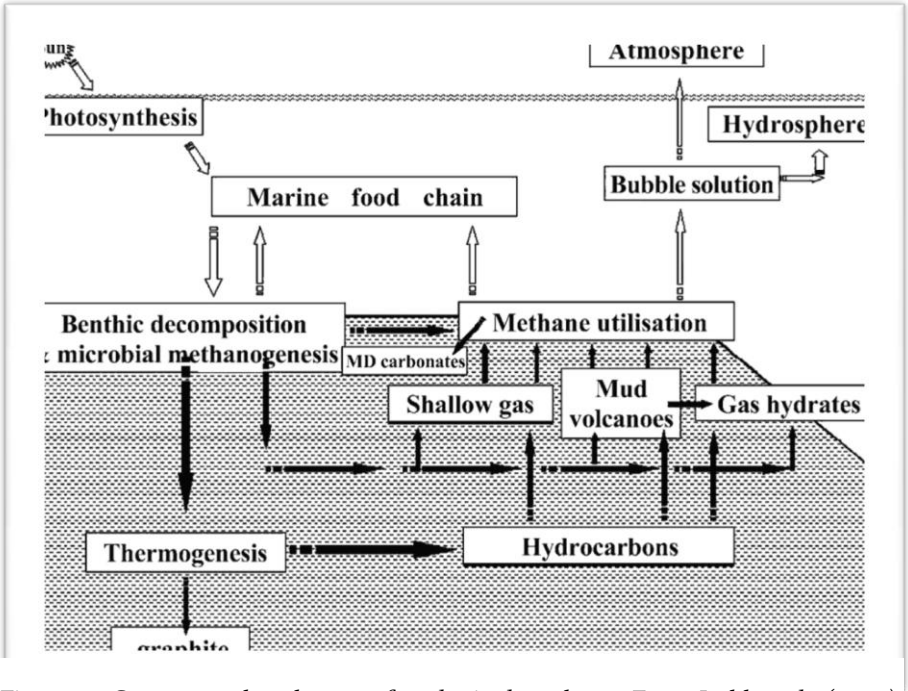

Figure 10: Sources and pathways of geological methane. From Judd et al., (2002)

Two types of methane exists, biogenic and thermogenic. Organic material is degraded first microbially and then thermogenically degrading to form oil and other hydrocarbons (Figure 10).

Organic material in the ocean is recycled mainly by oxidation within the water column. The material that reaches the sea floor and does not get utilized will be included in the sediments and decomposed by microbiological processes, which in turn generates the biogenic methane (Floodgate and Judd, 1992). Thermogenic methane, in contrast, comes from the thermal decomposition of organic matter originating in greater sub-seabed depth (Figure 10). Generally, thermogenic gases are formed from the thermal breakdown of complex organic compounds, including kerogen, at high pressures and temperatures at depths in excess of 1 km below the Earth surface (Judd et al., 2002). Thermogenic gases may be also found in gas hydrates as described from the Gulf of Mexico, the Caspian Sea, and a few other places where there are known petroleum systems (Kvenvolden, 1995).

1.2.4 HYDROTHERMAL CIRCULATION IN YOUNG OCEAN CRUST

Circulating seawater through young oceanic crust will cool the surrounding rocks. Cracks through which the water flows may become sealed by mineral precipitation. In addition, with an increase in age of the ocean crust due to seafloor spreading, sediments accumulate on top of the rocks causing an increase in the thickness of the sediment blanket. With an increase in age of the subsiding crust the increase in the thickness of the sediment will hinder further hydrothermal circulation (Judd and Hovland, 2007).

Especially, the young ocean spreading ridges such as the study area off Knipovich Ridge may be permeable due to wrenching, faulting and fissuring. In general, ocean water may become circulated through fractured rocks (Judd and Hovland, 2007). The inflowing cold water gets heated near the hot magma chambers, and the hot water increases its buoyancy and it may get expelled through hydrothermal vents or fluids. Plumes of rising hydrothermal fluids may rise into the water column (Judd and Hovland, 2007).

1.2.5 SIGNIFICANCE OF FLUID FLOW

Methane, if released in form of bubbles from the seabed to the atmosphere, has a global warming potential 20 times greater than an equivalent weight of carbon dioxide when integrated over 100 years (Shine et al., 1990). Geological methane is released preferably from shallow water sites to the atmosphere by natural gas seeps and mud volcanoes. It has been estimated that 6.6 -19.5 Tg of methane enters the atmosphere from the continental margins worldwide (Judd et al., 2002).

The factors that decide if geological methane gas has a positive or a negative feedback in the global carbon cycle is, according to Judd et al., (2002), decided by:

- The relative disposition of gas sources with respect to sea-level, and the extent of ice sheets, permafrost and gas hydrate stability zones;
- The amount of sea-level rise or fall;
- The duration of glacial- interglacial cycles;
- The rapidity of climate change.

1.3 GAS HYDRATES

Gas hydrates are crystalline solids, where gas molecules are entrapped in cages of water molecules (Judd and Hovland, 2007). Gas hydrates are similar to ice, except that the crystalline structure is stabilized by a gas molecule within the cage of water molecules (Judd and Hovland, 2007). Many gases have molecular sizes suitable to form hydrate, including natural occurring gases as methane and other hydrocarbons. According to Kvenvolden (1998) gas hydrates consist mainly of biogenic methane gas, and that is why they are called methane hydrate.

On Earth, natural gas hydrates can be found mainly in oceanic and permafrost regions, where the pressure (P) and temperature (T) conditions are such that gas hydrates remain stable (Figure 11). In addition, there must be an adequate supply of gas molecules and water within the sediments (Hovland, 2005; Kvenvolden, 1993).

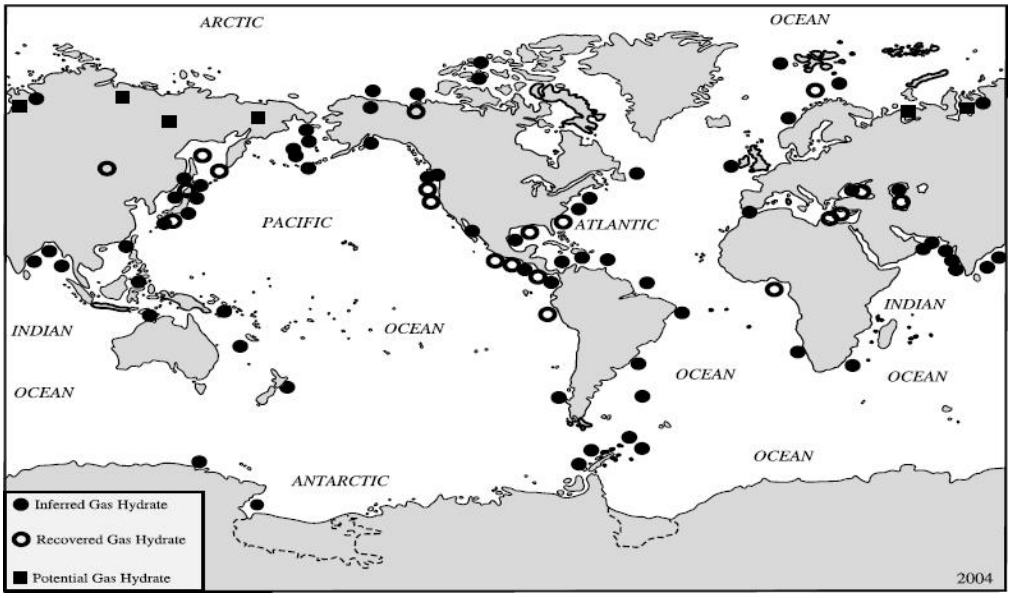

Figure 11: Worldwide distribution of known and inferred gas-hydrate deposits in sediments of continental margins and permafrost regions. (Figure 5, from Kvenvolden and Rogers, 2005).

Hydrates may also occur in lacustrine environments such as Lake Baikal (Vanneste et al., 2002).

The maximum amount of methane occurs in an ideally saturated methane hydrate. The molar ratio of methane to water is 1:5.75, which is equal to a volumetric ratio at standard conditions of methane gas to water of 216:1 or a volumetric ratio of methane gas to solid hydrate of 164:1 (Sloan, 1998).

Natural gas hydrate is usually formed in one out of three types of lattice (Sloan, 1998), where the most common lattice is structure I, which is a body-centered cubic structure that is created with small gas molecules like and , that exist in situ in deep ocean sediments. Structure II has a diamante lattice, created in the cubic system and have space for gas molecules larger than ethane, but smaller than pentane (Sloan, 1998).

Structure II may be created due to gas seepage from deep laying reservoir (Kvenvolden, 2005). Structure H has a hexagonal lattice with cavities large enough to contain molecules with the size of Nafta, diesel and gasoline. The formation of Type H requires the cooperation of two guest gases one large and one small to be stable. It is the large cavity that allows structure H hydrates to fit in large molecules, given the presence of other smaller help gases to fill and support the remaining cavities. Structure H hydrates are dependent on thermo-

genically-produced heavy hydrocarbons (Kvenvolden, 1995).

Structure II and structure H hydrate are more stable than structure I hydrate (Kvenvolden, 1995). The results from the DSDP and ODP shows that hydrocarbon gases in gas hydrate samples recovered from deep ocean sediment always contain > 99% methane and are therefore likely to be of structure I (Kvenvolden, 1995). Brooks et al., (1984) discovered structure II hydrates in the Gulf of Mexico in three of his samples, which contained 62.1-97.4% methane. At nearby Bush Hill, Sassen and MacDonald (1994) found surficial structure H gas hydrate having 21.2% methane, where isopentane were the most abundant gas (41.1%).

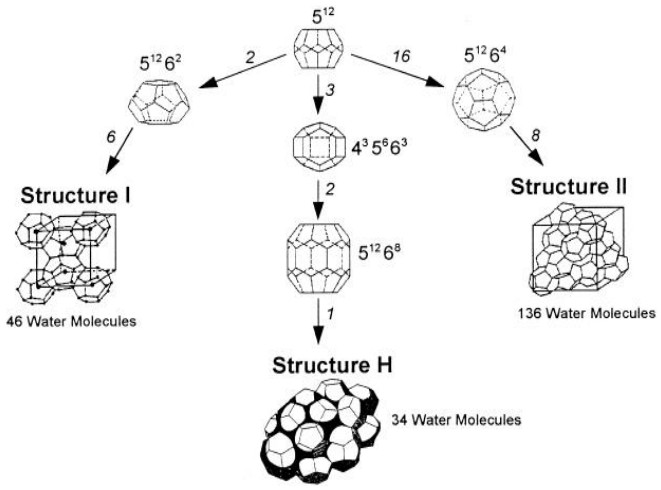

Figure 12: Cage arrangement for structure I,II and H. Figure 1, from Sloan, (1998)

1.3.1 GAS HYDRATE STABILITY ZONE

The gas hydrate stability zone is controlled by (Figure 13) the water temperature, the geothermal gradient, the pressure or water depth, and the pore water chemistry (Judd and Hovland, 2007).

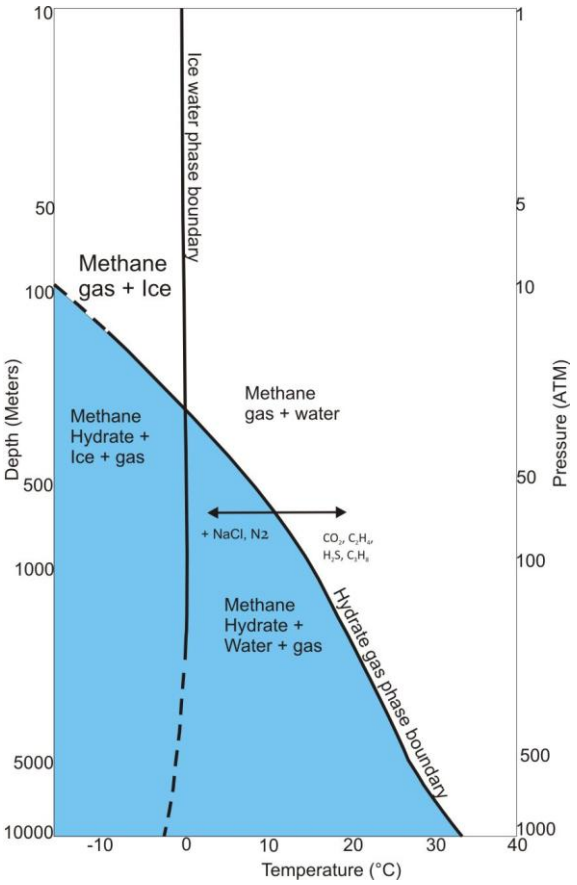

Figure 13: Phase diagram showing the boundary between free methane gas (white area) and methane hydrate (blue area) for a pure water and pure methane system. The addition of salts, such as NaCl, to water shifts the curve to the left. Adding CO_2, H_2S, C_2H_6 or C_3H_8 to methane (CH_4) shifts the boundary to the right, thus reducing the pressure for gas-hydrate stability at a given temperature. Depth scale assumes lithostatic and hydrostatic pressure gradient of 10.1 kPa×m^{-1}. From Kvenvolden (2000).

1.3.2 BOTTOM SIMULTING REFLECTION (BSR)

Gas hydrates may be indirectly detected using seismic methods, where the base of the gas hydrate stability zone (BGHSZ) is indicated by a BSR (bottom simulating reflection). The BSR is due to an abrupt change in acoustic impedance (Figure 9). The compressional wave velocity decreases abruptly when the seismic signal enters from the hydrated sediments above to gas charged sediments beneath it. Due to the velocity drop, the gas hydrate/free gas related BSR shows a phase reversal if compared to the sea floor (Figure 9).

The true nature of BSR is mostly due to the presence of free gas beneath the hydrate sediments (Andreassen et al., 1995). Since the BSR from gas hydrates is dependent on pressure and temperature, it may also cross cut the sedimentary bedding (e.g. Bünz and Mienert, 2004).

BSRs can also be caused by diagenesis in silica rich sediments. Diagenesis causes a transformation from Opal A to Opal CT, and from Opal CT to quartz during increased pressure and temperature during burial of sediments (Kastner et al., 1977). This process causes a positive acoustic impedance contrast, which will generate a seismic reflection parallel to the sea floor, but with the same seismic phase as the sea floor (Berndt et al., 2003). Thus, it can be relatively easily distinguished from a “gas-hydrate BSR”.

1.3.3 SIGNIFICANCE OF GAS HYDRATES

There are several reasons why gas hydrates are important: it has a potential of being an energy resource, a factor in global climate change, and a geohazard (Kvenvolden, 2000). As a energy source, the density (volume of methane at standard conditions per volume of sediment) of methane hydrate is 10-fold greater than the energy density of other unconventional sources of gas, such as coal beds, tight sands, black shale, and deep aquifers, and 2- to 5-fold greater than the energy density of conventional natural gas (Kvenvolden, 2000)

During gas-hydrate formation, methane and water become immobilized as a solid. The permeability of the sediment decreases due to gas hydrate growths and the normal processes of sediment compaction stop.

Continued sedimentation causes a deeper burial of gas hydrate. Finally, gas hydrate will

reach a temperature where the gas hydrate is no longer stable. The solid gas hydrate will become a liquid gas/water mixture, thus the basal zone of the gas hydrate becomes under consolidated and possibly over pressured due to newly released gas, leading to a zone of weakness. This zone of reduced shear strength and increased overpressure may result in submarine slope failures (Figure 14) (e.g. McIver, 1982)

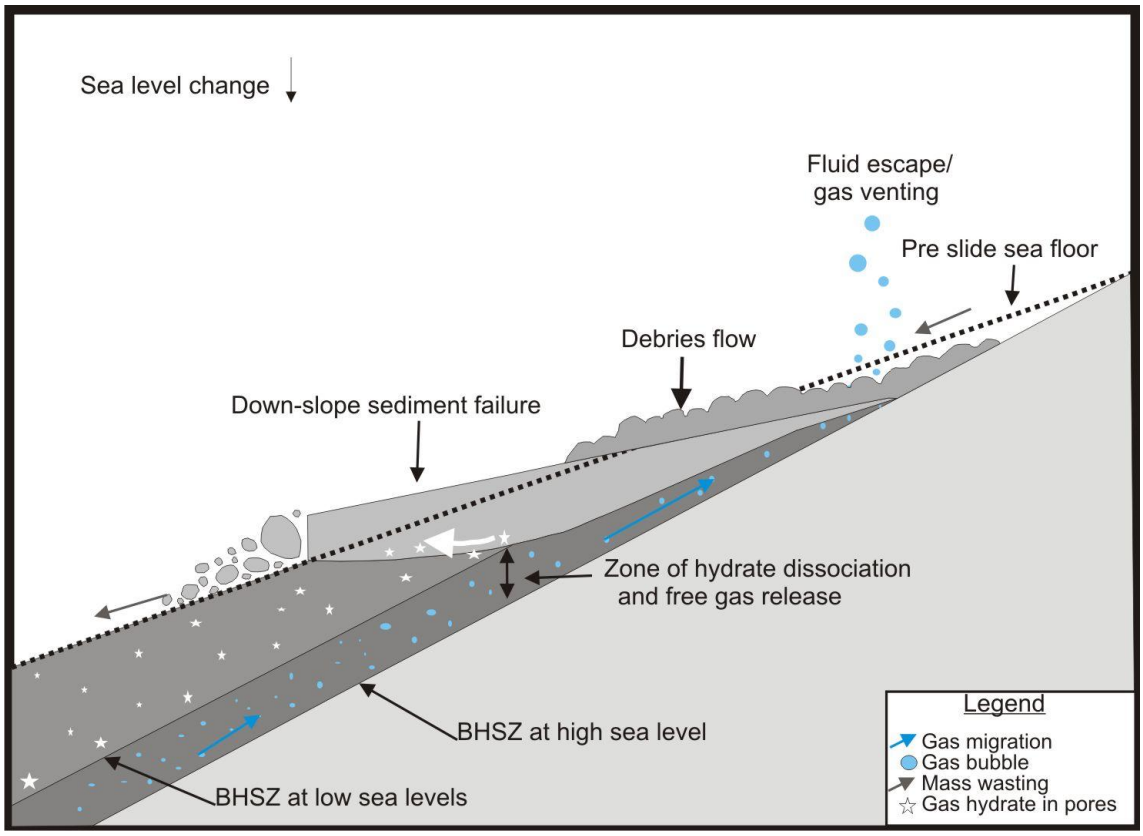

Figure 14: Schematic diagram showing a slope failure along the base of the gas hydrate stability zone From McIver, 2004.

A study of the Storegga slide by Mienert et al., (2005) suggests that the hydrate stability zone in the upper part of the Storegga area was significantly influenced by variations in ocean temperature. As a result, dissociation of gas hydrates occurred due to a shoaling of the BHSZ in the Holocene. Moreover, the solubility of methane in water increased due to pressure increases in times of Holocene sea level rise, which in turn causes an increase in the dissolution of gas hydrates (Sultan et al., 2003)

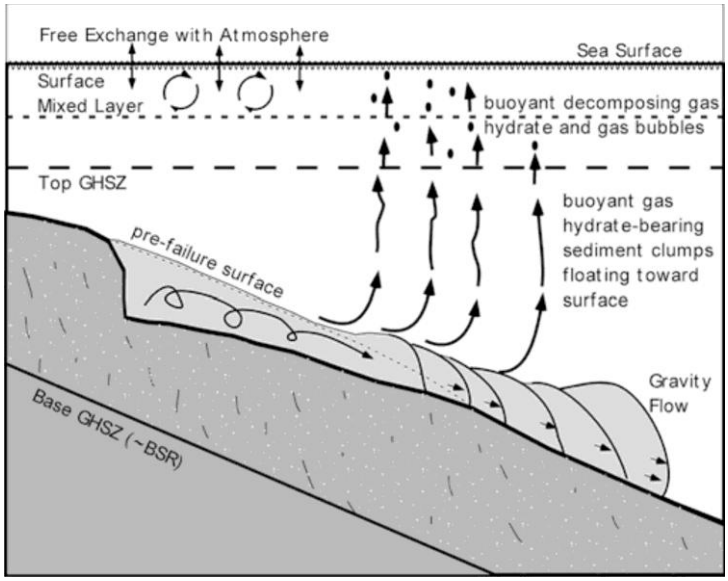

Figure 15: Schematic diagram showing sea-level change and the P/T condition, which may result in submarine slides (McIver, 1982). Figure from McIver (1982).

Mienert et al., (2005) and Vogt et al., (2002) concluded from their modelling results that the location for gas hydrate dissociation might explain the headwall development within the retrogressive sliding model.

According to the clathrate gun hypothesis proposed by Kennett et al. (2003), temperature increases in the upper intermediate waters intersecting upper continental slopes may partially destabilize the methane hydrate reservoir leading to CH_4 releases to the atmosphere/ocean system.

It has been suggested that the methane hydrate system is episodically loaded during cold intervals of the late Quaternary when cold intermediate waters bathed the slopes of the upper continental margins. Switching to sources of warm intermediate waters at stadial and glacial terminations created the instability in the methane hydrate reservoir and catastrophic releases of CH_4 into the ocean/atmosphere system (Figure 15). In contrast, Kvenvolden (2000) claims that although methane is a "greenhouse" gas in the atmosphere, much methane from dissociated gas hydrate may never reach the atmosphere, but rather may be converted to carbon dioxide and sequestered by the hydrosphere/biosphere before reaching the atmosphere.

1.4 CONTOURITES

Contourites are sediments deposited or substantially reworked in deep water by the action of bottom currents. They are known to cover large parts of the ocean floor and continental margins. Contourites are composed of fine grained structure-less mud. However they also show wide variation in grain size including sandy contourites and gravel lag deposits (Rebesco and Stow, 2001). Coarse- to fine-grained sediments, along with sea-floor erosion, are common features in contourite accumulations (Viana et al.,2007). Sediments arrive on the upper slope and are there entrained into the slope circulation system (Figure 16). They are redistributed parallel to the isobaths, forming elongated sediment deposits (e.g. Viana et al,. 1998).

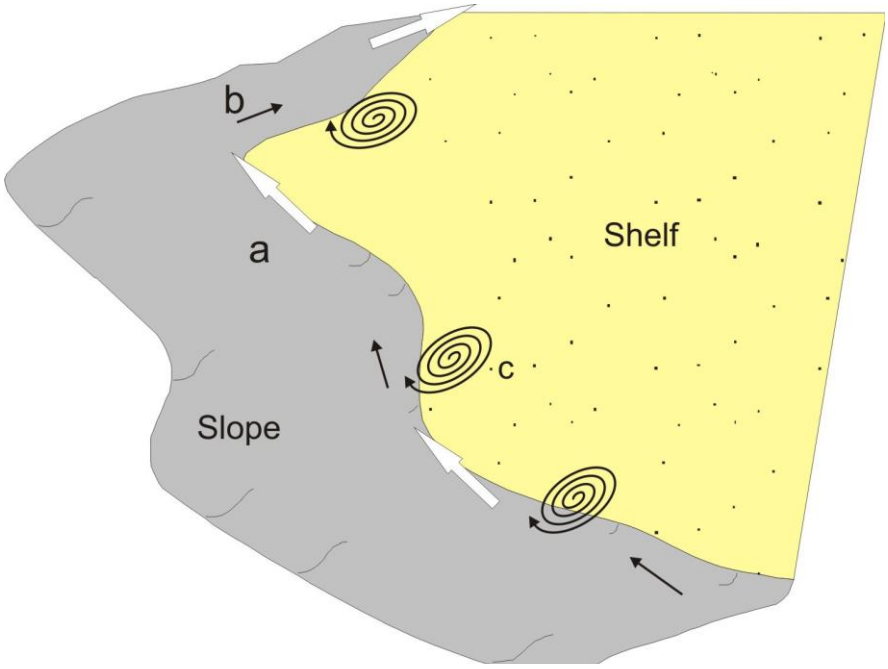

Figure 16: Schematic sketch of the current behavior with respect to margin configuration. Zones of current acceleration (a) are related to seaward margin projections and topographic obstacles that confine the flow; zones of decelerations (b) corresponding to margin re-entrants and flow expansion can induce formation of gyres or eddies (c). Sizes of arrows indicate current intensity. From Viana et al, (2007)

In deep water, thermohaline currents follow the contours and may develop major sediment drifts several hundred kilometers in length, several tens of kilometers in width, and several hundred meters thick (e.g. McCave 1985).

The factors that regulate where, when and how contourites develop in sedimentary basins and along continental margins are according to Viana et al (2007) controlled by:

- Intensity and duration of bottom-current regime;
- The grain size population available to the current action;
- Sea floor physiographic;
- Margin configuration.

Three main types of contourite deposits were proposed by Faugeres et al. (1993): They include giant elongated drifts that are hundred of km long and may exceed a thickness of 1-3 km, deposited parallel to the direction of the bottom current. Another feature are contourite sheets that have an extensive low relief and sediment waves on top, as for example observed in the Argentina basin. Typically, the sediment waves have amplitudes of 10-80 m, and wavelengths of 1-10 km, showing up-current migration. The third type of contourites is related to deep channels or passages where the speed of bottom current in increases. Such contourite deposits develop in the channel, the flanks and at the down current exit of the channel.

At the Norwegian shelf and the upper slope sediment drifts are located locally in lower slope embayment and in existing slide scars (Laberg et al., 2005), and along the southern area of the Fram Strait at the NW-Svalbard margin (Eiken and Hinz, 1993). All along the Atlantic passive margin settings, gas hydrate associated with BSRs are mainly found in contourite deposits (Dillon and Paull, 1983).

2 GEOLOGICAL SETTINGS

2.1 TECTONIC

The study area is located at the Vestnesa Ridge situated at the Northwest Svalbard margin in the Fram Strait, north of the Knipovich Ridge and east of the Molloy transform fault (Figure 17).

During the Cenozoic, the Norwegian Greenland Sea opened in several episodes. The sea floor spreading started in early Eocene and in the Oligocene. Changes of plate movement resulted in the development and activation of the Knipovich Ridge, forcing continental separation of Greenland and Svalbard (Lundin et al., 2002). Due to the continental spreading the Fram Strait opened between 15 and 7Ma and developed as the only deep water passage between the Arctic and the Atlantic Ocean, and since then it has played a dominant part in the large scale oceanic circulation processes (Thiede and Myhre, 1996).

The Knipovich Ridge is slowly and obliquely spreading at the northernmost part of the Atlantic Ridge system, abutting the West Svalbard margin at ~ 20 – 15 Ma (Thiede and Myhre, 1996). Due to the presence of fault and rift escarpments further north and glacigenic sediment input from the nearby margin, the Knipovich Ridge (Crane et al., 2001) is propagating as a sediment-buried feature with the Vestnesa Ridge. The faults are locally deforming the strata up to the sea floor and may form migration pathways for fluids coming from young hydrothermal systems within the ocean crust. A series of transform faults and short spreading centers connect the Knipovich Ridge in the most northern part of the Norwegian-Greenland Sea with the Gakkkel Ridge in the eastern Arctic basins (Thiede et al., 1998).

2.2 VESTNESA RIDGE

The Vestnesa Ridge is a SE-NW to EW bending sediment drift lying just east of the Molloy Ridge at 78.5N. The Vestnesa Ridge sediments are deposited on young oceanic crust that resemble an age between 3-14 Ma (Vogt et al., 1994). The sediments are believed to consist mainly of glacigenic debris flows (GDF) coming from trough mouth fans during glacial maxima and/or turbidite, glaciomarine and hemipelagic sediments, which have been partly reworked by contour currents (Ottesen et al., 2005).

2.2.1 SEDIMENTATION AND OCEAN CURRENTS

The Fram Strait is dominated by two main surface currents, the warm and northward flowing west-Spitsbergen current and the cold and southward flowing East-Greenland current (Aagaard et al., 1987).

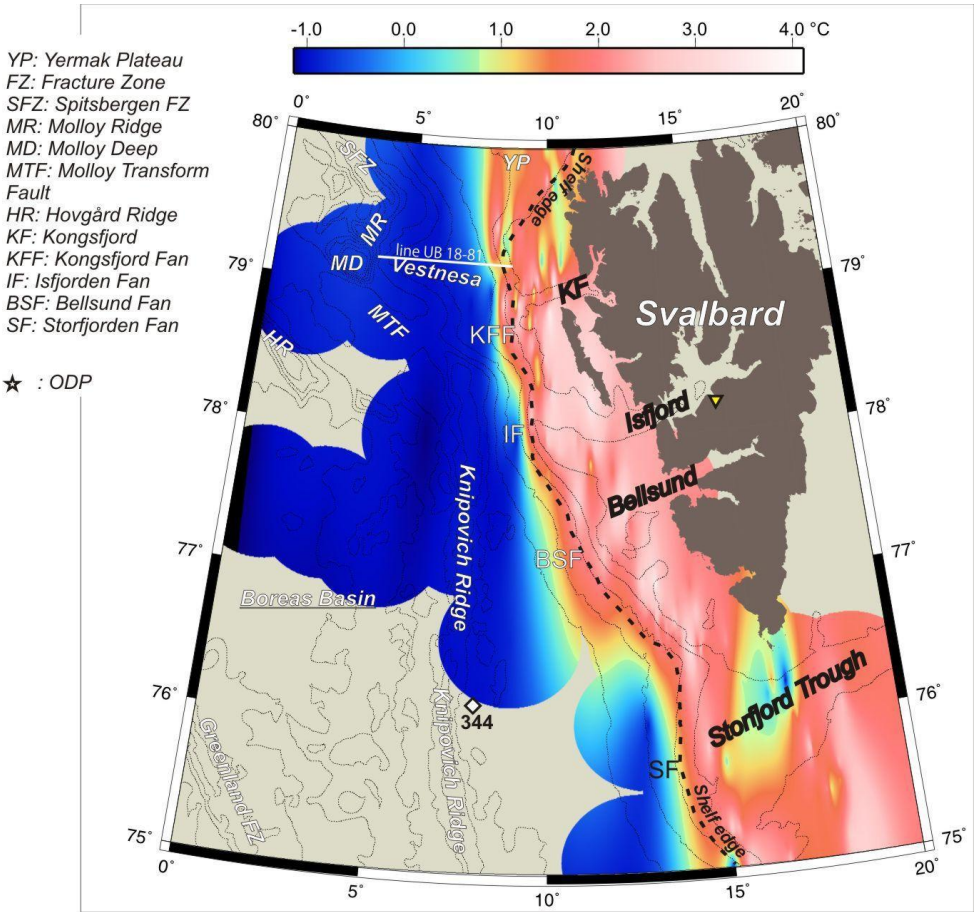

Figure 17: Map showing the bottom water temperature and the main tectonic features in the study area. The approximate position of seismic line UB 18-81 from Eiken and Hinz (1993) is indciated (white line) (see also Figure 18) as well as Deep Sea Drilling Project site 344 (Solheim, 1994; Talwani and Udintsev, 1976) .

According to Eiken and Hinz (1993) deep persistent currents have influenced the sedimentation in large parts of the Fram Strait since the late Miocene, where contourite deposits are mainly concentrated in the eastern part of the Fram Strait.

The uplift of the continental crust of Svalbard in postglacial times and the subsidence of the young ocean crust did was most likely accompanied by increases in sediment fluxes into the eastern part of the Fram strait (Eiken and Hinz, 1993). The continental ocean transition (COT)

zone runs slightly west of the Vestnesa Ridge (Figure 18).

Eiken and Hinz (1993) divided the Vestnesa Ridge into three seismic sequences that can be traced to the Yermark Plateau. These are YP-1, YP-2 and YP-3 that show continuous strata with only minor unconformities (Figure 18), and are defined as follows:

YP-1: Lowermost sequence YP-1 with sub-parallel reflections directly over the oceanic basement.

YP-2: Westward-thickening wedges with a migration of the depocenter and a sequence that downlaps to the west (Figure 18). It is believed to be the result of contour currents that systematically migrate upslope in response to the changing configuration of the seabed morphology caused by their own deposition.

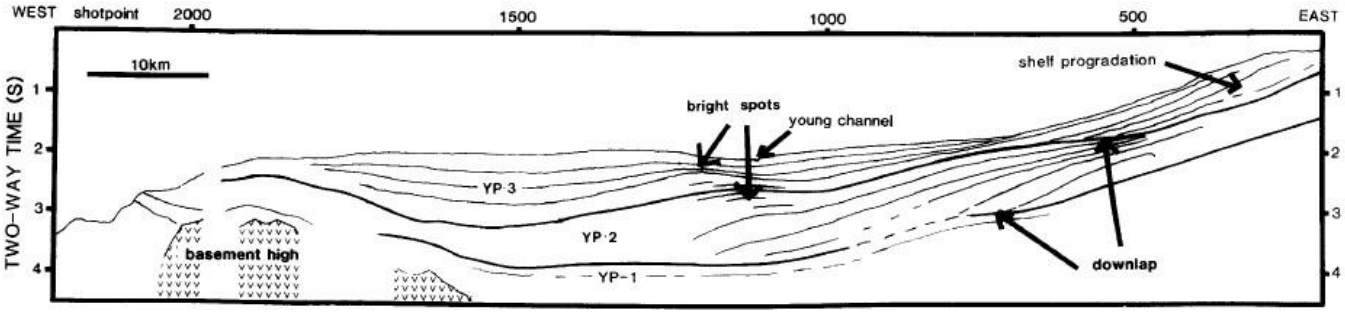

Figure 18: Interpretation of seismic line UB 18-81parallel to Vestnesa Ridge (Eiken and Hinz., 1993).

YP-3: Sediment depocenter with a prograding sequence at the outer shelf and a second depocenter of elongated shape at the Vestnesa Ridge (Figure 18)

Sediment core analysis from the Vestnesa Ridge (Howe et al., 2008), suggest glaciomarine muddy to silty contourite deposits from the west Spitsbergen current. They have been formed above muddy and sandy turbidites. Howe et al (2008) calculated high sedimentation rates of 105 cm/kyr for the mid to late Weichselian with a decrease to less than 10 cm/kyr between the LGM and Holocene. Preliminary analysis of box core JM08-325-BC and gravity core JM08-327GC acquired by the Arctic Marine Research School in Tromsø (pers. comm. Jessen, Simon. Pind.) suggest that the upper 6 cm consisted of residual sediments (pebbles) are due to current winnowing in the area of the sediment drift.

2.2.2 GLACIAL DEPOSITS

Deep Sea Drilling Project site 344 indicates glacial conditions at least since 5-7 Ma (Solheim, 1994; Talwani and Udintsev, 1976) (Figure 17). Today 60 % of Svalbard is glaciated, but most of the sediments seem to be trapped in fjords, which act as a temporary storage of the sediments. During a glacial advance the sediments stored in fjords are most likely eroded by ice streams and afterwards deposited further out on the continental shelf and upper slope (Solheim, 1994).

Along the western Svalbard margin and the entire western Barents sea there are seven significant seismic reflectors that may be correlated, R7- R1 (Figure 19). R7 shows an age of approximately 2.3 Ma marking the onset of glacially dominated deposition along this margin (Faleide et al., 1996; Andreassen et al., 2008). Other probable age exists of 440-200 ka for RI, while R5 may have been formed as a response to the climatic shift between 1.2 Ma and 0.8 Ma (Faleide et al., 1996). Glaciers reached the shelf break off Svalbard and the Storfjorden Trough already at R7 (Faleide et al., 1996) while the southwestern Barents Sea experienced glaciers that did not reach the shelf break until R5 (Faleide et al., 1996). The seismic sequences around R5, R3 and R1 also indicate that there was a transition from erosion and progradation to accumulation and aggradation at the outer shelf of Svalbard, the Storfjorden Trough and the Bjørnøya Trough indicating subsidence due to the increasing sediment load (Faleide et al., 1996).

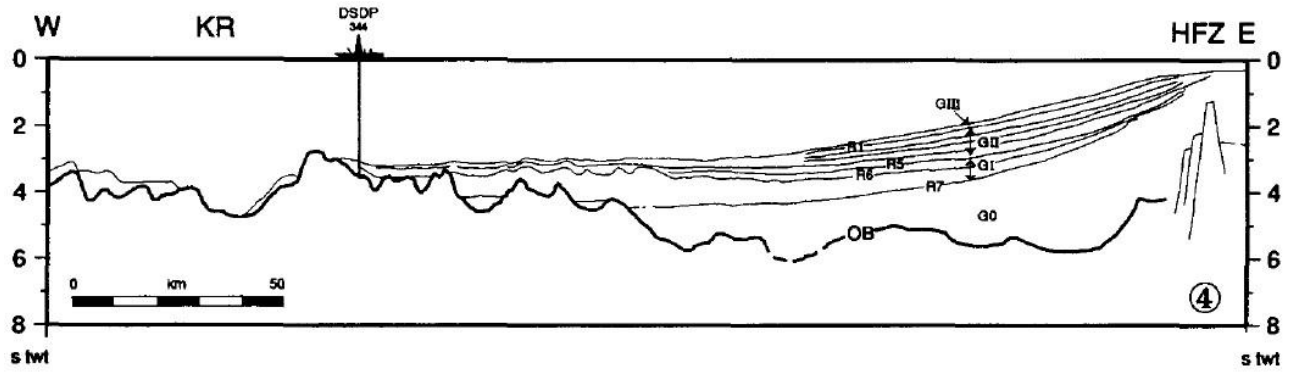

Figure 19: Figure showing DSDP 344 and seismic reflectors R7- R1 along the Storfjorden Fan. From Faleide et al, (1996).

2.2.3 POCKMARKS AT VESTNESA RIDGE

The most prominent pockmarks at Vestnesa Ridge are located at 1100-1500 m.b.s.l (Bünz et al., 2008), and are largely confined to a 3 km wide belt centered at the crest of the Vestnesa Ridge (Vogt et al., 1994). The seafloor is pierced by these pockmarks along the crest of the ridge, where the largest pockmarks have a diameter of 600 m and a depth of up to 20 m (Bünz et al., 2008). Their shapes vary from circular to elliptical (Hustoft et al. 2008,). Vogt et al. (1994) suggested that these pockmarks were caused by episodic releases of methane, that have been trapped below a natural anticline structure of the gas hydrated sediment drift. Vogt et al (1999) found that the sub bottom reflectors at the Vestnesa Ridge bent down in the pockmarks, with no disruption or acoustic wipe-outs that often are seen under pockmarks according to Hovland and Judd (1998).

2.2.4 GAS AND GAS HYDRATES AT VESTNESA RIDGE

Vestnesa Ridge consist of well stratified sequences, where the BSR is situated at 250 ms TWT (Howe et al., 2008; Vanneste et al., 2005). The BSR covers the whole area of Vestnesa Ridge and terminates towards the ridge close to the Molloy Transform with high heat flow and towards the shelf edge with glacial debries flows (Vanneste et al., 2005; Bünz et al., 2008). In the Vestnesa Ridge the BSR is disrupted due to (warm?) uprising fluid flow, thus following the seafloor morphology not in all places (Vanneste et al. 2005; Bünz et al., 2008). The disrupted BSR localities are situated mainly close to the vertical fluid flow pathways including faults (Vanneste et al., 2005).

According to Vanneste et al (2005) the sub bottom depth of the hydrate stability limit varies laterally, and is mainly controlled by the geothermal trend that is connected with the lithospheric cooling away from the Molloy spreading ridge, where the geothermal gradient increases gradually from 70 to 115 °C/km towards the Molloy transform fault (Vanneste et al., 2005). Since the gas hydrate stability zone lies in an area where ocean ridge escarpments are observed, Vanneste et al (2005) suggest a causal link between hydrate accumulation, fluid flow and tectonic activity.

Free gas beneath the BSR and other enhanced reflections act as an effective low pass filter, where the drop of the dominant frequency is approx. 30 Hz (Vanneste et al.,2005). Given

the depth of the observed enhanced reflections underneath the BSR, the free gas zone must be thicker than 150 m (Bünz et al 2008).

3 MATERIAL AND METHODS

3.1 MULTIBEAM (MB) KONGSBERG SIMRAD EM300

3.1.2 MULTIBEAM SONAR SURVEY METHOD

Approximately 7500 km^2 of swath bathymetry data were acquired at Vestnesa Ridge during geophysical surveys with RV Jan Mayen of the University of Tromsø (Mienert et al., 2004; Mienert et al., 2006). Moreover, an area of approx. 35 km^2 were covered at the ridge crest for fluid flow studies using 3D seismic acquisition techniques (Mienert et al., 2007, Petersen et al., 2008). Swath bathymetry collected arrives from the motion-compensated Kongsberg-Simrad EM300 Multibeam sonar system, hull-mounted aboard the R/V Jan Mayen operated by University of Tromsø.

3.1.3 KONGSBERG-SIMRAD EM300 MULTIBEAM SONAR SYSTEM

The EM300 system employs a single mills-cross transducer array geometry that operates at 30 kHz, making it capable of surveying water depths of up to 3000-5000 m. It is possible to select between swath widths (angular sector) of 60 and 150 degrees with 2 degrees interval. For shallower water depths the system operates with 111 beams formed, while for the greater depth ranges the system consists of 135 beams.

For all angular sectors a choice of equidistant or equiangular beam spacing is available. The transmit beam is 1^{o} in width in the fore-aft direction and the receiver beams are 2^{o}/cos (steering angle) wide athwart ship. The position update is up to 1 Hz and heave, pitch, roll and heading information are updated at 100 Hz. Active beam steering for all three rotations of vessel motion, results in a near-uniform sounding density irrespective of instantaneous ship orientation. To obtain best resolution, pulse length and range sampling are variable with water depths.

The operating width of the swath of sonar echo beams produced by the EM300 system depends on the angular sector chosen and the water depth. For a fixed angular sector, the swath width will increase as the water depth increases. But the maximum width can be chosen, such that the system automatically narrows the angular sector when the water depth

increases above the threshold, this way helping to keep a constant sounding density. Bottom returns are determined using a combination of phase and amplitude detection with quoted measurement accuracy in the order of $\pm 0.2\%$ of depth.

The outer beams of the EM300 swath can be of low quality, due to speed and signal reception errors caused by the great travel distance, large propagation angle and low angle of reflection. On R/V Jan Mayen a protection housing is installed around the hardware to avoid damage of ice contact, the amplitudes recorded are slightly attenuated ~6 dB, due to periods with bio incrustation, the attenuating may increase. Also suspended material accumulated at these locations causing a higher attenuation and distortion of the most outer beams (pers. comm. Steinar Iversen).

These outer portions can be removed using software programs. Ship turns also produce unevenly spaced swaths and data logging is normally paused during turns, the turns may also be flagged out during processing. It is possible to eliminate data gaps with ship maneuvers such as the “Farmer’s Turn”.

On R/V Jan Mayen the system runs on a high performance PC (dual 2.8 GHz, 2 GB RAM), displaying the data collected and logging them to hard disk. As a standard, the following parameters are logged: depth, seabed imaging, vessel position, vessel attitude, and sound speed. Sound speeds are loaded from CTD profiles of sound velocity, after appropriate filtering and editing.

The Simrad processors use the sound speed data for instantaneous beam forming and ray tracing of each individual beam, at the same time as they correct for the vessel attitude. The result is the conversion of range and angle data to xyz triplets. A graphical user interface provides control on the data quality and runtime parameters used during acquisition.

3.1.4 RESOLUTION OF THE KONGSBERG-SIMRAD EM300 MULTIBEAM SONAR SYSTEM IN R/V JAN MAYEN

Spatial and horizontal resolution of multibeam sonar method is governed by several separate but dependent parameters. Sonar or acoustic resolution is a function of the area of coverage which is dependent on (Clarke et al 1998; Mosher, 2006)

1. the beam width along the two axes of the acoustic signal
2. the method of bottom detection within the beam footprint (amplitude or phase bottom detection)
3. spatial sampling density (samples per area)
4. positioning resolution, which is function of precision and accuracy of locating the sounding of on the seafloor

The beam width along the two axes will determine the area of coverage (Figure 20). The area of coverage of an acoustic beam is the area of an ellipse ($\pi \times r_1 \times r_2$). For the vertical beam, its area is a function of the water depth (z) and the angle width of the beams in the along-track (ϕ) and cross-track (θ) directions. For the beams off vertical, the area is additionally a function of the beam emission angle (α, from vertical) and the seabed grazing angle (β, from the seabed surface).

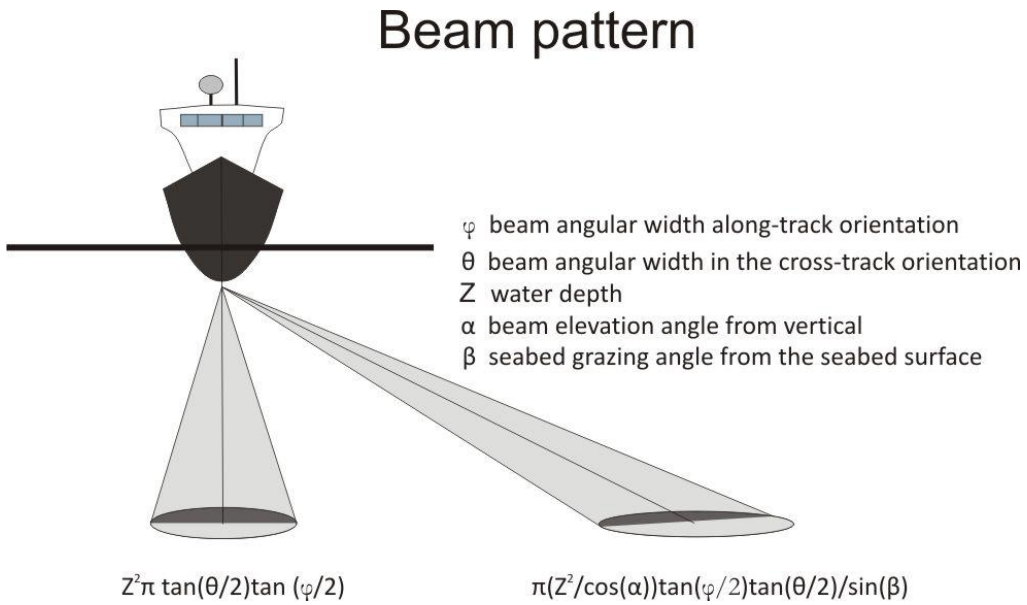

Figure 20: Multibeam sonar beam angle and parameters for calculations of area coverage (Mosher, 2006).

Figure 20 show the area of coverage grows as depth increases and the beam becomes more oblique, resulting in a poorer spatial resolution. Although the obliquity of the beam angle increases the coverage area, at a certain critical angle, the system transform from amplitude bottom detection to a phase detection algorithm. This later greatly enhances the precision of the depth sounding but is still representative of the larger elliptic area.

Field results have proven that with phase detection it is possible to image features smaller than the beam footprint, while the same is not true for amplitude detection (Clarke et al, 1998). This way reducing the beam spacing will increase the sounding density, but the resolution of features smaller than the area of coverage will still depend on the bottom detection algorithm. Values for the area of coverage for different water depths and different beam angles are shown in Table 1.

Water depth (m)	Area of coverage (m^2) (normal incidence)	Area of coverage (m^2) (31.5^O beam)	Area of coverage (m^2) (63^O beam)
500	120	165	580
1000	479	658	2322
1100	579	797	2810
1200	689	948	3342
2000	1914	2633	9287
3000	4307	6924	20897

Table 1: Theoretical area of coverage of multibeam data calculated based on equations given in figure 20. (20/10 beam angular width in along/cross-track)

The density of soundings on the seafloor can be divided in the two axes. In the along ship direction, which is a function of ping rate and vessel motion. While across it is a function of beam spacing, orientation (speed, heave, pitch, roll and yaw) and the amount of overlaps between swaths on successive lines

The beam spacing is usually less than 1^{o} (it varies depending on the angular sector employed and whether beams are equidistant or equiangular). Water depth and obliquity of the beam determine the ping rate, in that the ping period must be greater than the time taken for the sound to travel to and from the most distant target, so wider angular sectors imply smaller ping frequencies. The physical distance between two successive pings is determined by the vessel speed.

3.1.5 VESTNESA RIDGE MULTIBEAM SURVEY

During the surveys in 2004, 2006 and 2007 (Mienert et al., cruise reports) , the Multibeam data were recorded using WGS-84 datum, angular sector set to 126 degrees with equidistant beam spacing, and the maximum swath width was set to 10000 m.

To ensure optimal positioning resolution the system is calibrated once a year for yaw, pitche, heave and roll. Velocity through the water column was integrated from CTD stations acquired prior to and during the bathymetry surveying to update the system.

In areas outside the main Multibeam surveys, the system was kept online during the cruises, thus collecting overlapping data, but due to the lack of sound velocity control and the variation in water depth in the area, positioning resolution is unreliable and much of this data presented very gross ray bending problems. Ray bending occurs due to refraction in the water column in response to spatial sound velocity variations. Nevertheless, some of this overlapping data could be used to get a better spatial resolution in places where the previously measured sound velocity was still accurate.

3.2 PROCESSING

Post processing was done with the software Neptune from Kongsberg Maritime. Neptune is used for post-processing of bathymetric data collected from single beam or multibeam echo sounders, consisting of cleaning and filtering of positioning data, analysis and correction of depth data, tidal height adjustments, automated data cleaning based on statistical rules or manual editing, controlled data thinning, and export of final soundings for further data processing.

All the mentioned steps were applied to the main survey lines, except for the tidal height adjustments, due to the low tidal height differences in the area (1.5 m at Ny Aalesund). The accepted results and the backscatter data was exported as ASCII xyz files.

For the 3D high resolution seismic survey conducted in 2007, the line spacing was so dense (~40m), that the beams had approximately ~88% overlap, thus the phase bottom detection data covered the whole survey area (Figure 21) Therefore when exporting to ASCII xyz files, the phase bottom detection and amplitude bottom was split into two separate files. This was done since the amplitude bottom detection would disrupt the backscatter data, so only the phase bottom detection data was used during gridding of the backscatter data. For the other data, both the phase bottom detection and amplitude bottom detection data was used.

The ASCII xyz files were gridded and studied in the Interactive Visualization System Fledermaus for geomorphic analysis. When gridding the data the number of neighboring soundings inside a given radius is important, by using too small radius, remaining noise from processed data cannot be reduced well enough, by using too large radius, it may smooth the surface characteristics (Fledermaus, 2007).

For the data acquired during the cruise in 2004 and 2006 the weighted moving average method were used with a weight diameter of 8 (Gridding is inherently a low-pass filter in which a depth value for a node is calculated by taking an average of the soundings around the node), with a 50 m by 50 m grid. For the high resolution data acquired during the 2007 survey the same gridding method was used, but with an weight diameter of 3, and a grid 15 m by 15 m. The same method and parameters were also used for the backscatter data.

For further geomorphic analysis and for calculating attribute maps, Generic mapping tools (GMT) were used. GMT provides a public suite of tools used to manipulate tabular, time-series, and gridded data sets, and to display multibeam data in appropriate formats for data analysis (Wessel and Smith, 2008). The data there was gridded with the near neighbor algorithm, using the same parameters that were used for the Fledermaus software.

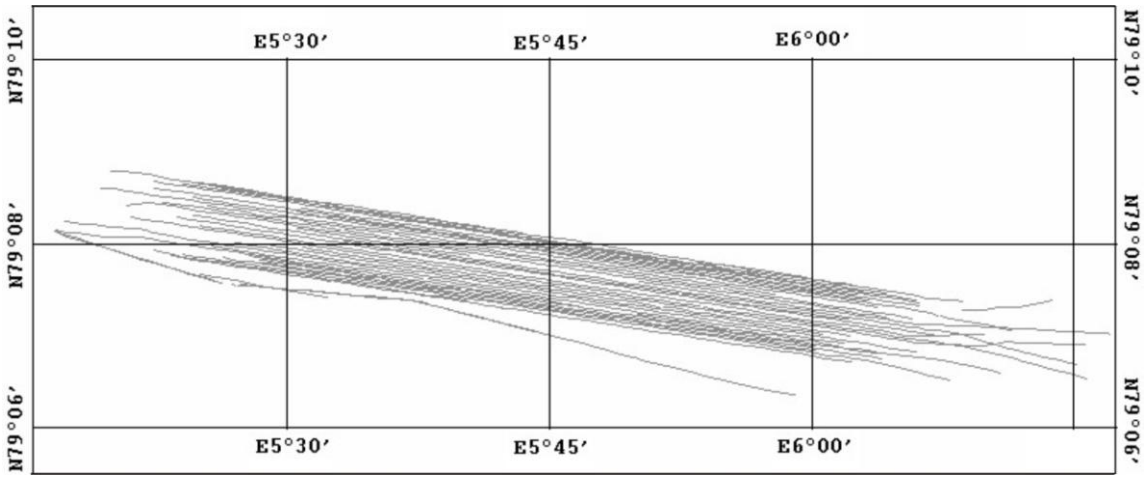

Figure 21: Lines are shown used for processing the 2007 multibeam survey. Approximately 40 m distance exists between each line (Snapshot from Neptune software)

3.2.1 BACKSCATTER

Backscatter strength is the intensity of the acoustic returns (Figure 22), which corresponds to the relative amount of energy send back from target, measured in decibels (e.g. Lindberg et al., 2007). The backscatter strength depends on the physical nature of the seafloor, structure and the characteristics of the acoustic pulse. The data are often useful for classifying seafloor bottom characteristics (Lurton et al., 2002).

Experience shows that soundings from multibeam do not always represent the seafloor surface. If the upper part of the seafloor sediments have a density which is close to the sea water density, the reflections may represent sediments as deep as 1 m below the seafloor with the use of frequencies close to 30Hz (Figure 22) (Blondel and Murton, 1997).

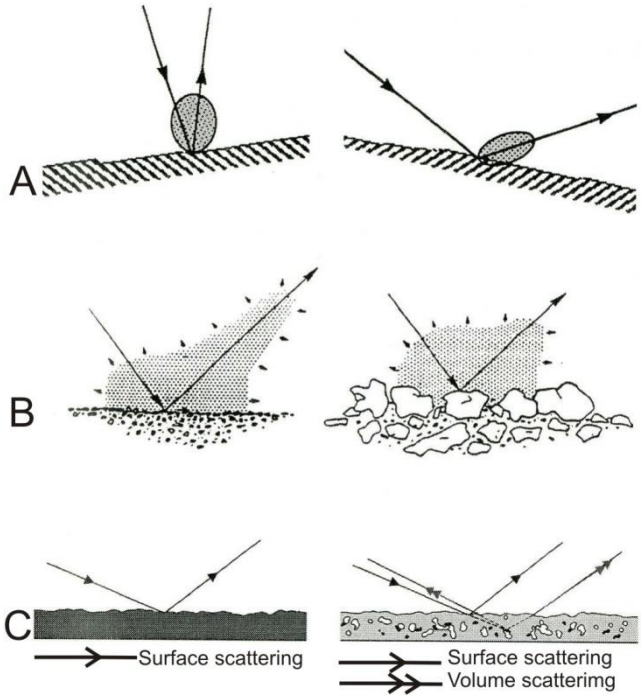

Figure 22: Backscatter from the seafloor is influenced by three factors: A) local geometry of area of coverage, B) roughness of the seafloor at scales comparable to the sonar's wavelength, C) intrinsic properties of the seafloor (Blondel and Murton 1997).

For a seafloor with gas hydrates (Johnson et al., 2003) backscatter is divided into 3 categories (Figure 23):

- Category I backscatter: High backscatter, due to presence of gas hydrates and authi genic carbonates.
- Category II backscatter: High backscatter but with a thin drape of sediments covering gas hydrates (if present) and authigenic carbonates.
- Category III backscatter: High to moderate backscatter that coincides with regions of high slope angles, associated with deep seated fluid flow but unrelated to destabilization of gas hydrate.

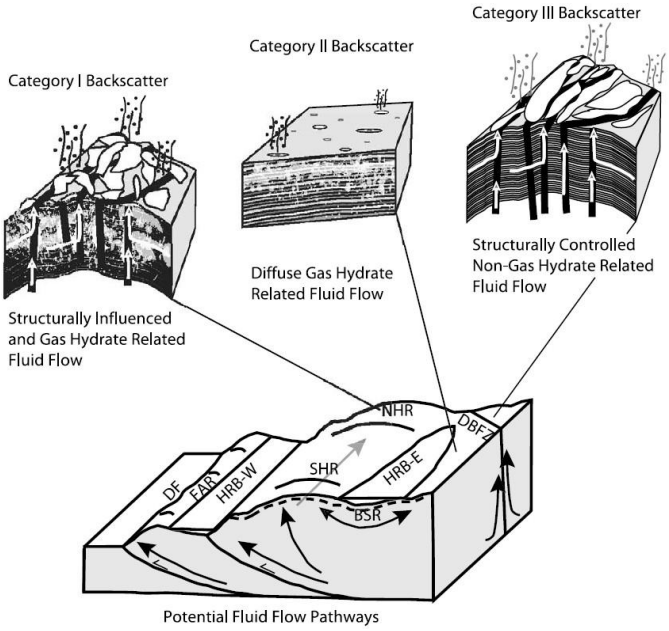

Figure 23: Classification of backscattering. Figure 11, from Johnson et al (2003).

3.2.2 GRIDBASED BATHYMETRIC ATTRIBUTE MAPS

Shaded bathymetry maps are used for imaging the seafloor that is usually illuminated from a chosen direction between 0° and 360°, with a azimuth of 0° to 90°. Attributes maps are useful for enhancing the fine-scale structure that is not well-revealed by the shaded-relief maps, while slope maps calculate changes in the slope direction and the angle of the slope.

3.3 SINGLE CHANNEL 2D SEISMIC

3.3.1 SEISMIC ACQUISITION

High-resolution 2D reflection seismic profiles oriented approximately parallel and perpendicular to the axis of the Vestnesa Ridge were acquired with R/V Jan Mayen (Mienert et al., 2006; Mienert et al., 2007)

High resolution 2D reflection seismic data was recorded with a single-channel streamer. The single channel streamer was towed at near-zero offset, slightly off track (Figure 24).

An array of two GI guns (G&I 2 x 40cc and G&I 2 x 105 cc) was used as a source for the 2D seismic acquisitions. The two GI guns are secured with chains 4 m under a frame (distance between them: ~1 m) and gun float (Figure 24).

The frequency nudge depends on the water depth and is calculated to be 180 Hz. A firing pressure of approx. 150 bars, a shooting rate of 10 sec, a sampling frequency of 2 kHz (0.5 ms) and a recording length of 2 s was used. The seismic signal recorded by the GI gun hydrophones can be continuously monitored. A trigger offset of 30 ms was used between G and I. (Mienert et al., 2006)

The 2D seismic reflection data was stored in SEGY format on hard disk using a Delph2 recording/processing unit on a Windows-based PC (Mienert et al., 2006).

In 2006 the GI array was towed 43 m behind the vessel, and the active part of the streamer was towed 29 m behind the GI array. During the 2007 survey the GI array was towed 32 m behind the vessel, and the active part of the streamer was towed 39 m behind the GI array, 11 m on the port side (Mienert et al., 2006).

The principal aims of the high frequency seismic recording are to image the morphology of the seabed in detail and its shallow sub-bottom sedimentary layers and structures related to gas hydrates (Mienert et al., 2006).

The acoustic penetration of the GI gun signal was limited due to free gas accumulation in deeper sediments and reached 0.6 s TWT. The signal-noise ratio was good and the overall quality of the records was very high (Mienert et al., 2006).

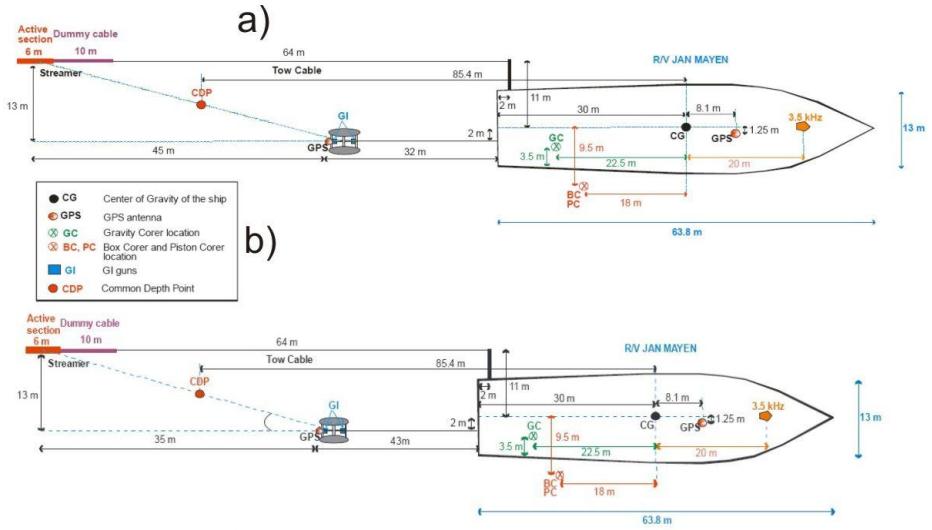

Figure 24: Navigation and configuration of sources, receivers, and GPS antenna, a) 2006 b) 2007

3.3.2 3300-HM HULL MOUNT SUB-BOTTOM PROFILER

Sub Bottom Profiler is used to gather data of the upper tens of meters beneath the sea floor. They are single beam sounders working with a frequency range from 1 kHz to 10 kHz. 3.5 kHz is the most common frequency (Lurton, 2002), and will give a (λ/4) vertical resolution of approximately 0.1m in soft sediments for both a velocity of 1600m/s and a velocity of 1500m/s. The function of a sediment profiler is to record echoes from the interfaces between sedimentary layers; these layers correspond to breaks in acoustic impedance, generating reflections of the acoustic signal (Lurton, 2002).

3.4 SEISMIC PROCESSING.

During the processing of the seismic lines the SEGY files was first imported into Promax where the geometry of the datasets was defined. Header statistics was applied to account for variations in the recording delay. Top muting was applied to remove noise in the water column.

A True Amplitude Recovery with the setting at 6dB/sec was applied to the dataset, which applies a single time-variant gain function to traces to compensate for loss of amplitude due to wave front spreading and inelastic attenuation.

An interactive spectral analysis was used to check the dominant frequencies on the seismic lines. Subsequently, the Butterworth bandpass filter was set to 25-30-170-200Hz.

Kirchhoff time migration was applied using a constant velocity of 1500 m/s. The objective of the migration is to remove diffraction hyperbola. After the migration, trace mixing and FX deconvolution was applied to reduce inline noise.

The trace mixing was used with weighted trace mix set to 1-3-5-3-1, which multiplies the horizontal trace samples within the trace mixing window by the given weights, sums the weighted samples, and normalizes this accumulated weighted sample sum by the sum of the weights.

F-X Deconvolution was used with a Wiener Levinson filter, which based on a statistical approach to filter out noise that has corrupted a signal. The F-X deconvolution applies a Fourier transform to each trace of an input ensemble or stacked data. It applies a complex, Wiener, unit prediction filter in distance for each frequency in a specified range, and then inverse transforms each resulting frequency trace back to the time domain.

(See flow chart at Table 2)

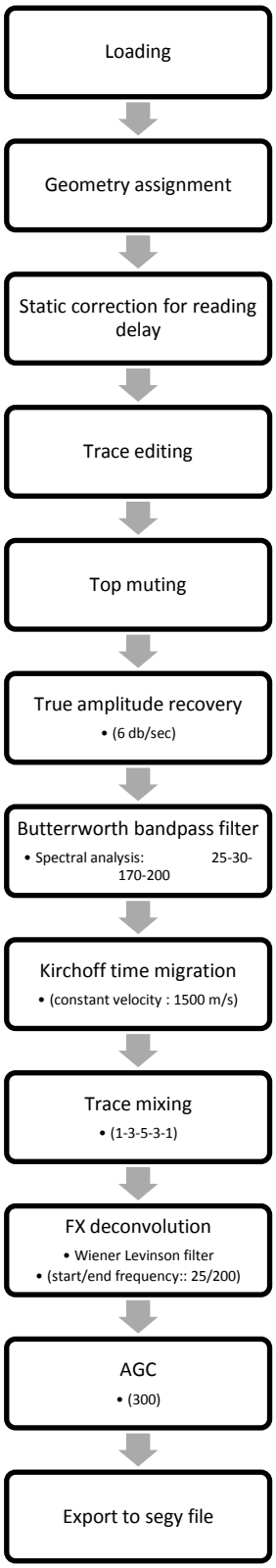

Table 2: Flow chart showing the main processing steps for single seismic reflection data.

3.5 SEISMIC RESOLUTION

Seismic resolution is a measure of how large an object need to be in order to be detectable by a seismic wave signal (Figures 25-27). The sound waves sent out from the source move in three dimensions and spread out over a larger area the further away it gets from the source. Normally depth is measured in milliseconds two-way travel-time, based on the time the sound wave needs from the source until it hits the reflector and returns to the receiver. With increasing depth the frequency of the sound signal will be attenuated, since the sediments are usually gradually more compacted with increasing depth, so that velocity and wave-length increase. Thus, the resolution of the seismic will decrease since higher frequencies are attenuated while lower frequencies reach further down (Figure 25) (Brown, 1999).

Vertical resolution is derived from the length of the sound-wave, that determines layers can be discerned when their thickness is below ¼ of the wavelength (Figure 25). The theoretically vertical resolution is usually given as $\frac{1}{4}\lambda$, were λ is the wavelength, but on real data the vertical resolution may often be between $\frac{1}{3}\lambda$ or even $\frac{1}{2}\lambda$ (e.g. Rafaelsen, 2000).

The horizontal resolution is derived from the Fresnel-zone, the part of a reflector covered by the seismic signal at a certain depth. On a buried horizon, all features with a lateral extent exceeding the Fresnel zone will be visible. Migration of the seismic data focus the energy spread in the Fresnel zone, re-arranges reflections misplaced due to dip, and remove reflection patterns from points and edges, which improves the horizontal resolution (Figure 25-27).

$$\text{Wavelength} = \lambda = \frac{V}{F}$$

$$\text{Vertical seismic resolution} = \frac{\lambda}{4}$$

$$\text{Fresnel zone before migration in m}^2 = \pi \sqrt{\frac{\frac{V \times T}{2} \times \frac{V}{F}}{2}}^2$$

$$\text{Fresnel zone after migration in m}^2 = \pi\left(\frac{\lambda}{4}\right)^2 = \pi\left(\frac{V}{4F}\right)^2$$

λ = wavelength

F = seismic frequency

T = depth in time

V = seismic velocity

Figure 25: Equations for calculating seismic resolution

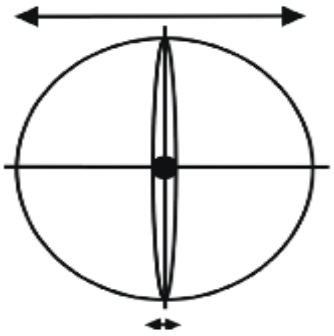

Figure 26: Fresnel zone before (large circle) and after (elliptical circle) migration (Brown, 1999).

	wavelength	Vertical resolution	Unmigrated Fresnel zone	Migrated Fresnel sone
Above BSR at 1.9 s, assumed velocity of 1550 m/s	12m	3 m	27755 m^2	28 m^2
Below BSR at 2.1 s, assumed velocity of 1650 m/s	23.6m	5.9m	64225m^2	109m^2

Figure 27: Seismic resolution calculated. Frequency of 130Hz is used for the layers above BSR, and frequency of 70Hz is used for layer below BSR.

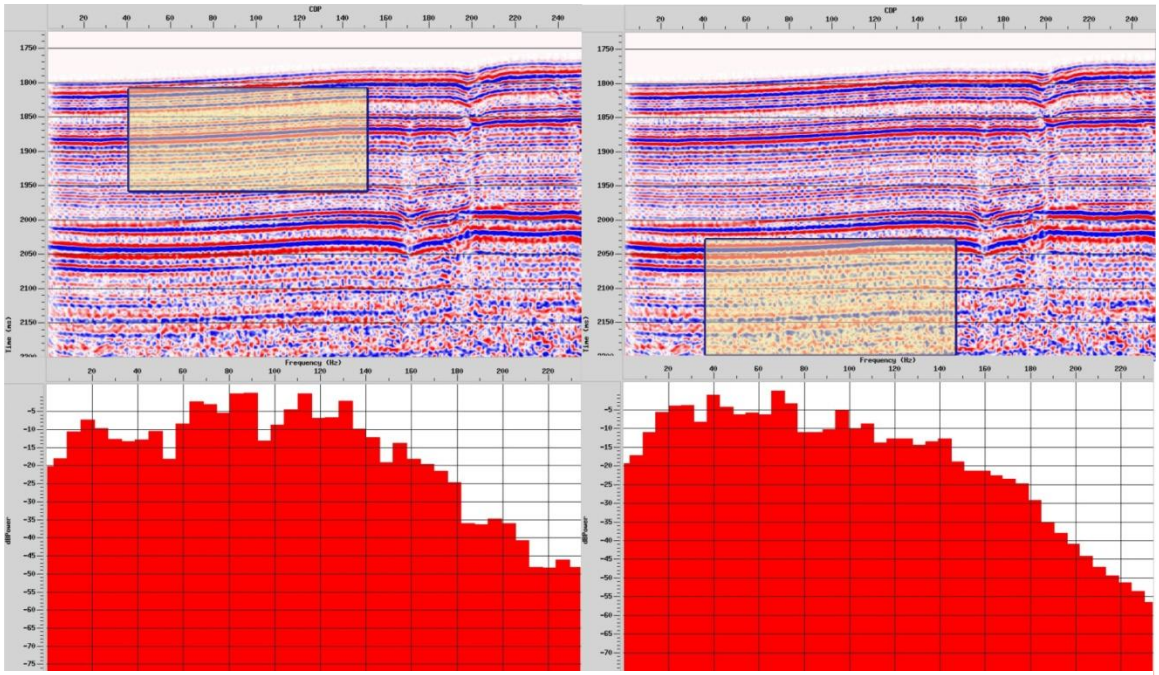

Figure 28: Frequency above and below BSR on line 215 at Vestnesa Ridge. The spectral analysis above the BSR (to the left) shows an abrupt frequency near 130Hz, while the spectral analysis below the BSR (to the right) shows a frequency drop close to 70 Hz.

3.5.1 SEISMIC FREQUENCY ANALYSIS

Figure 28 shows that the frequency range is clearly higher in the area above the BSR than in the area below the BSR. That is caused by an abrupt velocity decrease when the signal passes into the zone with free gas beneath the BSR. The free gas zone works as a filter that decreases the energy of high frequencies. On all the seismic sections that is used in this master thesis, the same effect can be seen, which causes a change in seismic resolution from above to below the BSR. Most of the seismic signal below the BSR shows a low frequency. Thus, it makes it almost impossibly to determine any high resolution reflection data beneath the BSR further down. As a result, the analysis of the data of this master thesis concentrates on sections above the BSR, i.e. from 200- 250 ms TWT below the seafloor to the seabed.

4 RESULTS

4.1REGIONAL SWATH MULTIBEAM DATA GRIDDED TO 50 M

Figure 29 shows the regional swath bathymetry of the study area that allows identifying the shelf edge with bmoraine ridges at ~200 m water depth and the Kongsfjorden Trough mouth fan. Between the Kongsfjorden Trough mouth fan in the east and the more than 3000 m deep Molloy transform fault in the west lies the northwest elongated Vestnesa Ridge at 1200 m water depth. On the approx. 100 km long Vestnesa Ridge a string of densely distributed individual pockmarks marks the crest of the ridge (Figures 30-31). The depth profiles on Figure 30 show that the part of Vestnesa Ridge covered by profiles is approximately 73 km long and between 1– 4 km wide. The swath bathymetry gridded to 50 m shows that the ridge widens from south-east until the Vestnesa Ridge bent towards the west, where it gradually starts to get narrower further westward. An estimate of the crest area provides 250 km^2 assuming an average width of 2.5 km and a length of 100 km.

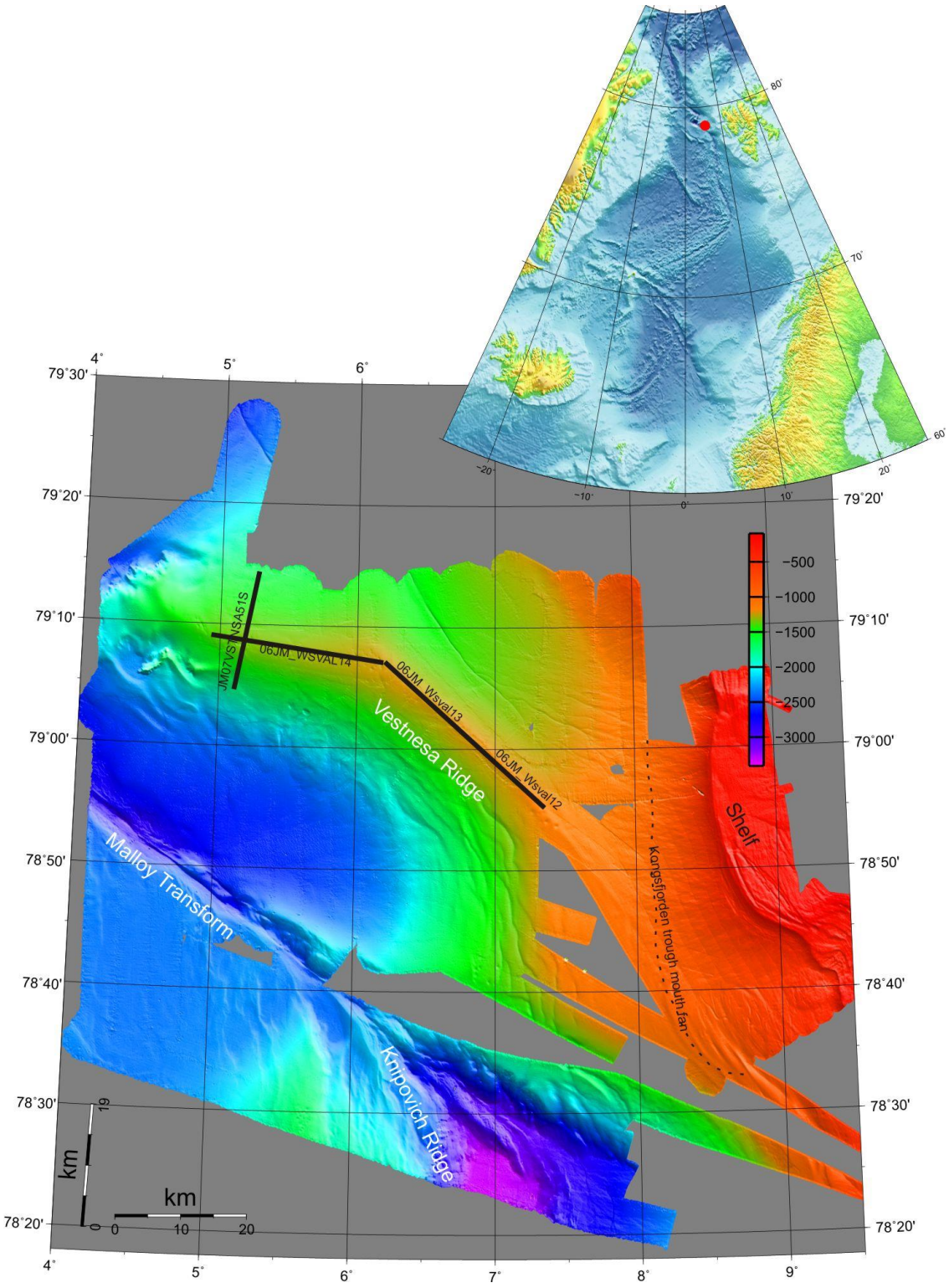
79°30'
79°20'
79°10'
79°00'
78°50'
78°40'
78°30'
78°20'
4°
5°
6°
7°
8°
9°
−500
−1000
−1500
−2000
−2500
−3000
06JM_WSVAL14
06JM_Wsval13
06JM_Wsval12
Vestnesa Ridge
Shelf
Kongsfjorden trough mouth fan
Molloy Transform
Knipovich Ridge
km
0
10
20

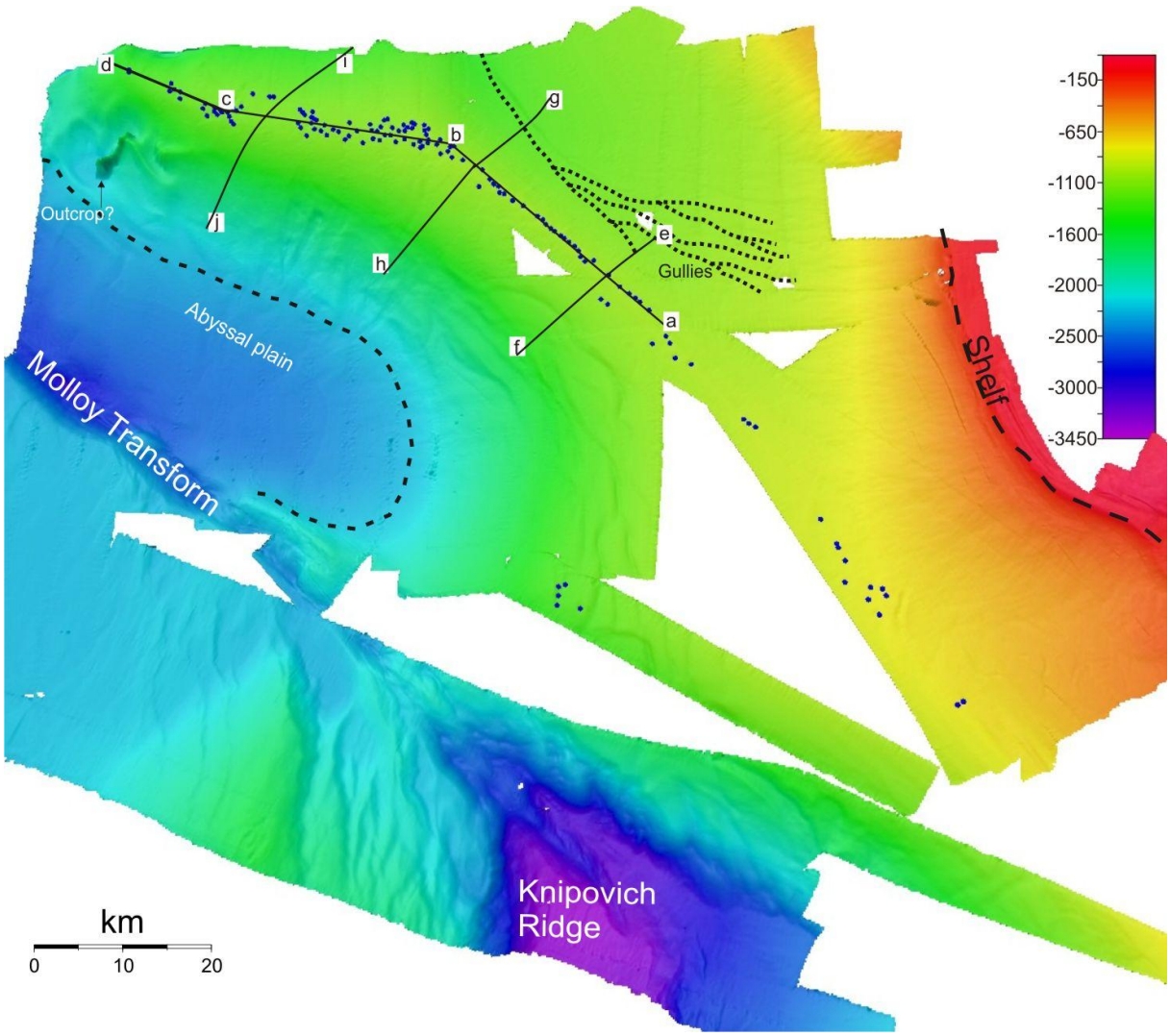

Figure 30: Swath bathymetry of the Vestnesa Ridge gridded to 50 m were the pockmarks are marked with blue dots.

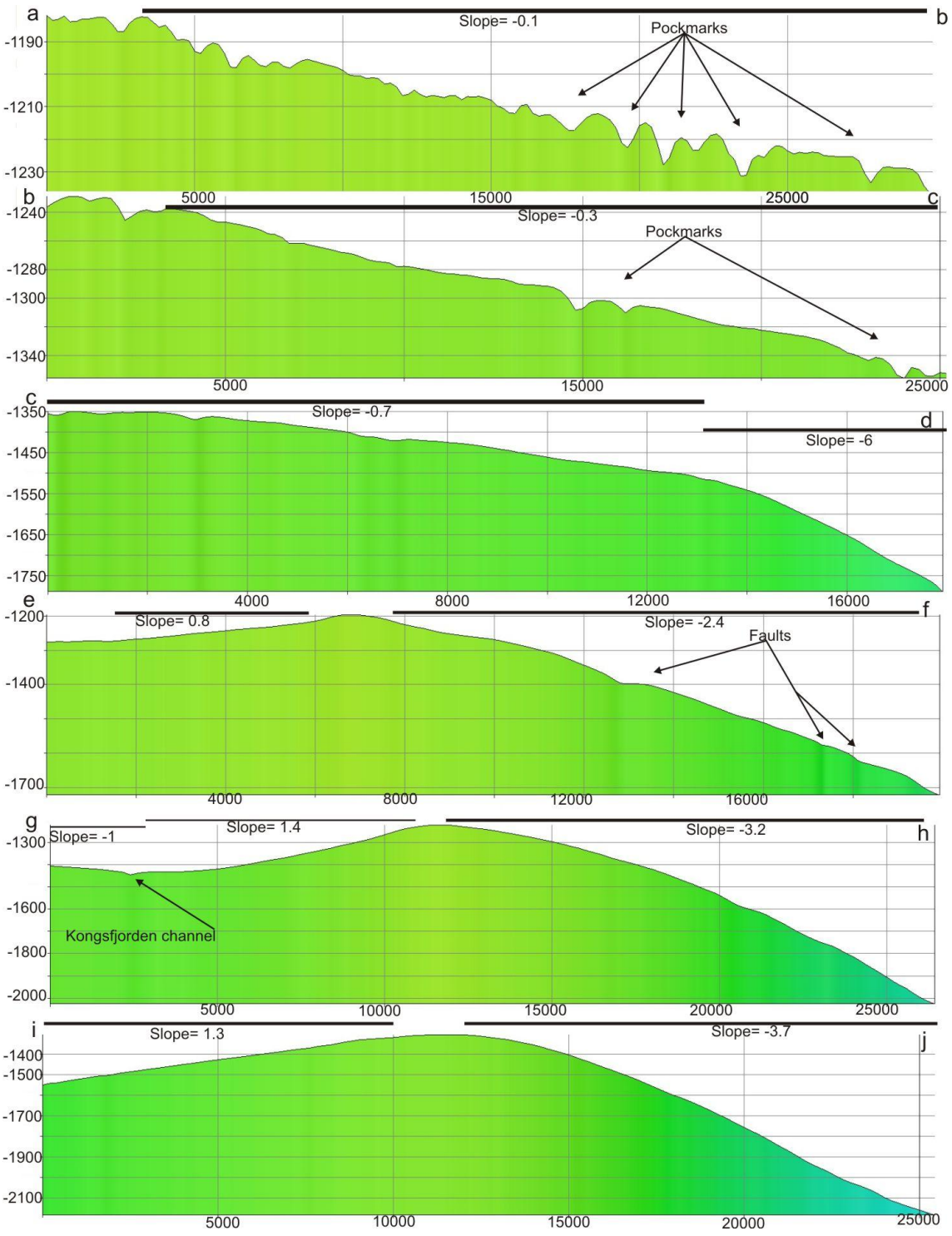

Figure 31: Depth profiles a-b, b-c and c-d follows parallel to Vestnesa Ridge, profiles e-f, g-h and i-j are transverse to Vestnesa Ridge. Locations of profiles are shown on figure 30.

The mean slope angle of the Vestnesa Ridge is 0.1° from south-east towards the area where it turns westward. Here the slope angle gradually increases from 0.3° to 0.7° until it rapidly increases to 6° at the most western part of the Vestnesa Ridge (Figure 31).

The southern slope angle increases (Figure 31, depth profiles e-f, g-h and i-j) from the south-eastern area of the ridge (2.4°) to the south-western part where it gradually increases towards 3.7°.

The northern slope of the Vestnesa Ridge is more gentle and starts with a slope angle of 0.8° in the south- eastern part and increases to 1.4° (Figure 31, depth profiles e-f, g-h and i-j) in the western area.

A total of 133 pockmarks have been identified (Figure 30) and all of them are situated on the crest of Vestnesa Ridge. On the south-eastern part of the Vestnesa Ridge, where the crest is becoming narrower, the pockmarks line up perfectly along the apex of the crest (Figure 30 and 32). On the western part of Vestnesa Ridge the crest gets wider, and the distribution of pockmarks shows over a wider area as well. When the crest gradually becomes narrower towards the west, they are again aligned in a narrow string (Figures 29 and 31).

According to a first inspection of the depth profiles of figure 30, the pockmarks on the south-eastern side of Vestnesa Ridge appear to be more numerous and larger compared to the western part.

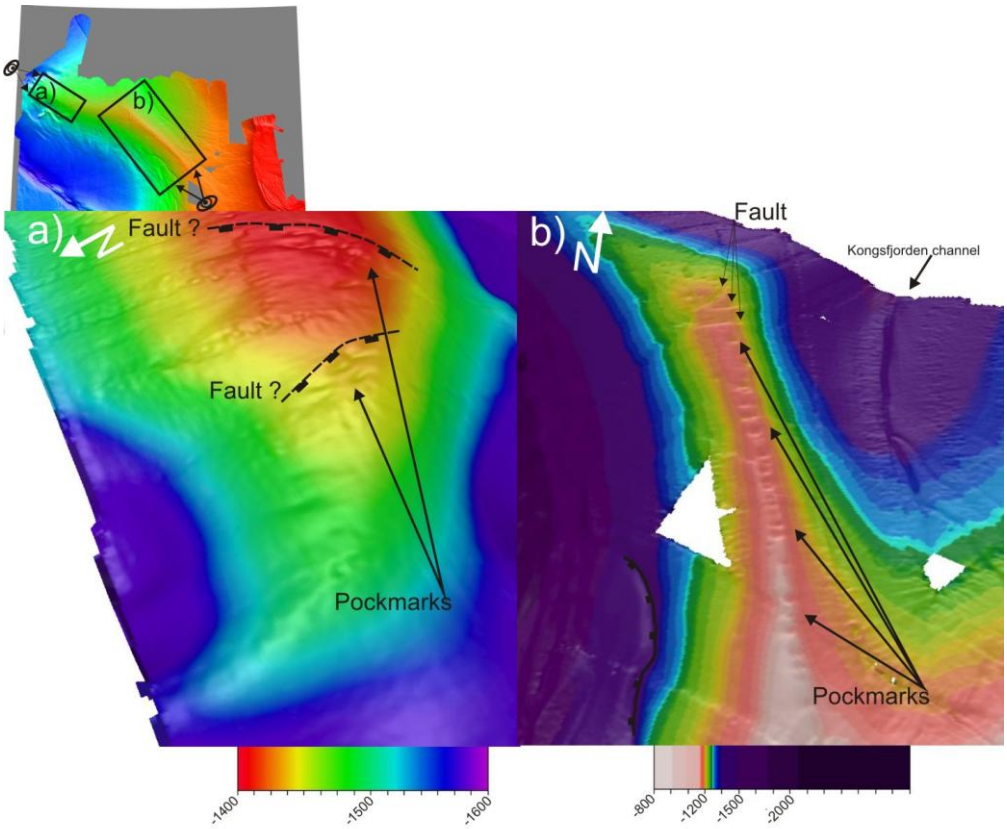

Figure 32: a) Swath bathymetry viewed from west showing the western part of Vestnesa Ridge where circular to elliptical seafloor depressions can be identified. b) Swath bathymetry viewed from south- east of Vestnesa Ridge. White areas are data removed during processing due to acquisition noise.

Figure 32a shows the westernmost pockmark fields. These pockmarks are mainly aligned in a string with a few pockmarks outside of it, which might indicate a relationship to faults. Figure 32a indicates also a change in the slope gradient, which may indicate faults that rupture and deform the seafloor.

It is important to note, that the south-eastern part of Vestnesa Ridge (Figure 32b), shows pockmarks that are perfect aligned on the apex of the crest, where the swath bathymetry gridded data (50 m resolution) point not towards a fault related origin. However, where the Vestnesa Ridge turns towards the west, three areas close to each other can be identified that indicate faults rupture and related deformation of the seafloor (Figure 32b). There is also a change in the slope gradient and this area will be described in more detail below (chapter: 4.4.2.2 Faults).

4.2 HIGH RESOLUTION SWATH BATHYMETRY DATA (GRIDDED TO 15 M)

The detailed swath bathymetry map (Figure 33) presents and area of approximately 110 km^2 (20 × 5.5 km). The mean slope angle from east to west is 0.2 °, and across the eastern part the gradient is 0.3° on the northern slope, and close to 0.5° on the southern slope. Further westward the gradient increases gradually and is steepest at the southern (1.3°) and northern flank (0.9°).

Figure 33a and d present 44 circular to elliptical pockmarks with depressions up to 15 m and a maximum axis up to 1000 m. Pockmarks are either connected to each other with 2 or more individual pockmarks, or scattered around as single pockmarks. The pockmark density in the study area based on the high resolution swath bathymetry (gridded to 15 m) is 0.4 pockmarks per km^2 (Figure 33a).

Figure 33b shows the slope gradient of the pockmark area. The main trend is obvious where the slope is steepest toward the crest of the Vestnesa Ridge. Pockmarks that are situated in flat areas of the ridge have a slope gradient that appears to be similar in all directions

Figure 33c indicates the variety in the specific backscatter pattern of pockmarks. Clearly, all high backscatter spots, except for one, correlate with pockmarks. The areas with high backscatter seem to be either in the centre of the pockmarks or on the pockmark rim. The slope gradient or the shape of the pockmarks does not appear to be relevant for the backscatter.

One area with high backscatter does not correlate with any visible pockmarks either on the swath bathymetry map or the slope gradient map (Figure 33).

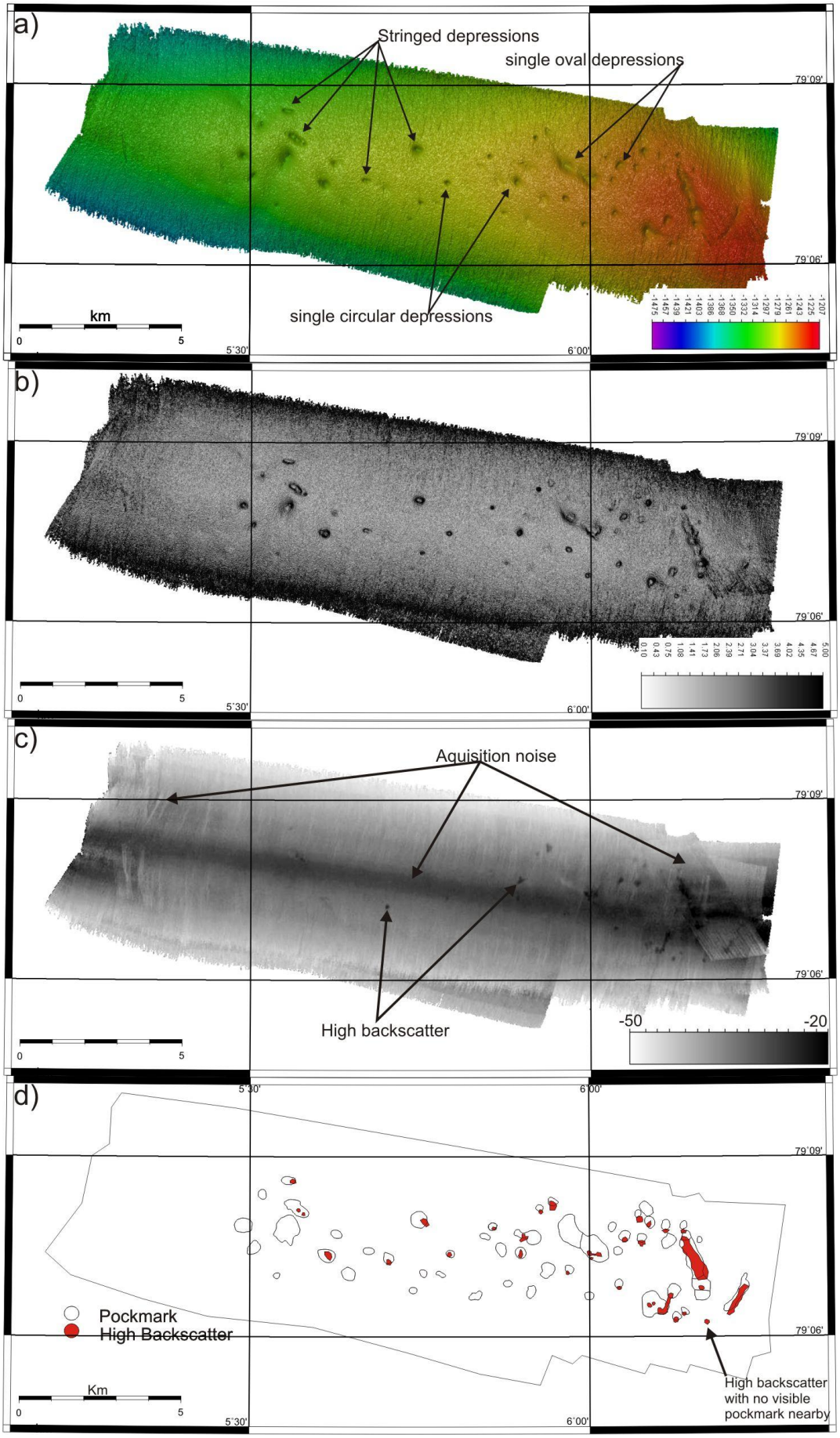
a)
Stringed depressions
single oval depressions
single circular depressions
km
0
5
5°30'
6°00'
79°09'
79°06'
b)
c)
Aquisition noise
High backscatter
-50
-20
d)
Pockmark
High Backscatter
Km
High backscatter with no visible pockmark nearby

Figure 33: a) High-resolution swath bathymetry map (resolution 15 meter). b) Slope gradient map generated for 0-5 degrees (white-black). c) Backscatter map where dark areas have a high backscatter, and white areas have a low backscatter. d) Interpretation of swath bathymetry data showing the relationship between pockmarks and areas with high backscatter (based on figure 33 a, b and c).

4.3 QUANTIFICATION OF POCKMARK DIMENSIONS

This subchapter presents a very detailed study of pockmarks. It was achievable due to the high-resolution swath bathymetry (gridded to 15 m) collected during the 3D seismic survey. The axis, depths and orientation of pockmarks have been measured and treated with basic statistical methods.

As shown in figure 34, there is a significant difference in both width and depth of the seafloor depressions depending on the achieved grid resolution. The major difference is due to smoothing effects during interpolation of the data during gridding. Pockmark 5 is a good example since it is gridded to 50 m and 15 m. As a result, the depressions are wider and shallower in the swath bathymetry gridded to 50 m, if compared to 15 m.

Figure 34 (a-2), four depressions gridded to 15 m: Pm 5, Pm 12, Pm 13 and Pm 14. Figure 34 (a-1) shows the same area but gridded to 50 m, and here only Pm 5 and 14 can be identified with confidence. Pockmarks 13 and 14 may just as well be within the noise, or an undefined feature in the dataset, instead of distinct depression related to a pockmark.

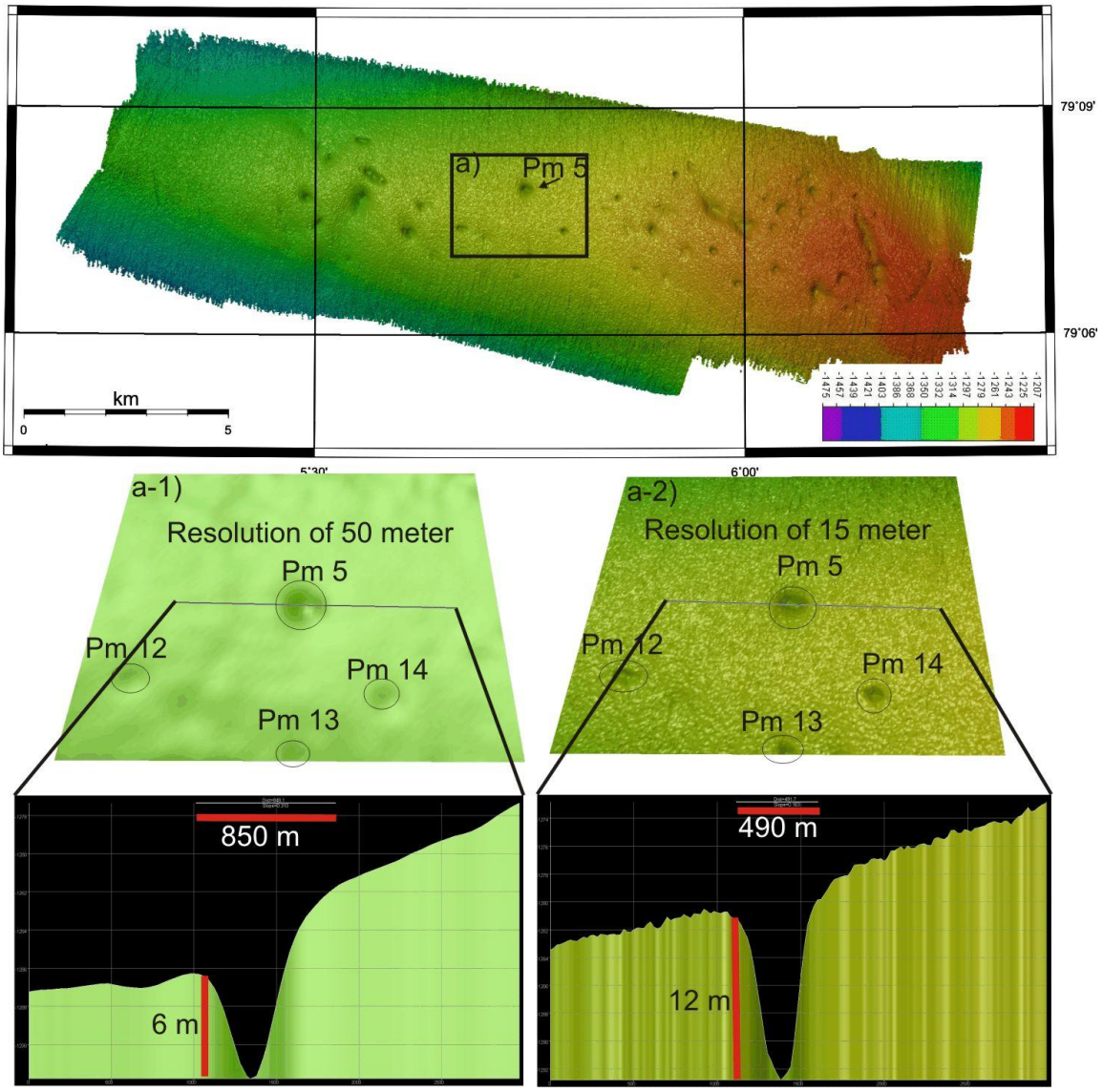

Figure 34: Swath bathymetry gridded to 50 meter versus swath bathymetry gridded to 15 meter. The swath bathymetry gridded to 50 m shows that the signal is more interpolated making the pockmarks both shallower and wider compared to the swath bathymetry gridded to 15 m which shows a more spiked signal.

Therefore, the x-y ratio and other measurements that are affected by the size and depth of the pockmarks were only based on data retrieved from the high-resolution swath bathymetry gridded to 15 m and not from swath bathymetry gridded to 50 m.

4.3.1 POCKMARK DIMENSIONS

Generally, the majority of mapped pockmarks appear to show shapes from circular to elliptical with ratios (length of long axis/length of short axis) in the range from 1 to 2.4 with a mean value around 1.4 (Figure 35, 36 and 37). The absolute size of the long axis varies from approximately 150 to 1000 meter while the short axis varies from approximately 100 to 680 meter (Figure 35).

The average pockmark has a long axis of 390 meter and short axis of 276 meter (Figures 35-36). The depth varies between 1 and 15 meter, with an average depth of 6.5 meter (Figure 37). An average pockmark therefore represents a volume of expelled material of approx. 0.00135 km^3. Since a total of 44 pockmarks have been mapped in the study area (Figure 33) the volume of possibly expelled material may amount to approximately 0.056 km^3. This material may be picked up by bottom water currents, and the orientation of the long axis for all depressions may therefore be influenced by the direction of the bottom currents.

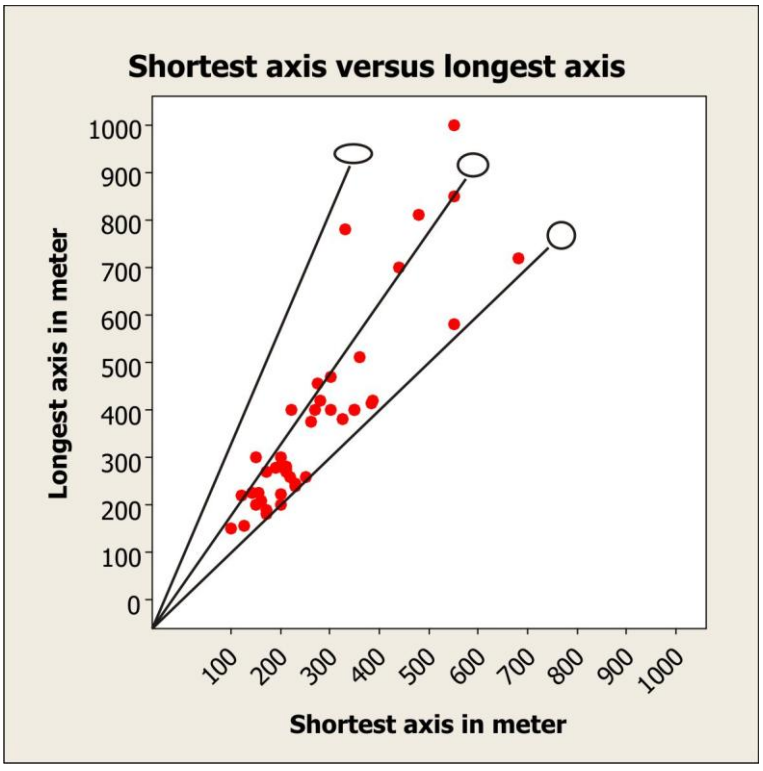

Figure 35: Axis of pockmarks plotted against each other, classified after shape. Circular (y=x), elliptical (y=0.75x) and elongated (

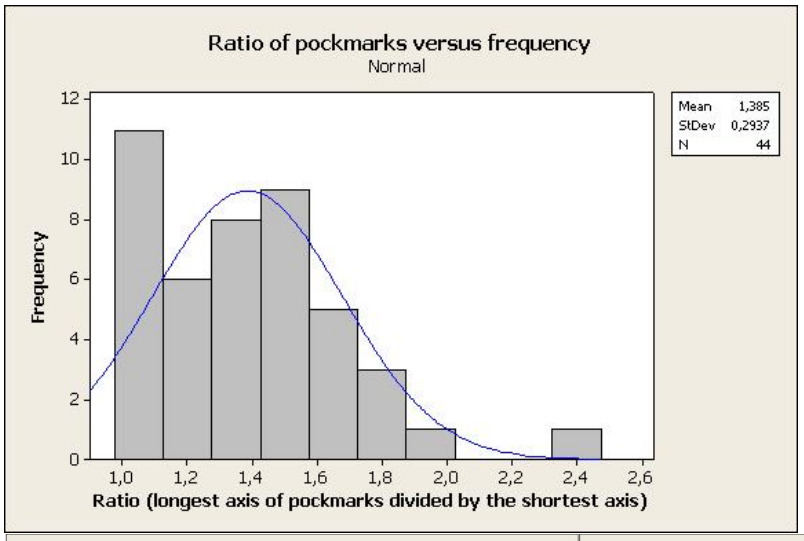

Figure 36: The longest axis was divided by the shortest axis. If the ratio of a given pockmark is 1 it is circular, the higher the ratio is for a given pockmark, the more elongated the pockmark is. This graph shows that the average pockmark in the study area have a ratio of 1.4, giving it a shape of semi circular.

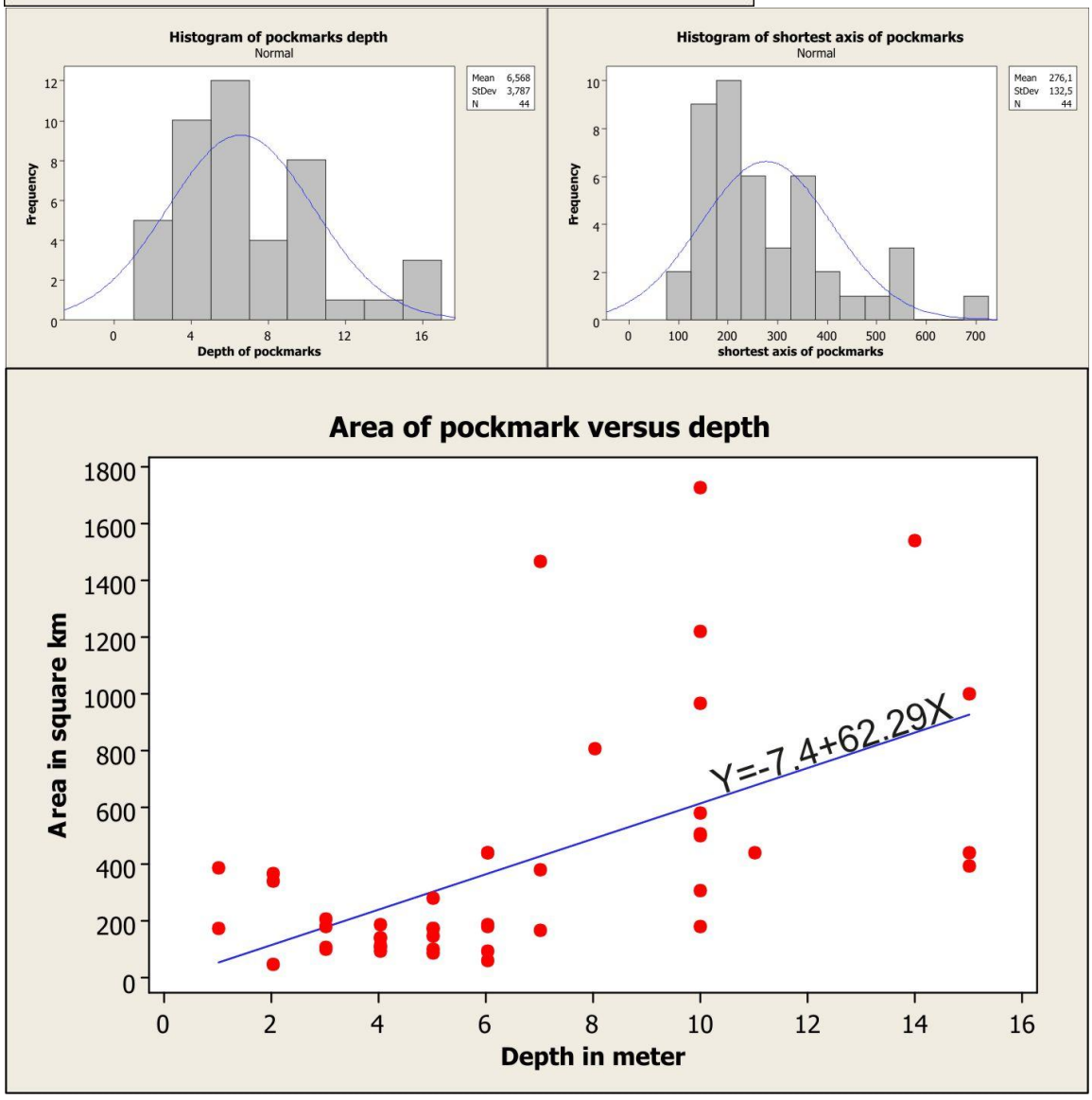

Figure 37: The shortest axis and depths of 44 pockmarks are plotted versus each other. The mean axis is 276 m long; the mean depth is 6.5 m.

The rose diagram shows a preferred orientation of N-S, if stringed pockmarks are included (Figure 39). If the stringed pockmarks are excluded the results obviously show no clear preferable orientation of the long axis of pockmarks.

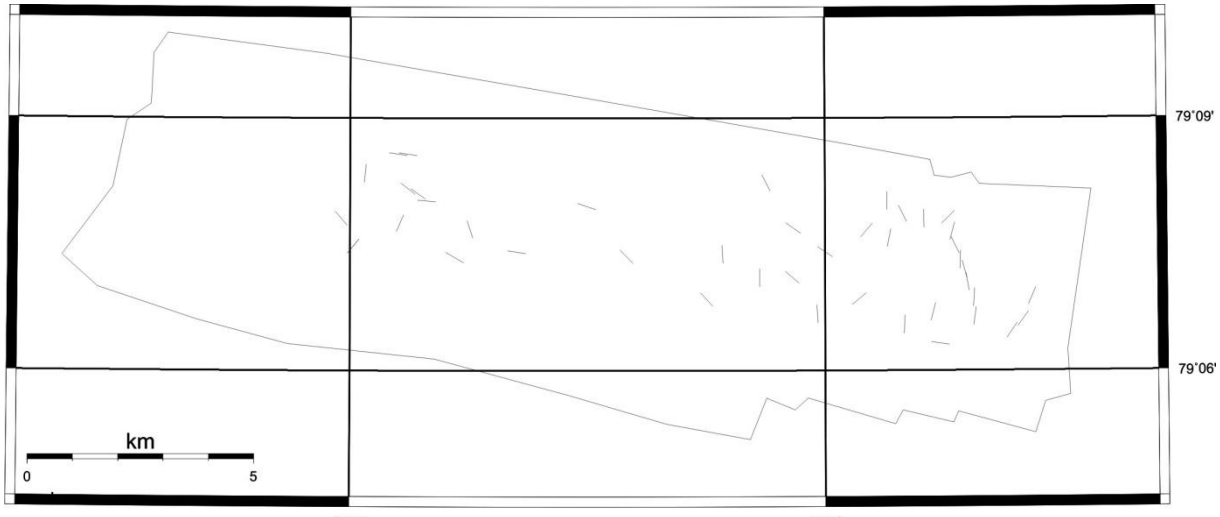

Figure 38: Estimated azimuth of pockmarks used to calculate the rose-diagram (Figure 39).

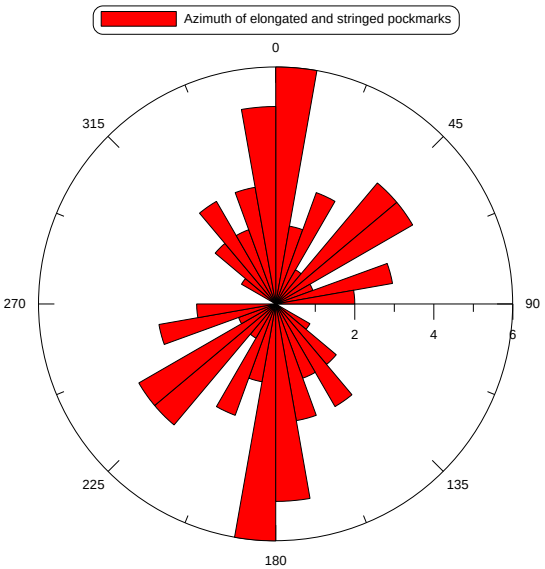

Figure 39: Bidirectional rose- diagram with a bin size of 10°, showing the azimuth of elongated pockmarks, estimated from figure 38.

4.4 GENERAL INTERPRETATIONS

4.4.1 BSR

Seismic line JM07VSTNSA51S (Figure 43) shows several high amplitude reflectors that terminate at an apparently overlying reflection at the southern area at approximately 200 ms below the seafloor. It mimics the seafloor and coincides with the base of the hydrate-stability zone in this area (Vanneste et al., 2005). The reflection has a reversed polarity if compared to the seafloor reflection. The polarity reversal of the reflector mimicking the seafloor is typical for a BSR at the base of the gas hydrate stability zone (BGHSZ), and is interpreted to be a free-gas bottom simulating reflection (Vanneste et al., 2005). The BSR is caused by the strong impedance contrast between partially hydrated sediment above and gas charged sediments beneath it.

The bottom simulating reflector (BSR) is only disrupted by chimney structures, and cross cuts the layering where the layering is not parallel to the seafloor. In areas where the reflection follows the strata the BSR is difficult to recognize, but its depth can be estimated due to the underlying enhanced amplitude reflections of the free gas zone.

In the northwestern part of Vestnesa Ridge (Figures 42- 43), the BSR may exists at 200 ms below the seafloor. By tracing it in the seismic lines towards the south-east the BSR is gradually deepening to 240 ms, i.e. with an increasing distance from the mid ocean ridge (Figure 40).

Seismic lines that are acquired parallel to Vestnesa Ridge axis (Figure 40, 41 and 42,) show that the BSR is running continuously parallel to the seafloor reflection with high amplitude reflections beneath. The high amplitude reflections below the BSR are interpreted to be free gas, which have accumulated beneath the GHSZ. The gas accumulation zone is believed to be in excess of 150 m due to the thickness of the zone with enhanced reflections (Bünz et al. 2008). Below the enhanced reflections an acoustic turbidity zone exists due to the highly attenuated seismic signal in gas charged sediments.

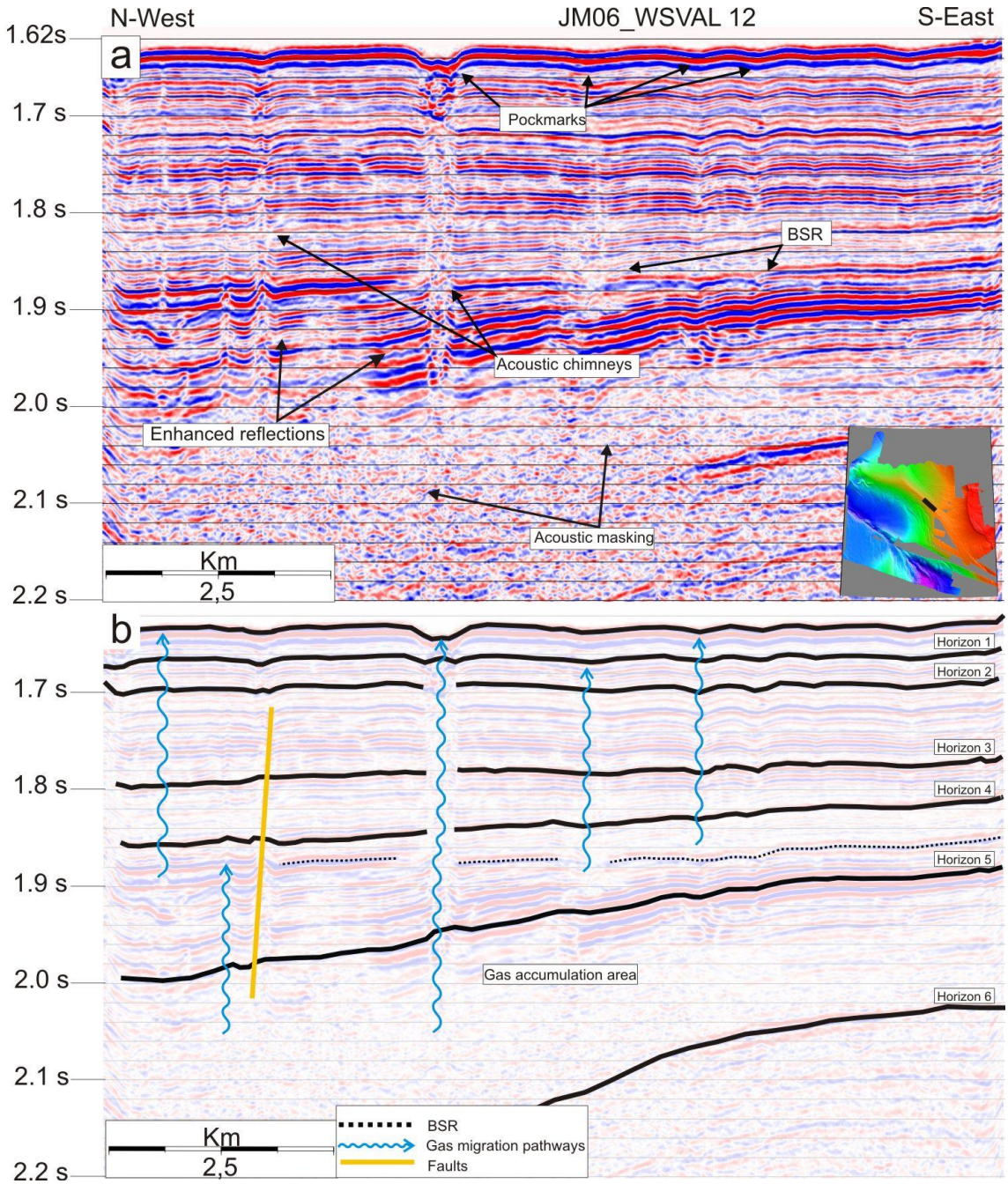

Figure 40: a) High-resolution single channel seismic line shows seafloor fluid expressions connected to chimneys piercing the GHSZ and strata formations at the Vestnesa Ridge (for location see Figure 29). b) The seafloor reflection is dipping very gentle towards the northwest; horizon 1 and 2 are parallel to the seafloor. Horizon 3 and horizons beneath are gradually deepening towards the northwest. High amplitudes mark the time interval beneath the BSR between 1.88 and 2 sec TWT. The BSR is hardly recognizable but the high amplitude zones indicate the ags accumulation beneath the BGHSZ. The acoustic chimneys can be traced from the seabed and down trough horizon 5 but beneath they cannot be imaged due to the high acoustic turbidity.

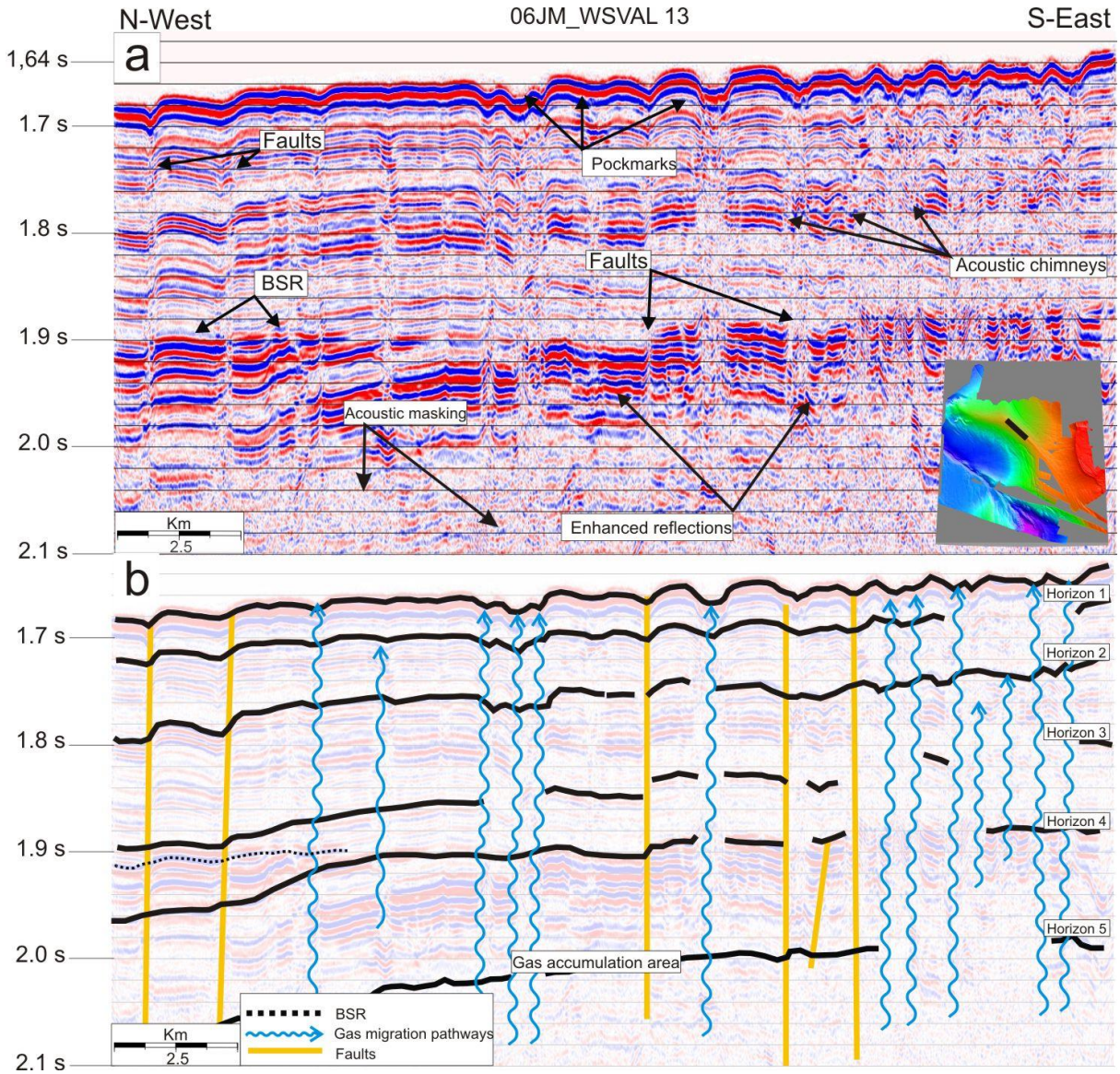

Figure 41: a) High-resolution single channel seismic line showing the relationship between the seafloor topography, faults, BSR, chimneys piercing the GHSZ, and the seismic stratigraphy geometry, at the the Vestnesa Ridge (see Figure 29 for location). b) The seafloor reflection is dipping gently towards N- west; horizon 1 and 2 are parallel to the seafloor. Horizon 3 and the horizons beneath are dipping gradually deeper the further down they are in the TWT seismic section. The acoustic chimneys can be traced trough horizon 5, where they disappear due to acoustic turbidity.

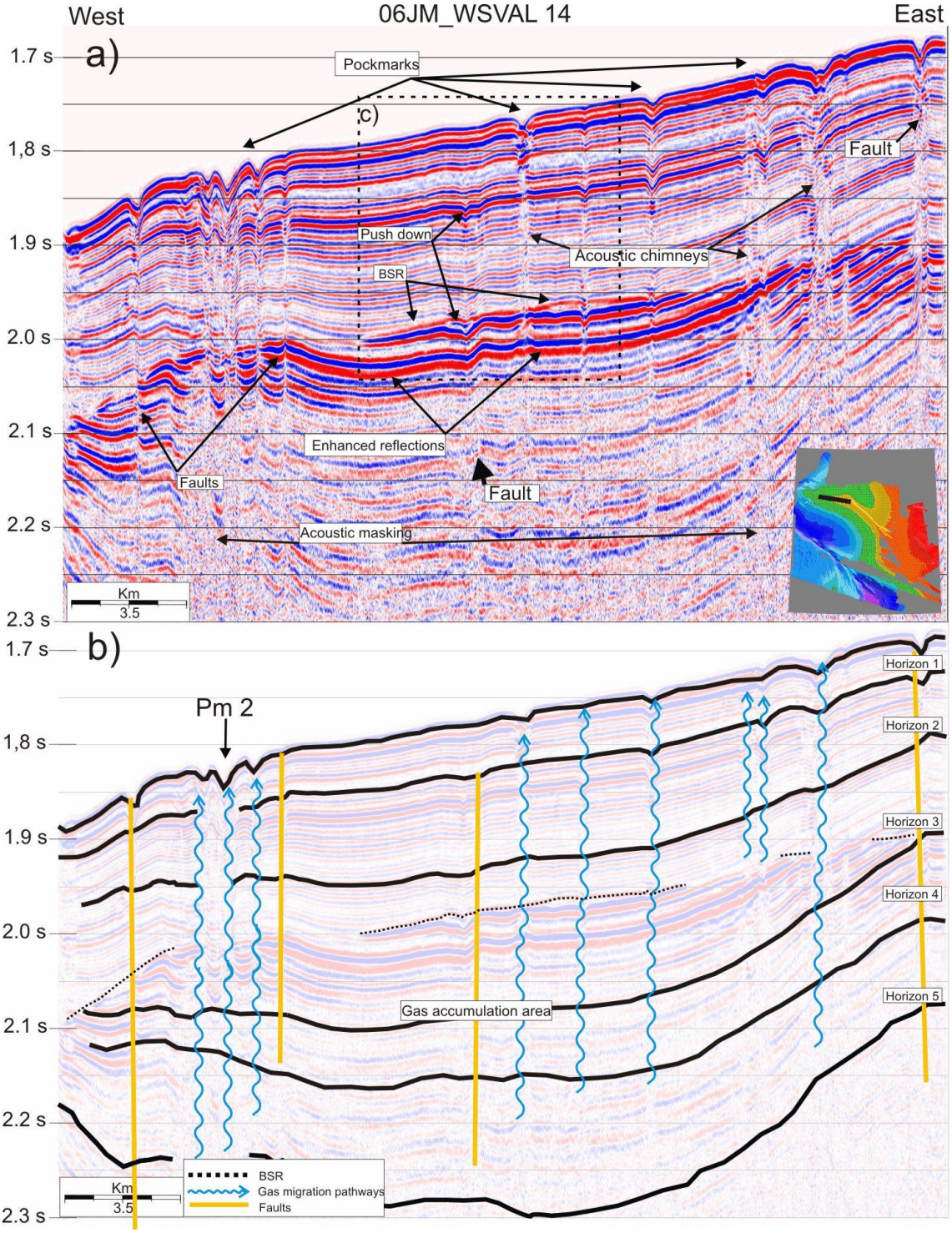

Figure 42: a) Single channel seismic line showing the influence of the faults and chimneys pierces the GHSZ on the seafloor topography of the Vestnesa Ridge (for location see Figure 29). Note that Seismic line 06JM_WSVAL 14 has a a direction towards the west. The seafloor reflector is dipping towards the west.. High amplitudes are clearly visible beneath the BSR. Horizons 2 to 5 are dipping towards the west but become flattened towards the western tongue of the drift. At the western part a concentration of faults occur. Horizon 5 dip upward while horizon 3 and 4 appear to merge. Individual pockmarks occur above several faults that penetrate horizon 5. They are separated by approximately 6 km from the pockmark fields located further east.

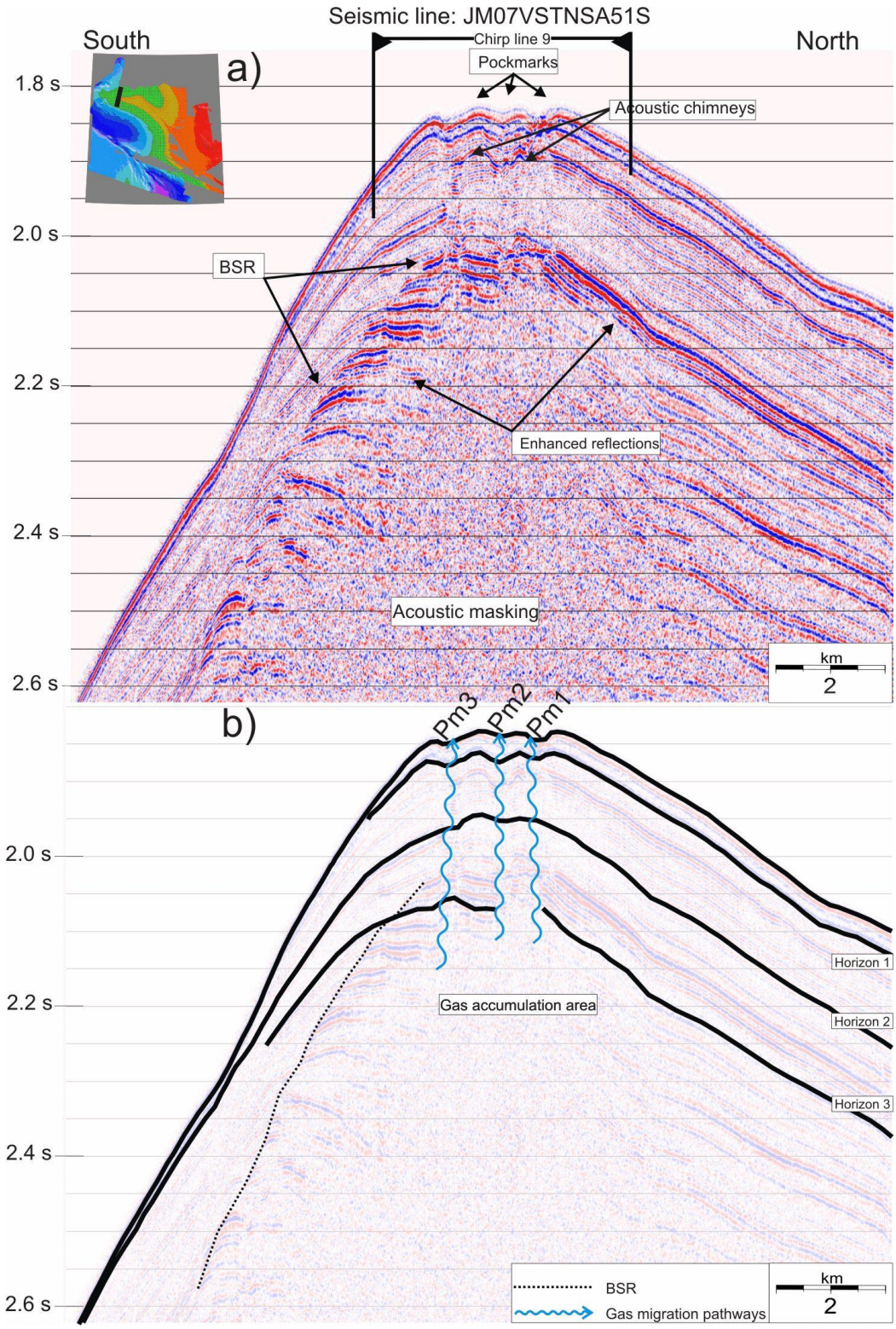

Figure 43: a) Single channel seismic line showing the relation between the seafloor topography, the strata-geometry, the BSR and high amplitude reflectors beneath it, and chimneys piercing the GHSZ at the top of the Vestnesa Ridge (for location see Figure 29). A high resolution chirp profile was shot parallel to the seismic acquisition and the approximate depth penetration and position is marked on top. b) Seismic line JM07VSTNSA51S crosses seismic line 06JM_WSVAL 14 at pockmark 2. Acoustic turbidity hinders to trace the lowermost horizons but the uppermost horizons 1,2and 3 are traceable. The acoustic chimneys can be followed trough both the BSR and the enhanced reflectors.

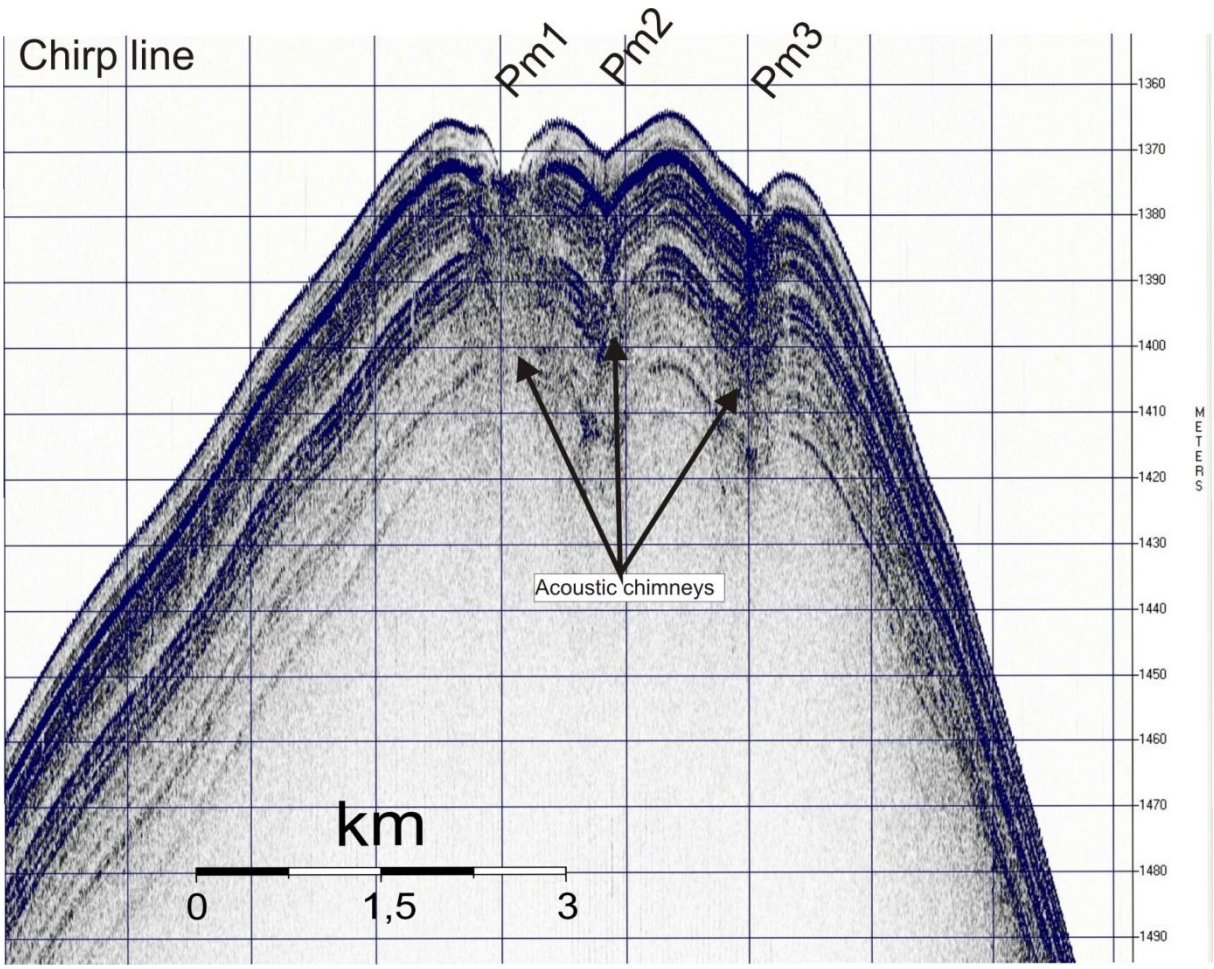

Figure 44: Very high resolution chirp line showing the upper 30 m of sediments (see figure 43 for location).

4.4.2 FLUID FLOW STRUCTURES

Indications for vertical fluid flow exist at the Vestnesa Ridge particularly at the crest of the ridge in form of acoustic chimneys in the sub seabed connected to pockmarks at the seabed. Some of these fluid flow expressions may be related to faults.

4.4.2.1 ACOUSTIC CHIMENYS AND POCKMARKS

In the presented seismic lines of Vestnesa Ridge (Figure 40- 44) more than 40 vertical migration pathways for fluids can be observed. They resemble a great variation in size and seismic signatures, such as high amplitude reflections and intervals of dimmed zones and may indicate an active fluid migration system.

Acoustic chimneys do in most cases end in a pockmark at the seafloor. There are also examples where acoustic chimneys do not penetrate the seafloor (Figure 45c_b).

Size and shape of the acoustic chimneys vary greatly on Vestnesa Ridge. They can appear in different shapes and diameters where the broad end may be pointing either upward or downward. Other acoustic chimneys appear more as a straight pathway. Some of them are interrupted, and fluids seem to move laterally within layers, until the next chimney connects to the upper layers (Figure 42).

The width of acoustic chimneys studies may vary from more than 1000 m to less than 100 m, even within the same acoustic chimney (Figure 42). The source area is impossible to identify due to the acoustic turbidity zones beneath, but they may start within these potentially free gas areas.

Shallow enhanced reflectors are common in the acoustic chimneys (Figure 40, 41 and 42), and so are also dimmed areas. Acoustic artifacts such as push down and pull up effects within the acoustic chimneys may suggest high or low velocity anomalies, respectively (e.g. figure 41 and 42).

In many of the acoustic chimney the seismic reflectors are disrupted or discontinuous (Figure 42), and these acoustic chimneys show often enhanced reflectors further up in the section suggesting an active fluid seepage system. Other acoustic chimneys have continuous reflectors, often with a push down effect (Figure 40, 41 and 42), which may be caused by high gas contents within the sediments, or a velocity anomaly caused by soft sediments accumulated within in the pockmark (Bradley, 1985).

4.4.2.2 FAULTS

There are several locations on seismic lines 06JM_WSVAL 12, 06JM_WSVAL 13 and 06JM_WSVAL 14 where seismic reflectors are interrupted and displaced vertically (Figure 40, 41 and 42).

These displacements are suggested to indicate normal faults (Badley 1985).

All normal faults that have been identified in the study area seem to penetrate the seafloor, or at least reach the most upper part and stop beneath the seafloor. These faults penetrate both the BSR and the high amplitude zone reaching a total length of approx. 500 ms TWT or

even more since the acoustic turbidity zone hinders solid identifications. There are also some indications of smaller normal faults, or displacements on the chirp lines (Figure 45)

At the seafloor, these faults seem to stimulate the development of pockmark clusters, either in a string, where several pockmarks grow together, or as individual features in a line (e.g. Figure 46).

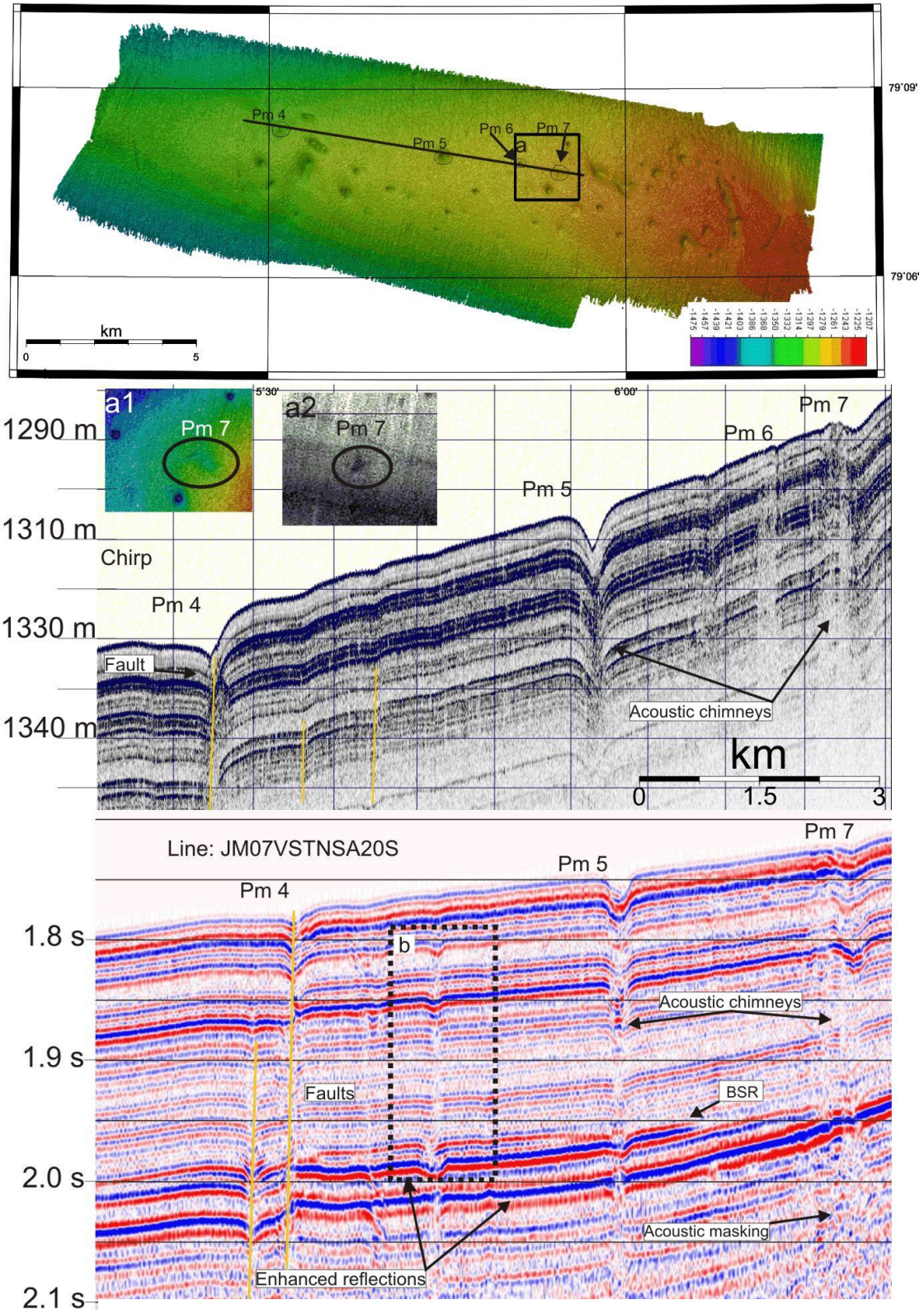

Figure 45: a) Swath bathymetry showing the location of seismic profile and pockmarks. a1) swath bathymetry showing pockmark 7. a2) same location as a1, showing the backscatter. b) Chirp profile showing the fine lamina of the uppermost meters of sediment. The chirp line crosses pm 4, 5, 6, and 7. c) Seismic line JM07VSTNSA20S crossing on the pm 4, 5, 6, and 7. The profile shows four pockmarks, where two of them are possibly fault related. c-b) Possibly pockmark in development.

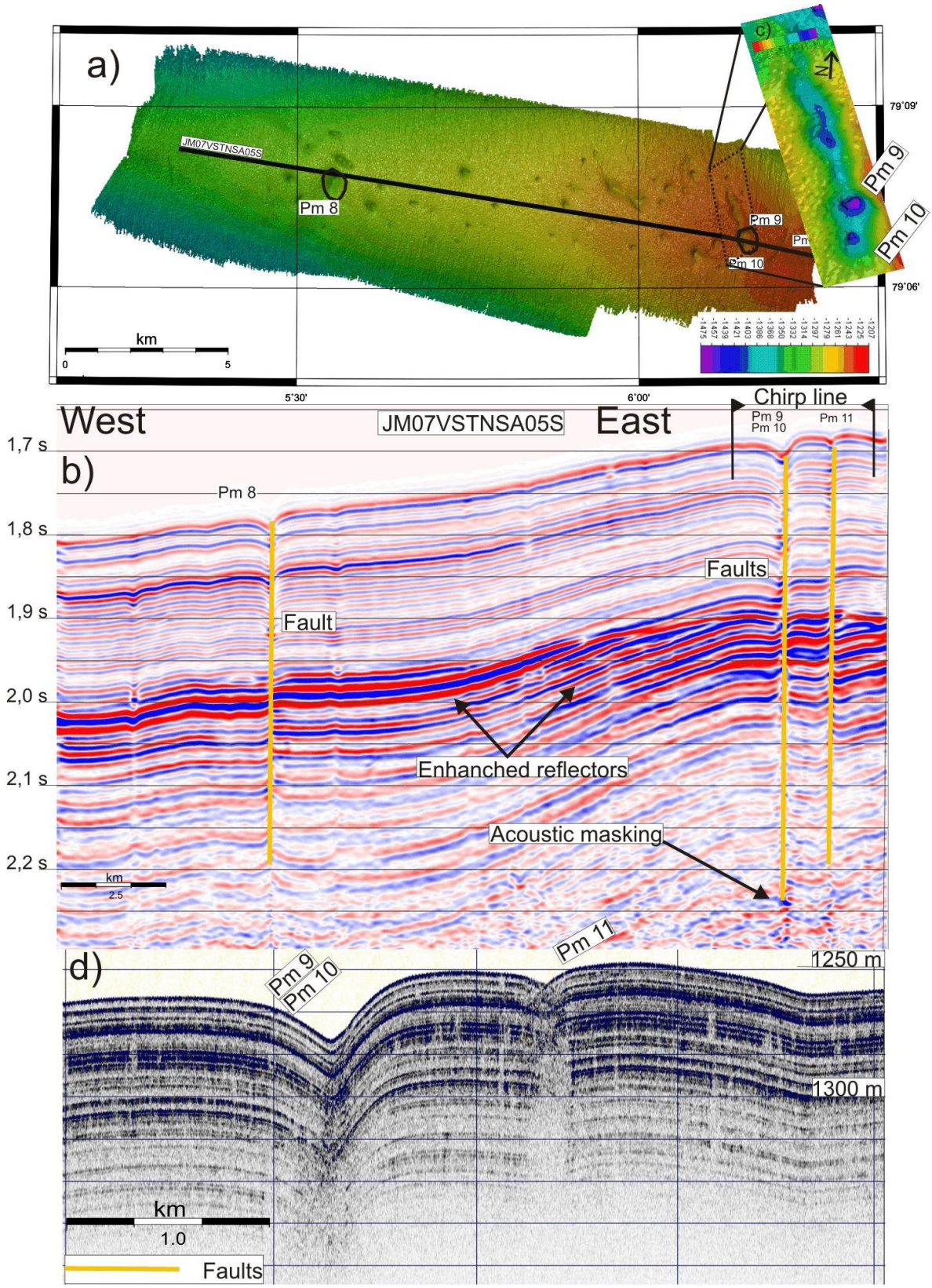

Figure 46:a) Swath bathymetry showing the location of seismic profile and pockmarks. b) Seismic line JM07VSTNSA05S crossing on the side of pm 8, on the rim between pm 9 and 10 and across pm 11. The profile shows four fault related pockmarks. c) Zoomed in on fault where pm 9 and pm 10 is marked, depth scale from -1230 to -1250 m. e) Chirp profile showing the fine lamina of the uppermost meters of sediment. The chirp line crosses the rim between pockmark 9 and 10, thereafter crossing pockmark 11.

Fluid pathways that are related to faults may penetrate deeper than acoustic chimneys. Fault related fluid pathways connect to deep rooted sources from well below the free gas zone beneath the BSR.

The acoustic chimneys are in many cases rooted in the acoustic turbidity zone interpreted to be a gas accumulation area. The gas may be a mixture of biogenic gas, and hydrothermal gas transported trough deep rooted faults of the young ocean crust. However, this suggestion is highly speculative since we cannot recognize the ocean crust formations on our available seismic lines.

4.4.3 CHIMNEYS AND POCKMARKS

Pockmark 7 (Figure 45a1) is hardly visible on the swath bathymetry, but can be clearly recognized due to its high backscatter (Figure 45a2). The chirp data may indicate a push-down effect in the upper seabed at pockmark 7, but also pull up effects are possibly in the most upper part possibly due to either authigenic carbonate or gas hydrate accumulations. There exists also a narrow vertical acoustic turbidity zone beneath pockmark 7 due to upward migration of fluids.

The seismic line crossing pockmark 7 indicates a possible pull-down effect at approx. or just beneath 1.8 s TWT. It is possibly caused by a velocity decrease of the seismic signal. Alternatively, a paleo-pockmark may show a similar seismic feature.

Pockmark 4 belongs to a fault dominated pockmark field (Figure 45), which is also suggested to for pockmark 8 (Figure 46). The seismic line provide some evidence for two faults, where the eastern most fault can be followed from the seafloor trough the BSR to the gas accumulation area beneath it.

The stippled black frame b in the seismic line (Figure 46) indicates not only the existence of a premature acoustic chimney but also possibly a buried pockmark at a depth of ~2.0s TWT. In comparison, pockmark 5 (Figure 45) shows an acoustic chimney that clearly reaches the seabed leading to a recognizable seabed fluid flow expression. This pockmark is easily spotted on all the seismic profiles and the swath bathymetry data. Both pull down and pull-up effects are visible at different levels at the high amplitude zone between 1.95 and 2.1 s TWT. It is difficult or nearly impossible to differentiate between pull-up effects caused by high ve-

locity anomalies or structural effects due to sediment deformation that is likely caused by vertical and rapid fluid migrations.

On Seismic line JM07VSTNSA05S (Figure 46) there are three areas with displacements between seismic reflectors that have been interpreted to be faults. The displacements vary between 20- 10 ms TWT. Above the inferred faults a string of pockmarks exists.

Pockmarks 9 and 10 (Figure 46c) belong to a string of pockmarks, which are interlinked at the seabed by a trough that is aligned approximately in north-south direction. The string of pockmarks including the trough is approximately 2500 m long and 400 m wide. The depressions are up to 15 m deep getting shallower towards the north.

Pockmark 8 (Figure 46) seems to be a single pockmark that has an elongated shape downhill. The seismic data (Figure 42b) suggest the fault due to displaced seismic reflectors, which is particularly obvious beneath 2 s TWT. Similar reflector displacments are documented below pockmark 4 (Figure 4) suggesting that the fault systems may play an important role in the development of fluid migration pathways at the Vestnesa Ridge.

4.4.4 DEPOSITIONAL SYSTEM OF VESTNESA RIDGE

The interpreted seismic horizons show a westward progradation and an apparent thinning of the bedding (Figure 40- 42).

Horizons marked in seismic line JM06_WSVAL 12 (Figure 40) show a dipping seabed towards the northwest with horizon 1 and 2 parallel to the seafloor. Horizon 3 and the horizons below are dipping gradually deeper with depth in the seismic section. The steep dipping may also be caused by velocity artifacts due gas within the sediments (Badley, 1985)

The same horizons are traced in seismic line JM06_WSVAL 13 (Figure 41) where horizon 3 shows a steeper gradient toward the northwest. Also, horizon 2 is dipping gradually deeper toward the west. Northwestward from seismic line 06JM_WSVAL 12 the amount of acoustic chimneys seems to increase.

Seismic line 06JM_WSVAL 14 (Figure 42) has a different direction that is more towards west. The seafloor reflector is dipping toward west on the seismic profile. Horizons 2 to 5 are dipping steep toward the centre of the profile where they are flattening. At the western part of

the seismic profile there possibly a basement high, which causes horizon 5 to dip upward and horizon 3 and 4 to merge together. At the center of the basement high there is an isolated area with pockmarks above several faults that penetrates horizon 5, which are separated by approximately 6 kilometers from the closest pockmark fields further east.

The oceanic basement seen on seismic line 06JM-WSVAL 14 (Figure 42) may possibly be the same basement high as seen on seismic line UB 18-81 (Figure 18), and the basement outcrop that pierce the Vestnesa Ridge (Figure 48).

Seismic line JM07VSTNSA51S (Figure 43) runs transverse to the Vestnesa Ridge. The sediment packages on the southern flank of the Vestnesa Ridge are pinching out, where they on the northern flank are thick sediments packages, indicating that ocean currents may have gradually eroded the southern flank of the Vestnesa Ridge, and redeposited sediments on the northern flank. Such a process may have caused the crest of Vestnesa Ridge to gradually migrate northward.

Between the north-western part of the Vestnesa Ridge and the upper continental slope several downslope-sediment transport features are clearly observable. For example, a major channel runs towards the deeper basin while gullies prevail on the upper slope. The gullies merge into the Kongsfjorden channel (Figure 47).

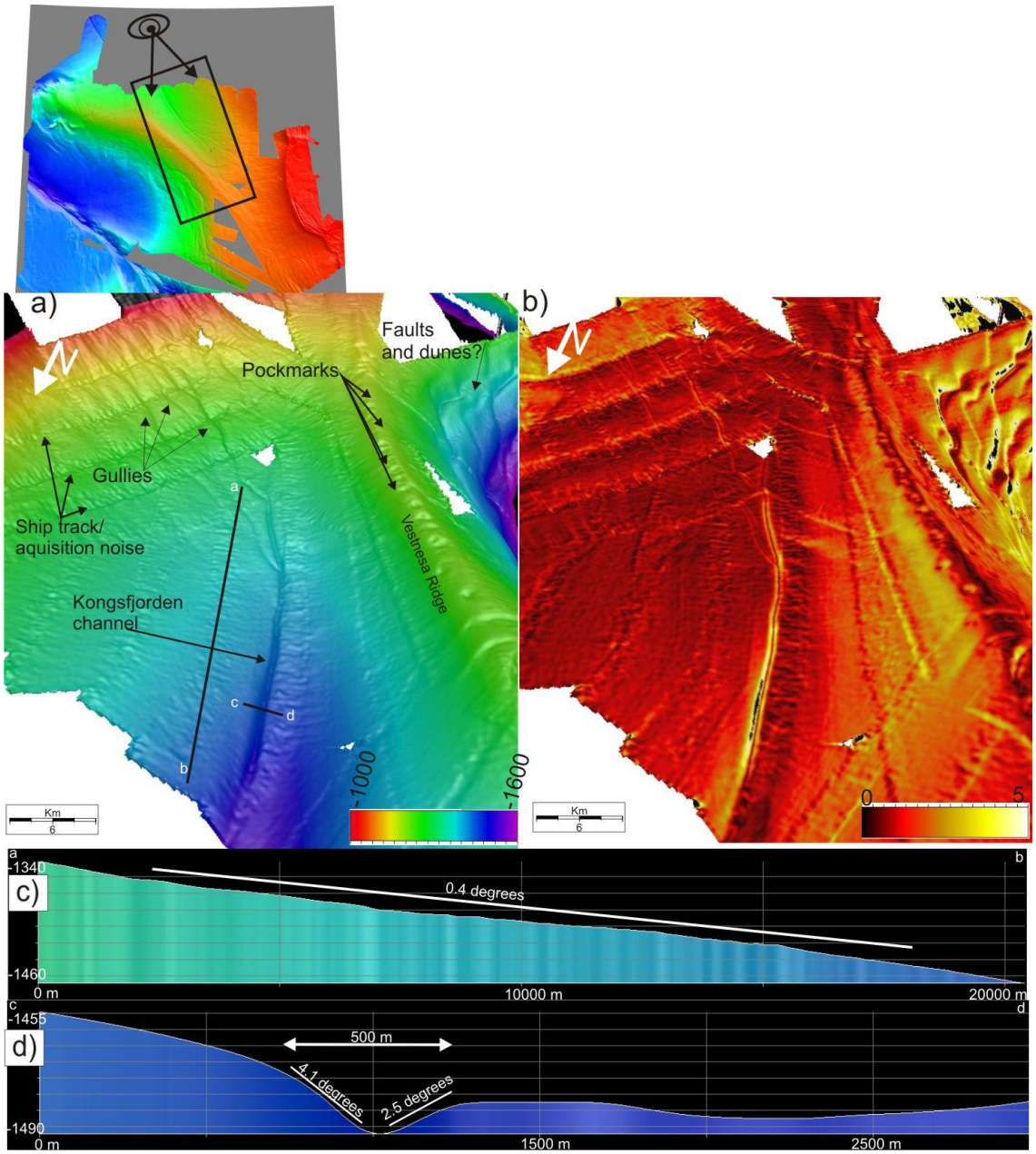

Figure 47: a) Swath bathymetry gridded to 50 m . It shows the Kongsfjorden channel, and gullies coming from the upper slope and Kongsfjorden trough mouth fan on the northern part of the Vestnesa Ridge, while dune formations are indicated on the southern side of the ridge. b) Slope gradient map encompassing values from 0-5 degrees. c) Profile showing the seafloor gradient (a-b solid black line in Figure a) parallel to the Kongsfjorden channel. d) Profile (c-d solid black line in Figure a) crossing the Kongsfjorden channel. White areas are data removed during processing due to acquisition noise.

The Kongsfjorden channel is 15 m deep (Figure 47d) with a gentle slope of 0.4°. It runs parallel to the northeastern part of the Vestnesa Ridge (Figure 47 a and d). The Kongsfjorden channel continues further towards the northwest.

The soutwestern part of the Vestnesa Ridge (Figure 48) is very different in that, it shows a very distinct and more than 5000 m long and more than 300 m high and 1500 m wide ridge. It is oriented in northeast-southwest and shows steep flanks. The southern flank has a gradient of 24° while the western and eastern slope have a slope of 21° and 36°, respectively. The ridge is interpreted to be a basement outcrop, due to its high slope gradient. Eiken and Hinz (1993) interpretation of seismic line UB 18-81 (Figure 18) shows a basement high on the western part of the line, where this basement outcrop may be a part of.

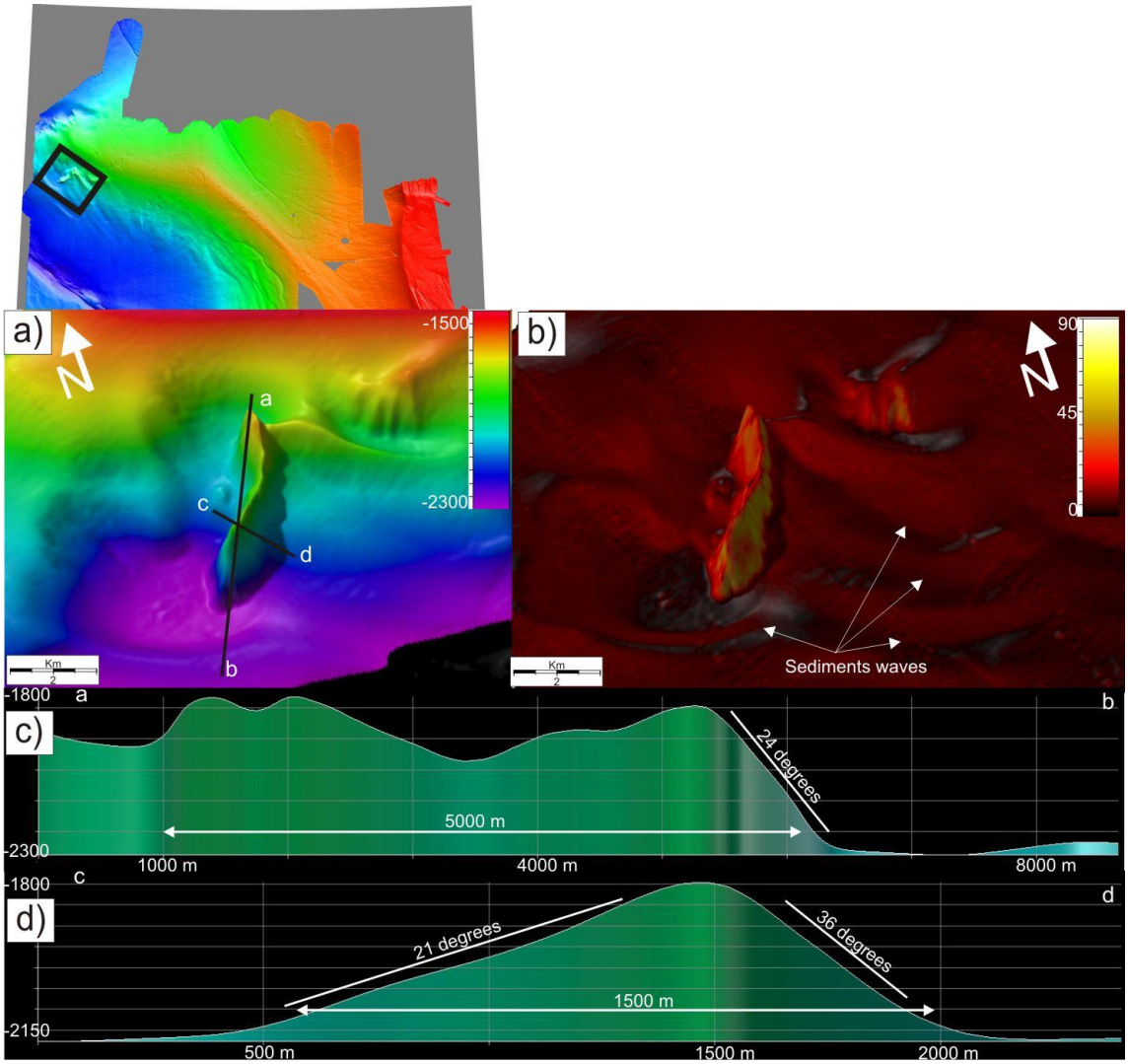

Figure 48: a) Swath bathymetry gridded to 50 m showing an area with a large ridge with steep slopes, and sediment waves in the vicinity b) Slope gradient map of the same area indicates the steep gradients of the ridge and highlights the sediment waves nearby. c) Profile (a-b) along the ridge. d) Profile (c-d) transverse to the ridge.

The ridge is surrounded by irregular dune like structures with a dominant east/west orientation showing an length of more than 5 Km and a width of more than 2 Km in some places. The slope of the inferred sediment waves varies between 2° to 5° degrees on the lower side, and is around 1° on the upper side. Due to the location in the area and their sizes they may be seen as secondary contourite deposits, which have been observed along many large sediment drifts (Carter and McCave, 1994).

The southern slope of the Vestnesa Ridge appears also to be more unstable than the northern area. There is evidence for several downslope-trending elongated depressions that may represent small scale slope failures. They start at approximately 1700 m.b.s.l. and appear to continue into the abyssal plain (Figure 49).

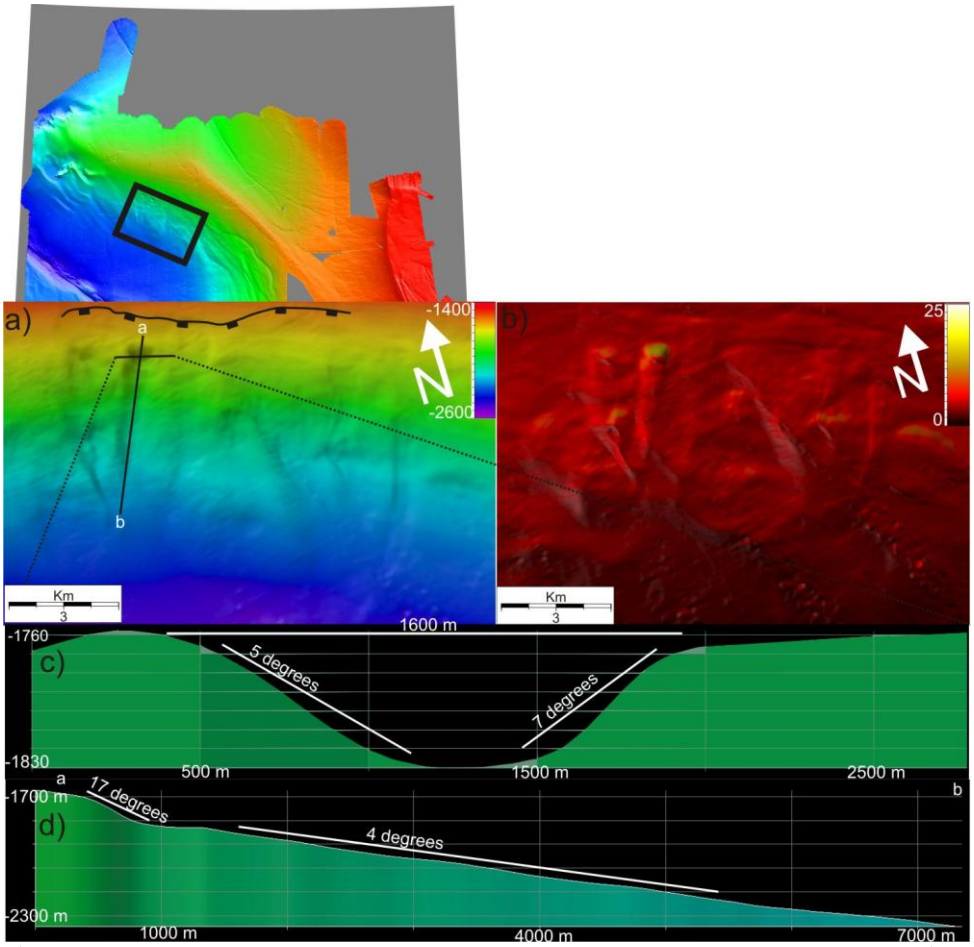

Figure 49: a) Swath bathymetry gridded to 50 m showing an area with several large slides. b) Slope map of the same area, note the steep gradient of the hang walls, compared to the side walls. c) Transverse profile of the largest slide observed in the study area. d) Profile along the visible part of the slide scar.

One of the most predominant elongated depressions (Figure 49) exhibits a 1600 m wide headwall, with a height of 70 m and a 17° slope. The sidewalls (Figure 48 c) have a mean gradient of 5° at the western and a gradient of 7° at the eastern side of the wall. The elongated depression has a mean slope angle of 4° and can be followed for approximately 7000 m before it merges with another elongated depression that developed further west.

Since several headwalls are situated at approximately the same depth below a fault (Figure 49) it is attempting to suggest that they are fault related.

5 DISCUSSION

5.1 SUBSURFACE FLUID FLOW

The Vestnesa Ridge off the NW Svalbard margin exhibits a variety of vertical zones of acoustic turbidity or disrupted reflections that can be classified as acoustic chimney systems similar to acoustic pipes observed on the mid-Norwegian margin (e.g. Berndt et al., 2003) or elsewhere on continental margins worldwide (Judd and Hovland, 2007). Some of the NW Svalbard acoustic chimneys at Vestnesa occur so close to each other that it is difficult to identify them as individual features, and they may be interconnected (Bünz et al., 2008). High resolution swath bathymetry and seismic data demonstrate that acoustic chimneys concentrate mainly at the apex of the sediment drift constituting the Vestnesa Ridge crest. Most of the observed chimneys pierce through sedimentary strata and connect at the seabed to pockmarks (Figure 40- 42)

There is some evidence that acoustic chimneys are getting wider with an increase in depth beneath the seabed (Figure 42). The increase in depth is accompanied by an increase in temperature due to the high geothermal gradient above the young ocean crust. The gradient is suggested to be between 65 and 118 ^{o}C/km based on in situ temperature measurements (Crane et al., 1982) and from BSRs inferred geothermal gradients (Vanneste et al., 2005). Thus, the high temperature gradients above young ocean crust may cause a warmer and more buoyant methane gas at depth causing a more vigorous perturbation of vertical fluid migration zones. This may also explain why some of the observed chimney structures are wider at greater depth as observed and discussed in other regions (Wood et al., 2002). Since there is presently no bore-hole information to verify these assumptions concerning temperature and gas buoyancy, the explanation has a limited validation. However, the hypothesis is consistent with observed acoustic chimneys (Figure 40- 42) and estimated geothermal gradients in the study area (Vanneste et al., 2005).

Within the chimneys, high amplitude reflections in the upper 50 ms TWT occur, i.e. approximately 40-50 m below the sea floor depending on the speed of sound in sediments (Figure 40, 42 and 45). These high amplitude reflections - if accompanied by a pull-up reflection - are possibly caused by the presence of gas hydrates and/or authigenic carbonates within the

chimney (Figure 40 and 45). However, since the precipitation of carbonates is restricted to the sulphate reducing zone, carbonates must have been buried beneath sediments after their formation close to the seafloor in order to occur at greater depth (Petersen et al., 2008). Alternatively, there can be a significant disruption of sedimentary strata due to rapid fluid flow or blow out events that also will cause pull up of reflections at the chimney walls (e.g. Figure 41).

In contrast, internal reflectors showing a significant push-down effect (Figure 42a_c) may indicate a seismic velocity decrease due to free gas in the pore space of sediments (Badley, 1985). Therefore, the observed information of pull up and push down acoustic effects in chimneys may shed more light on the individual plumbing systems in the Vestnesa Ridge. However, sampling of sediments and fluids from acoustic chimneys for geochemical analysis is requested and necessary for a more solid interpretation of the presented geophysical evidence for seabed fluid flow and plumbing systems.

The seismic lines indicate a heterogeneous distribution of gas hydrate above the BGHSZ and of free gas beneath the BGHSZ (Petersen et al., 2008). Locations of anomalous amplitudes seem to be controlled by the distribution of fractures and faults that created a favourable pathway for focused fluid flow upward. In these areas of elevated heat fluxes, methane gas may exist inside the hydrate stability zone (Wood et al., 2002).

5.2 ROLE OF GAS HYDRATE IN SUBSURFACE FLUID FLOW

According to Nimblett and Ruppel, (2003) gas hydrates may reduce the permeability of sediments, and therefore influence the fluid- flow flux through the sediment formation. The reduced permeability can therefore act as a “cap rock” where free gas accumulates beneath the gas hydrates cemented sediments.

Below the BGHSZ defined by a BSR (Figure 40-43), a zone of enhanced reflections shows a thickness of approximately 150 m (Bünz et al., 2008). This zone should correspond to the underlying free gas. The presence of such a thick free gas zone suggests that the gas is produced well beneath the base of the hydrate stability zone (Paull et al., 1996), which is also supported by the large extent of acoustic turbidity zones beneath the high amplitude reflec-

tion zones (Figure 40-43). Seismic data indicate that there exists fluid and/or mainly gas accumulation in the entire Vestnesa Ridge, but both surface and subsurface fluid flow features are confined to the crest of the ridge (Figure 30 and 32). Bünz et al (2008) suggest that due to reduced permeability caused by gas hydrate growth in the pore space of sediments in the flanks (Figure 43), gas generated inside the Vestnesa Ridge may mainly migrate laterally below the BSR, i.e. the GHSZ. It appears to migrate upward towards the crest of the ridge, where it gets trapped under hydrate bearing sediments.

As the gas accumulates the pressure builds up, but the pressure will eventually be decreased due to the release of fluids trough chimneys or faults. Thus, the observed chimneys seem to act as major pressure valve for the Vestnesa Ridge. Since the Vestnesa Ridge is situated on young oceanic crust, both the fluid flow and the gas hydrate system may therefore be affected by hydrothermal circulation of the ocean crust (Bünz et al., 2008). As a result, the gas hydrate dissociation may become vigorous in areas of warm upward moving fluids. This may be observed if a BSR intersects with a fault and/or acoustic chimney, where warm fluids may up-rise. Here, the BSR is often absent, weaker or pointing upward if compared to the adjacent BSR (Vanneste et al., 2005).

Acoustic chimneys and faults including their seismic signature suggest that they act as active important fluid flow pathways. They connect the seafloor with the free gas zone beneath the GHSZ, and possibly with the acoustic turbidity zone that acts as a major gas supply zone. Since acoustic chimneys penetrate the GHSZ they also may act as a plumbing system for the entire Vestnesa Ridge (Bünz et al., 2008)

5.3 MORPHOLOGY OF THE POCKMARKS

According to Hovland et al (2002) most pockmarks are circular depressions, since gas escape and erosion from a point source usually produces circular depressions. However, a large variety of morphologies exists depending on fluid flow rates, bottom current interactions, type of sediments, and blow out events. Bøe et al. (1998) explained the sizes of large pockmarks found in Skagerrak as a continuous release of gas from fixed points over some thousands of years. During slow gas escape through clay-rich sediments the finest fraction can become suspended in the water column ('gas-winnowing') and subsequently removed by bottom currents resulting in a slow erosion of the seabed.

Elongated pockmarks may initially be circular, so when measuring the shortest axis a minimum estimate of the initial pockmark diameter may be given. Elongated pockmarks may also be generated by merging of circular pockmarks formed due to gas escape from faults or merging of individual pockmarks (Judd and Hovland 2007). Elongated pockmarks occur also in areas influenced by strong bottom currents capable of eroding the newly formed pockmarks (Hovland et al 2002). Even though the pockmarks at Vestnesa are large (Figure 33a), all of the measured pockmarks on Vestnesa Ridge are within the range of pockmarks classified by Hovland et al (2002).

Since many of the pockmarks in the Vestnesa study are elongated, and some indicate a brim in the centre of the elongated pockmarks, a connection between some circular pockmarks is possibly responsible for the development of more elongated pockmarks. There is also evidence for a relation of pockmarks to underlying faults on the high resolution seismic lines, indicating faults as one of the causes for the elongation of the longest pockmark strings found at the Vestnesa Ridge (Figure 46).

In the North Sea, Bøe et al. (1998) described large elongated depressions to be current modified pockmarks with long axis that run parallel to the present bottom currents. They concluded therefore, that in areas of strong bottom currents pockmark fields can resemble a similar orientation. Since the pockmarks of the Vestnesa Ridge seem to have a random orientation (Figure 39), it is less likely and not obvious that strong bottom currents influence the pockmark field in such a manner. However, it is obvious that bottom currents must exist at Vestnesa because of the development of the distinct sediment drift (Figure 48). On the other hand, it is less likely that very strong bottom currents exist at the crest of the Vestnesa Ridge that are capable of eroding or shaping the pockmarks. According to Josenhans et al. (1978) erosion by bottom current will be most significant on the downstream side of the pockmark, resulting in an asymmetrical shape where they develop deepest upstream. Some of the elongated pockmarks on Vestnesa Ridge do have a asymmetrical shape, but since the orientation of the asymmetrical shape has a random orientation (Figure 39) other processes such as fault position, creeping, or similar down-slope processes may influence their morphology.

Pockmarks on Vestnesa Ridge are characterized by both high and low seafloor reflection amplitudes relative to the surrounding seafloor (Figure 33d). High amplitudes may be indicative for precipitated carbonate and/or hydrate formation at or near the seafloor whereas low reflectivity reflects soft, muddy sediment probably being altered by fluid expulsion (Petersen et al., 2008). Figure 33d shows an integration of swath bathymetry (Figure 33a), slope gradient (Figure 33b) and backscatter maps (Figure 33c). The three figures show the same feature but with different acoustic seabed expressions. It makes it possible to image details within pockmarks that remain otherwise unrecognized on an individual map. It warrants more acoustic and ground truth investigations that go beyond the ambitions of this master thesis.

During gas releases over 10-100 Kyr, coarse sediments and shell fragments can be concentrated within the pockmarks due to gas winnowing (Bøe et al., 1998), and authigenic carbonate may also form in the pockmarks (Hovland et al., 2002). Such processes may lead to a carbonate pavement in the pockmark floor (Andresen et al., 2008), which may explain high backscatter on the swath bathymetry data (Figure 33c), and the high amplitude response that is observed by Petersen et al. (2008) and on seismic lines (Figure 46). Petersen et al. (2008) suggested that the high amplitudes on the seismic may be caused by gas hydrate close to, or on the seafloor, which also may also explain the high backscatter in some of the pockmarks.

One area with high backscatter does not correlate with any visible pockmark either on the swath bathymetry map or the slope gradient map (Figure 33d). This may be explained by soft sediments on the crest of Vestnesa Ridge (Vogt et al., 1994), where beam signals from the EM 300 may penetrate the uppermost part of the seafloor. High backscatter that is not related to pockmarks may therefore relate to buried targets that have a strong reflection (Figure 22c). Such targets may be authigenic carbonate crusts or gas hydrates.

5.4 CONTROL MECHANISM ON FLUID FLOW IN THE VESTNESA RIDGE

The Vestnesa Ridge is known to overly young oceanic crust where the eastern part is approximately 20 My and the western part is less than 10 My until it reaches the zero- age at the centre of the mid ocean ridge. The western end of the Vestnesa Ridge is about 40 km away from the Molloy Ridge, thus probably close to an area of frequent and shallow seismic activity. Shallow crustal seismicity in connection with the mid ocean spreading is very likely and may sugges that active faults occur in the region around Vestnesa Ridge.

Seismic and swath bathymetry data indicate several zones of seabed deformation, including faulting, fluid expulsion, deformed and disturbed bedding. There are several faults that rupture and deform the uppermost sediments and penetrate the seafloor. This observation suggests that they are still active and the structural controlled expulsion of fluids may explain the chains of pockmark, or clusters with pockmarks adjacent to the faults (Figure 46). There are also apparently active faults identified by Vanneste et al. (2005) with oblique angle (striking 300°) that are parallel the Molloy Transform Fault. Since Vestnesa Ridge is situated on top of oceanic lithosphere within an age window of 10 to 20 My, there is a possibility of deep rooted faulting. This may be attributed to rapid subsidence of a young ocean ridge due to the vigorous convective hydrothermal circulation that causes the crust to cool. The young crust even pierces through the sediment blanket as seen in Figure 48.

This basement outcrop located at the western part of the Vestnesa Ridge is believed to be a part of a basement high, identified by Eiken and Hinz (1993) in seismic line UB 18-81 (Figure 18). The sediments of Vestnesa Ridge that accumulated on the young oceanic lithosphere are believed to reach a thickness of 2000 m (Breivik et al., 1999) and may additionally control the hydrothermal circulation from the crust to the seabed.

Sediments on the Vestnesa Ridge have been described as a contourite deposit (e.g. Vogt et al., 1994). Ocean currents can deposit coarse to fine grained sediments and erode sediments depending on the strength and the duration of the current regime (Viana et al., 2007). Sediments offshore NW Svalbard have been accumulated driven by the waxing and waning of the ice streams and ice sheets. Vorren et al. (1989) showed that during times when the gla-

ciers reach the shelf edge a high sedimentation rate prevail due to glacigenic sediment input in form of debris flows.

If the sedimentation rates are high enough, the speed of burial exceeds the rate of compaction. Thus, if the drainage of pore fluids is hindered by low permeability, the pore fluid are captured, which in turn may lead to over-pressurized sediment layers. Fluids may escape laterally along more permeable layers. However, if the pressure cannot be reduced, the overpressure within the sediment layers can result in vertical fluid and sediment flow (Judd and Hovland, 2007). When the gas migrates to an area with less pressure the gas can start to expand and this may increase the pressure within the sediment beds further. This process may become self perpetuating and become the main driving force for gas migration (Judd and Hovland, 2007), which is possibly one of the control mechanisms on fluid flow in the Vestnesa pockmark fields.

5.5 ORIGIN OF FLUIDS/GAS

High carbon contents measured in Miocene deposits of the Fram Strait suggest the potential for hydrocarbon source rocks along the continental margin of NW Svalbard (Knies and Mann, 2002). Knies et al (2004) found also traces of both biogenic and thermogenic methane gas in sediments of the Kongsfjorden shelf.

Observations of gas seepage of thermogenic gas from the seabed to the water column is particularly evident at major tectonic lineaments west off Spitsbergen. Active petroleum source rocks along the western Spitsbergen continental margin and migrating gaseous hydrocarbons at re-activated fault systems might explain these findings at the Kongsfjorden shelf (Knies et al., 2004). Unfortunately, we still have to await the results from gas analysis of samples from the Vestnesa Ridge. Thus, at the present we only can speculate on the origin of these gases.

It is known that the geothermal gradient on Vestnesa Ridge increases gradually from 70 to 115 °C/km towards the Molloy transform fault (Vanneste et al., 2005). By assuming a constant geothermal gradient, the western part of Vestnesa Ridge may represent at 2 km depth beneath the seabed a temperature of 230 °C. Accordingly, a temperature of 350 °C may be reached at 5 km depth at the base of the sediments overlaying the eastern part of the ocea-

nic crust (Figure 49) (Knies et al., 2004).

Biogenic gas according to Rice (1992) has a optimum temperature range of 35-45 °C, which will certainly be reached at the western part of the Vestnesa Ridge at a depth between 300 and 390 m.b.s.f.

Thermogenic gas occurs mainly in a temperature window from 60 to 260 °C. Considering the Vestnesa Ridge geological and thermal setting, the generation of thermogenic gas may develop at depths between 520-2250 m.b.s.f at the western part and at depths of 857-3714 m.b.s.f at the eastern part depending on the geothermal gradients (Figure 49). Therefore, a mixture of sources from thermogenic and biogenic gases is likely to be encountered in the seabed fluid flow system of the Vestnesa Ridge.

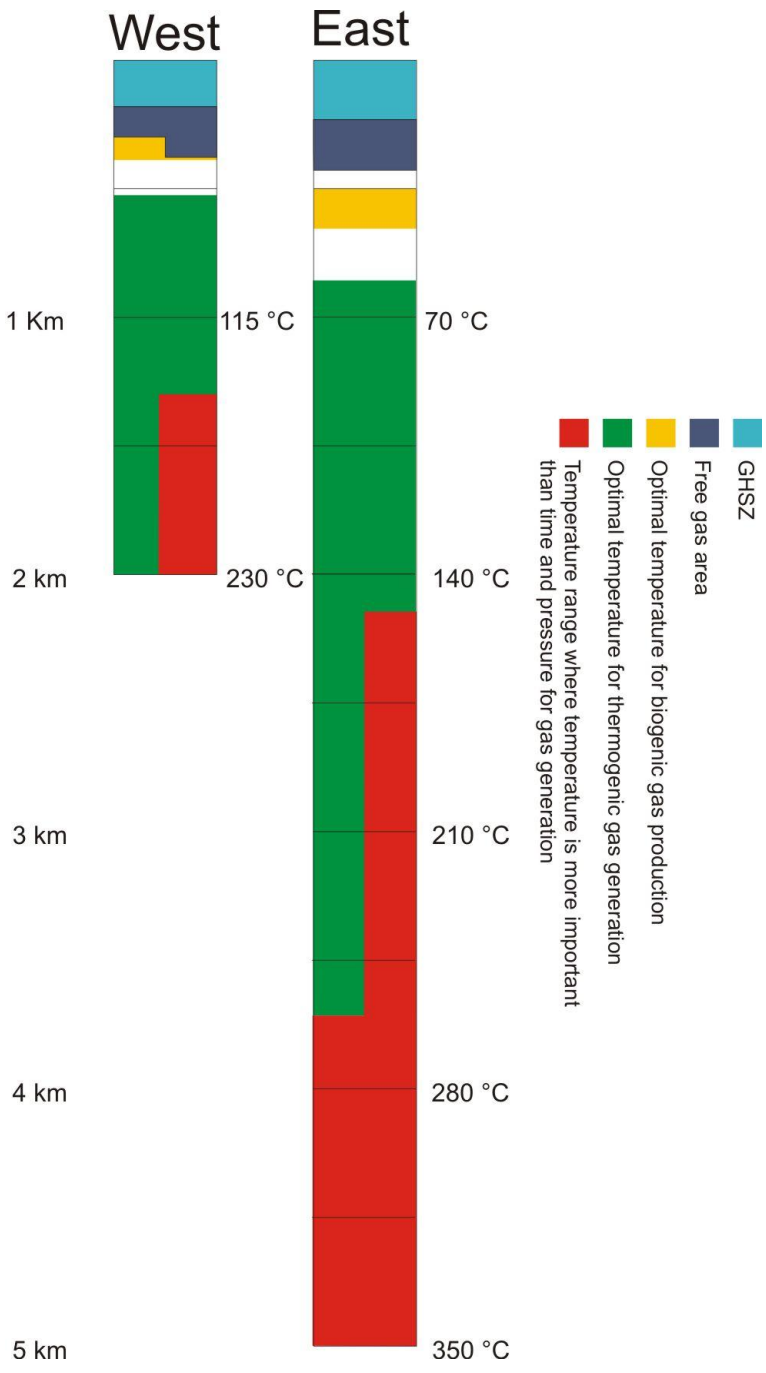

Figure 49: The depth and temperature plot shows the optimal areas for the generation of biogenic and/or thermogenic gas as well as the GHSZ and the free gas zone beneath it

Generally, the generation of thermogenic hydrocarbons is a slow process during which source rocks mature as sedimentary basins subside and receive sediment infill. This process takes millions of years. In places where there are exceptional high heat flows, such as at active spreading ridges or close to it, this process may be accelerated. Such a situation may exist at the Vestnesa Ridge but also at other locations in the world. For example, Simoneit

and Lonsdale (1982) described petroleum generation in the Guaymas Basin, which is a ≈500 m thick sediment basin situated on top of a spreading ridge west of California, where sediments have accumulated for about 150 ka. Due to very high temperatures - if compared to normal petroleum genesis windows - the chemical decomposition of organic materials is highly accelerated, which in turn may produce hydrothermal petroleum in a time span of less than 5 ka (Didyk and Simoneit, 1989).

Another possibility that is interesting to consider has been presented by Catallo and Junk (2001). They patented a method for transforming biomass to hydrocarbon mixtures in near-critical or supercritical water in anoxic or reducing environment, which transform biological masses into hydrocarbons within hours. Major differences between the near critical and supercritical treatments were that supercritical conditions produced higher yields of both gaseous hydrocarbons and insoluble carbonized residue.

Supercritical water forms at temperature/pressure conditions above 405 °C and 300 bar for seawater (Tester, J. et al., 1993). Supercritical water is neither vapor nor liquid, but something in between (Hovland et al., 2005). It has properties that include a very high compressibility, it is highly corrosive, and has a very low viscosity, and it behaves as a non-polar rather than a polar fluid (Hovland et al., 2006). The density of water also changes rapidly with respect to both temperature and pressure, and at the critical point it attains a value of 0.3 g/cm^3 (Tester, J. et al., 1993), which makes supercritical water extremely buoyant. However, according to the geothermal gradient measured (Crane et al., 1982) and estimated (Vanneste et al.,2005) at the Vestnesa Ridge, the temperature seems not to be high enough to produce supercritical water.

6 CONCLUSION

- Pockmarks along the crest of the Vestnesa Ridge indicate active fluid flow seeping.
- No obvious correlation exists between the backscatter, the size and the depth of the seabed fluid flow expressions.
- The orientation of elongated pockmarks is controlled by processes such as fault development, creeping of sediments, or similar down-slope processes.
- Due to reduced permeability in the GHSZ, the gas apparently migrates below the GHSZ along the flanks of Vestnesa Ridge laterally upward to the crest, where the pressure builds up as it get trapped below the GHSZ.
- Acoustic chimneys connected to seabed pockmarks and pierce through the GHSZ. They may originate in the free gas zone directly beneath the BSR or much deeper in the acoustic turbidity zone.
- Individual chimneys provide hints for an active plumbing system where pull up reflectors suggest gas hydrate formation in chimneys or the existence of buried crusts of authigenic carbonate.
- High geothermal gradients due to the young ocean crust may force vigorous fluid flow in the Vestnesa Ridge as exemplified by the changes in the width of the acoustic chimneys.
- The suggested source regions of fluid flow encompass both a deeper window for thermogenic and a shallow temperature window for biogenic gas.
- Sediment transport processes at the northern and southern part of the Vestnesa Ridge vary greatly with slope failures and sediment waves on the south and more stable flanks on the northern area. The northern area is influences by the adjacent deep-sea channel and the gullies system of the Kongsfjorden trough mouth fan that was possibly highly active during the last ice age.

REFERENCES

Andreassen, K., Hart, P.E. and Grantz, A., 1995. Seismic studies of a bottom simulating reflection related to gas hydrate beneath the continental margin of the Beufort Sea. Journal of geophysical research, 100(NO.B7): 12659-12673.

Andreassen, K., Laberg, J.S. and Vorren, T.O., 2008. Seafloor geomorphology of the SW Barents Sea and its glaci-dynamic implications. Geomorphology, 97(1-2): 157-177.

Andresen, K.J., Huuse, M. and Clausen, O.R., 2008. Morphology and distribution of Oligocene and Miocene pockmarks in the Danish North Sea implications for bottom current activity and fluid migration. Basin Research, 20: 445-466.

Badley, M.E., 1985. Practical seismic interpretation. IHRDC Press,Boston, MA, United States, Pages: 265 pp.

Berndt, C., Bunz, S. and Mienert, J., 2003. Polygonal fault systems on the mid-Norwegian margin: a long-term source for fluid flow. Geological Society, London, Special Publications, 216(1): 283-290.

Bjørlykke, K., 2001. Sedimentologi og petroleumsgeologi. Gyldendal Norsk Forlag AS, 334 pp.

Blondel, P. and Murton, B.J., 1997. Handbook of seafloor sonar imagery. Wiley, Chichester, XXII, 314 s. pp.

Boetius, A. et al., 2000. A marine microbial consortium apparently mediating anaerobic oxidation of methane. Nature, 407(6804): 623-626.

Breivik, A.J., Verhoef, J. and Faleide, J.I., 1999. Effect of thermal contrasts on gravity modeling at passive margins: Results from the western Barents Sea. Journal of geophysical research: planets, 104(7): 15293.

Brooks, J.M., Kennicutt, M.C., Fay, R.R., McDonald, T.J. and Sassen, R., 1984. Thermogenic Gas Hydrates in the Gulf of Mexico. Science, 225(4660): 409--411.

Brown, A.R., 1999. Interpretation of three-dimensi3onal seismic data. AAPG Memoir, Tulsa, Oklahoma, 42.

Bryn, P., Berg, K., Stoker, M.S., Haflidason, H. and Solheim, A., 2005. Contourites and their relevance for mass wasting along the Mid-Norwegian Margin. Marine and Petroleum Geology, 22(1-2): 85-96.

Bünz, S. and Mienert, J., 2004. Acoustic imaging of gas hydrate and free gas at the Storegga Slide. Journal of geophysical research, 109(B04102).

Bünz, S., Petersen, J., Hustoft, S. and Jürgen., M., 2008. Environmentally-sensitive gas hydrates on the W-Svalbard margin at the gateway to the arctic ocean, Proceedings of the 6th international conference on gas hydrates (ICGH 2008) Vancouver, British Columbia, Canada.

Bøe, R., Rise, L. and Ottesen, D., 1998. Elongate depressions on the southern slope of the Norwegian Trench (Skagerrak): morphology and evolution. Marine Geology, 146(1-4): 191-203.

Carter, L. and McCave, I.N., 1994. Development of sediment drifts approaching an active plate margin under the SW Pacific Deep Western Boundary Current. Paleoceanography, 9(6): 1061-1085.

Catallo, J.W. and Junk, T., 2001. Transforming biomass to hydrocarbon mixtures in near-critical or supercritical water, USA.

Chand, S. and Minshull, T.A., 2003. Seismic constraints on the effects of gas hydrate on sediment physical properties and fluid flow: a review. Geofluids, 3: 275-289.

Clarke, J.E.H., Gardner, J.V., Torresan, M. and Mayer, L., 1998. The limits of spatial resolution achievable using a 30kHz multibeam sonar: model predictions and field results.

Crane, K. et al., 2001. The role of the Spitsbergen shear zone in determining morphology, segmentation and evolution of the Knipovich Ridge. Marine Geophysical Researches, 22: 153-205.

Crane, K., Eldholm, O., Myhre, A.M. and Sundvor, E., 1982. Thermal implications for the evolution of the Spitsbergen transform fault. Tectonophysics, 89(1-3): 1-32.

Didyk, B.M. and Simoneit, B.R.D., 1989. Hydrothermal oil of Guaymas Basin and implications for petroleum formation mechanism. Nature, 342: 65-69.

Dillon, W.P. and Paull, C.K., 1983. Marine gas hydrates, II Geophysical evidence, Cox, J. L. (ed Natural Gas Hydrates: properties, occurrence and Recovery), pp. 73--90.

Dimitrov, L.I., 2002. Mud volcanoes--the most important pathway for degassing deeply buried sediments. Earth-Science Reviews, 59(1-4): 49-76.

Eiken, O. and Hinz, K., 1993. Contourites in the Fram Strait. Sedimentary Geology, 82: 15-32.

Faleide, J.I., Solheim, A., Fiedler, A., Hjelstuen, B.O. and Vanneste, K., 1996. Late Cenozoic evolution of the western Barents Sea-Svalbard continental margin. Global and Planetary Change, 12: 53-74.

Faugeres, J., Mezerais, M. and Stow, D., 1993. Contourite Drift Types And Their Distribution In The North Atlantic and South-Atlantic Ocean Basins. Sedimentary Geology, 82: 189-203.

Fledermaus, 2007. Fledermaus. Reference manual Interactive Visualization Systems

Floodgate, G.D. and Judd, A.G., 1992. The origins of shallow gas. Continental shelf research, 12: 1145--1156.

Gay, A. et al., 2006. Seafloor facies related to upward methane flux within a Giant Pockmark of the Lower Congo Basin. Marine Geology, 226: 81--95.

Heggland, R., 1998. Gas seepage as an indicator of deeper prospective reservoirs. A study based on exploration 3D seismic data. Marine and Petroleum Geology, 15: 1--9.

Hovland, M., 2002. On the self-sealing nature of marine seeps. Continental Shelf Research, 22: 2387-2394.

Hovland, M., 2005. Gas hydrates. Petroleum Geology, Gas Hydrates: 261--268.

Hovland, M., Gardner, J.V. and Judd, A.G., 2002. The significance of pockmarks to understanding fluid flow processes and geohazards. Geofluids, 2(2): 127-136.

Hovland, M. and Judd, A.G., 1988. Seabed Pockmarks and Seepages. Graham and Trotman., London, 293 pp.

Hovland, M. et al., 2005. Was the Chapopote asphalt-volcano, Gulf of Mexico, generated by supercritical water? EOS, Transactions American Geophysical Union, 86(42): 397-402.

Hovland, M. and Svensen, H., 2006. Submarine pingos: Indicators of shallow gas hydrates in a pockmark at Nyegga, Norwegian Sea. Marine Geology, 228(1-4): 15-23.

Hovland, M. et al., 2006. Sub-surface precipitation of salts in supercritical seawater. Basin Research, 18(2): 221-230.

Howe, J.A., Shimmield, T.M. and Harland, R., 2008. Late Quaternary contourites and glaciomarine sedimentation in the Fram Strait. Sedimentology, 55: 179-200.

Hustoft, S., Bünz, S., Mienert, J. and Chand, C., 2008. The Vestnesa Ridge gas hydrate-reservoir and methane venting province at the Fram Strait in the Arctic - NW-Svalbard margin. University of Tromsø

Johnson, J.E., C., G. and E., S., 2003. Geophysical constraints on the surface distribution of authigenic carbonates across the Hydrate Ridge region, Cascadia margin. Marine Geology, 202: 79-120(42).

Josenhans, H.W., King, L.H. and Fader, G.B.J., 1978. A sidescan sonar mosaic of pockmarks on the Scotian Shelf. Canadian Journal of Earth Sciences, 15: 831-840.

Judd, A.G., 2003. The global importance and context of methane escape from the seabed. Geo-Mar Lett, 23: 147--154.

Judd, A.G. and Hovland, M., 2007. Seabed fluid flow, The impact on geology, biology and the marine environment. Cambridge University press, 475 pp.

Judd, A.G., Hovland, M., Dimitrov, L.I., Garcia Gil, S. and Jukes, V., 2002. The geological methane budget at Continental Margins and its influence on climate change. Geofluids, 2(2): 109-126.

Kastner, M., Keene, J.B. and Gieskes, J.M., 1977. Digenesis of siliceous oozes-I. Chemical controls on the rate of opal-A to opal-CT transformation an experimental study. Geochimica et Cosmochimica Acta, 41: 1041–1059.

Kennett, J.P., Cannariato, K.G., Hendy, I.L. and Behl, R.J., 2003. Methane Hydrates in Quaternary Climate Change. American Geophysical Union, Washington, DC,.

Khokhar, A.A., Gudmundsson, J.S. and Sloan, E.D., 1998. Gas storage in structure H hydrates. Fluid Phase Equilibria, 150--151: 383--392.

Knies, J., Damm, E., Gutt, J., Mann, U. and Pinturier, L., 2004. Near-surface hydrocarbon anomalies in shelf sediments off Spitsbergen: Evidences for past seepages. Geochem. Geophys. Geosyst., 5.

Knies, J. and Mann, U., 2002. Depositional environment and source rock potential of Miocene strata from the central Fram Strait: introduction of a new computing tool for simulating organic facies variations. Marine and Petroleum Geology, 19(7): 811-828.

Kopf, A. and Deyhle, A., 2002. Back to the roots: boron geochemistry of mud volcanoes and its implications for mobilization depth and global B cycling. Chemical Geology, 192(3-4): 195-210.

Kvalstad, T.J., Nadim, F., Kaynia, A.M., Mokkelbost, K.H. and Bryn, P., 2005. Soil conditions and slope stability in the Ormen Lange area. Marine and Petroleum Geology, 22(1-2): 299-310.

Kvenvolden, K.A., 1988. Methane hydrates and global climate. Global Biogeochemical cycles, 2: 221--229.

Kvenvolden, K.A., 1993. Gas Hydrates-Geological perspective and global change. Reviews of Geophysics, 31: 173--187.

Kvenvolden, K.A., 1995. A review of the geochemistry of methane in natural gas hydrate. Org. Geochem, 23: 997--1008.

Kvenvolden, K.A., 1998. A primer on the geological occurrence of gas hydrate. Geological Society, London, Special Publications, 137(1): 9-30.

Kvenvolden, K.A., 2000. Gas Hydrate and Humans. Ann NY Acad Sci, 912(1): 17-22.

Kvenvolden, K.A. and Rogers, B.W., 2005. Gaia's breath---global methane exhalations. Marine and Petroleum Geology, 22: 579--590.

Laberg, J.S., Dahlgren, T., Vorren, T.O., Haflidason, H. and Bryn, P., 2001. Seismic analyses of Cenozoic contourite drift development in the Northern Norwegian Sea. Marine Geophysical Researches, 22(6): 401-416.

Laberg, J.S. et al., 2005. Cenozoic alongslope processes and sedimentation on the NW European Atlantic margin. Marine and Petroleum Geology, 22: 1069--1088.

Leynaud, D., Mienert, J. and Vanneste, M., 2008. Submarine mass movements on glaciated and non-glaciated European continental margins: A review of triggering mechanisms and preconditions to failure. Marine and Petroleum Geology, In Press, Corrected Proof.

Ligtenberg, J.H., 2003. Unraveling the petroleum system by enhancing fluid migration paths in seismic data using a neural network based pattern recognition technique. Geofluids, 3(4): 255-261.

Lindberg, B., Berndt, C. and Mienert, J., 2007. The Fugloy Reef at 70 degrees N; acoustic signature, geologic, geomorphologic and oceanographic setting. International Journal of Earth Sciences, 96: 201-213.

Linke, P. et al., 1994. In situ measurement of fluid flow from cold seeps at active continental margins. Deep Sea Research Part I: Oceanographic Research Papers, 41(4): 721-739.

Lundin, E. and Dore, A.G., 2002. Mid-Cenozoic post breakup deformation in the passive continental margins bordering the Norwegian-Greenland sea. Marine and Petroleum Geology, 19: 79--93.

Lurton, X., 2002. An Introduction to Underwater Acoustics. Springer.

McCave, I.N. and Hollister, C.D., 1985. Sedimentation under deep-sea current systems: Pre-HEBBLE ideas. Marine Geology, 66(1-4): 13-24.

McIver, R.D., 1982. Role of naturally occurring gas hydrates in sediment transport. Am. Assoc. Pet. Geol. Bull., 66: 789--792.

Mienert, J. et al., 2007. ”Gas hydrates of the NSB-margin" Vestnesa Ridge (3D PCABLE AND MULITICOMPONENT SEISMIC) Petromaks- Gans project, Institutt for Geologi, Universitetet I Tromsø.

Mienert, J. et al., 2006. ”Gas hydrates of the NBS margin" W-Svalbard margin (3D cable seismic experiment) petromaks project, Institutt for Geologi, Universitetet I Tromsø.

Mienert, J. et al., 2005. Ocean warming and gas hydrate stability on the mid-Norwegian margin at the Storegga Slide. Marine and Petroleum Geology, 22: 233--244.

Mienert, J., Vanneste, M., Guidard, S. and Iversen, S., 2004. NFR Strategisk Universitets prosjekt (SUP) – Slope Stability, Institutt for Geologi, Universitetet I Tromsø.

Milkov, A.V. et al., 2004. Ethane enrichment and propane depletion in subsurface gases indicate gas hydrate occurrence in marine sediments at southern Hydrate Ridge offshore Oregon. Organic Geochemistry, 35(9): 1067-1080.

Mosher, D., 2006. 3D seismic versus multibeam sonar sea floor surface renderings for geohazard assessment: Case examples from the central Scolian slope. The leading edge, 25(12): 1484-1494.

Nimblett, J. and C. Ruppel, 2003. Permeability evolution during the formation of gas hydrates in marine sediments. Journal of Geophysical Research-Solid Earth, 108 (B9).

Ottesen, D., Dowdeswell, J.A. and Rise, L., 2005. Submarine landforms and the reconstruction of fast-flowing ice streams within a large Quaternary ice sheet: The 2500-km-long Norwegian-Svalbard margin (57{degrees}-80{degrees}N). Geol Soc Am Bull, 117(7-8): 1033-1050.

Paull, C.K., Ussle III, W.R. and Borowski, W.S., 1996. Sources of Biogenic Methane to Form Marine Gas Hydrates In Situ Production or Upward Migration? Annals of the New York Academy of Sciences, 715(Natural Gas Hydrates): 392-409.

Pettersen, J., Bünz, S., Hustoft, S. and Jürgen., M., 2008. 3D seismic imaging of marine gas hydrates in arctic sediments of the Vestnesa Ridge off the W-Svalbard margin, Proceedings of the 6th international conference on gas hydrates (ICGH 2008) Vancouver, British Columbia, Canada.

Rafaelsen, B., 2000. Studier av kenozoiske erosjonsflater i det sørvestlige Barentshav basert på tredimensjonale seismiske data., Unpublished cand. scient. thesis. University of Tromsø.

Rebesco, M. and Stow, D., 2001. Seismic expression of contourites and related deposits: a preface. Marine Geophysical Researches, 22: 303-308.

Rice, D.D., 1992. Controls, habitat and resource potential of ancient bacterial gas. In: R. Vitaly (Editor), Bacterial Gas Conference. Editions Technip, pp. 91-118.

Rice, D.D., 1992. Controls, habitat, resource potential of ancient bacterial gas. In: R. Vitaly (Editor), Bacterial gas. Editions Technip, pp. 91-118.

Sassen, R. and MacDonald, I.R., 1994. Evidence of structure H hydrate, Gulf of Mexico continental slope. Organic Geochemistry, 22: 1029--1032.

Shine, K.P., Derwent, R.G., Wuebbles, D.J. and Morcritte, J.-J., 1990. Climate Change, The IPCC Scientific Assessment, pp. 41--68.

Simoneit, B.R.D. and Lonsdale, P.F., 1982. Hydrothermal petroleum in mineralized mounds at the seabed of Guaymas Basin. Nature, 295: 198-202.

Sloan, E.D., 1998. Clathrate hydrates of natural gas. Marcell Dekker, New York.

Solheim, A., 1994. Seismic atlas of western Svalbard, A selection of regional seismic transects, Glacial deposits on the western Svalbard margin Norsk Polarinstitutt, 52--57 pp.

Sultan, N., Cochonat, P. and Foucher, J.-P., 2003. Effect of gas hydrate dissociation on seafloor slope stability. Submarine mass movements and their consequences, 103-11. Dordrecht, Kluwer Academic Publishers.

Talwani, M. and Udintsev, G., 1976. Initial reports of the deep sea drilling project. 38: 389-449.

Tester, J. et al., 1993. Supercritical water oxidation technology. EmergingTechnologies in Hazardous Waste Management III. American Chemical Society: 35-76.

Thiede, J. and Myhre, A.M., 1996. Introduction to the North Atlantic- Arctic Gateways: Plate tectonic- paleoceanographic history and significance. Proceedings of the Ocean Drilling Program, Scientific Results, 151: 3--23.

Thiede, J. et al., 1998. LATE CENOZOIC HISTORY OF THE POLAR NORTH ATLANTIC: RESULTS FROM OCEAN DRILLING. Quaternary Science Reviews, 17: 185-208(24).

Vanneste, M., Guidard, S. and Mienert, J., 2005. Bottom-simulating reflections and geothermal gradients across the western Svalbard margin. Terra Nova, 17(6): 510-516.

Vanneste, M., Mienert, J., Guidard, S. and partners, H.-I., 2005. ``Arctic`` Gas Hydrate Provinces West of Svalbard, Norway: Preliminary Results, pp. --.

Vanneste, M., Poort, J., Batist, M.D. and Klerkx, J., 2002. Atypical heat-flow near gas hydrate irregularities and cold seeps in the Baikal Rift Zone. Marine and Petroleum Geology, 19(10): 1257-1274.

Viana, A., Faugeres, J. and Stow, D., 1998. Bottom-current-controlled sand deposits - a review of modern shallow- to deep-water environments. Sedimentary Geology, 115: 53-80.

Viana, A.R., Almeida, W.J., Nunes, M.C.V. and Bulhoes, E.M., 2007. The economic importance of contourites. Geological Society, London, Special Publications, 276(1): 1-23.

Viana, A.R. and Faugeres, J.-C., 1998. Upper slope sand deposits: the example of Campos Basin, a latest Pleistocene-Holocene record of the interaction between alongslope and downslope currents. Geological Society, London, Special Publications, 129(1): 287-316.

Vogt, P.R., Gardner, J. and Crane, K., 1999. The Norwegian Barents Svalbard (NBS) continental margin: Introducing a natural laboratory of mass wasting, hydrates, and ascent of sediment, pore water, and methane. Geo-Marine Letters, 19: 2--21.

Vogt, P.R. and Jung, W.-Y., 2002. Holocene mass wasting on upper non-Polar continental slopes-due to post-glacial ocean warming and hydrate dissociation? Geophysichal Research letters 29, 29

Vogt, P.R., Kathleen, C., Eirik, S., D., M.M. and L., P.S., 1994. Methane-generated(?) pockmarks on young, thickly sedimented oceanic crust in the Arctic; Vestnesa Ridge, Fram Strait. Geology, 22(3): 255-258.

Vorren, T.O., Lebesbye, E., Andreassen, K. and Larsen, K.B., 1989. Glacigenic sediments on a passive continental margin as exemplified by the Barents Sea. Marine Geology, 85(2-4): 251-272.

Wessel, P. and Smith, W.H.F., 2008. The Generic Mapping Tools GMT Version 4.3.0. Technical Refference and Cookbook.

Westbrook, G.K., 2008. Fears surface over methane leaks. Nature news, 455: 572-573.

Wood, W.T., Gettrust, J.F., Chapman, N.R., Spence, G.D. and D., H.R., 2002. Decreased stability of methane hydrates in marine sediments owing to phase-boundary roughness Nature, 420: 656-660.

Yusifov, M. and Rabinowitz, P.D., 2004. Classification of mud volcanoes in the South Caspian Basin, offshore Azerbaijan. Marine and Petroleum Geology, 21(8): 965-975.

Aagaard, K., Foldvik, A. and Hillman, S., 1987. The west Spitsbergen Current - Deposition and water mass transformation. Journal of Geophysical Research-Oceans, 92: 3778-3784.